# Growing foundation for Majorana qubits using In-plane Selective Area Networks (InSANe)

Peters, Stan M.E.

*Award date:*
2018

# Growing foundation for Majorana qubits using In-plane Selective Area Networks (InSANe)

Stan Peters

**Supervisors:**

MSc. Roy op het Veld [1]

prof. dr. Erik Bakkers[1]

[1] : Advanced nanomaterials and devices, Department of Applied Physics, Eindhoven University of Technology (AND,TU/e), Eindhoven, The Netherlands

# Abstract

Quantum bits have the potential to make information processing faster and better than ever before. The struggle against decoherence for most quantum bits does not hold for topological quantum bits based on Majorana fermions.[1,2,3] Hybrid semiconductor-superconductor devices could host these semi-particles, where a nanowire would be perfect to fulfil the roll of the semiconductor foundation.[4,5] Here we report the growth of In-plane Selective Area Networks (InSANe) by MOVPE made from the III-V semiconductor InSb. These in-plane nanowire networks would be easy to scale for future applications. The problem of the large lattice mismatch between InSb and the InP substrate has been overcome and single crystalline InSb networks have been achieved. A yield of ~95% demonstrates the excellent control over the growth.

These InSb networks exhibit large electron phase-coherence lengths as shown by Aharonov-Bohm measurements. This underlines the potential of these InSb networks to be used in scalable topological qubit devices.



Keywords: In-plane Selective Area Networks (InSANe), III-V InSb semiconductor, large lattice mismatch, misfit dislocations, topological qubits, hybrid semiconductor-superconductor device.

# Index

Abstract ..... 3
1 Introduction ..... 7
2 Theory ..... 9
2.1 Quantum bits ..... 10
2.2 Latest results on Majorana qubits ..... 11
2.3 Zinc Blende (InSb) properties ..... 13
2.3.1 InSb crystal structure and planes ..... 15
2.3.2 Side facets of nucleations ..... 16
2.4 Epitaxial crystal growth ..... 17
2.4.1 Influence of oxidation on surface energy ..... 19
2.5 Precursors ..... 20
2.5.1 Thermal decomposition of InP surfaces ..... 23
2.6 Aharonov-Bohm effect ..... 24
3 Experimental Methods ..... 25
3.1 Scalable devices: InSANe ..... 26
3.2 Growth scheme ..... 28
3.3 Designs ..... 29
3.3.1 Rainbow design ..... 30
3.3.2 InSb in-plane selective area growth networks ..... 31
3.3.3 InSb in-plane selective area overgrowth ..... 34
3.3.4 Comparing (110) with (112) project; electron mobility and nucleation/growth process ..... 36
3.3.5 Complex designs ..... 37
3.4 Metalorganic vapour phase epitaxy ..... 38
3.5 Scanning electron microscope ..... 40
3.6 Transmission electron microscope ..... 41
3.7 Sample preparation ..... 43
4 Results and Discussion ..... 44
4.1 In search of the optimal growth conditions ..... 45
4.2 Study of nucleation mechanism ..... 49
4.2.1 Indium series ..... 50
4.2.2 Antimony series ..... 53
4.2.3 Nucleation process and side facets ..... 55
4.3 Study of growth mechanism and defects ..... 58

4.3.1 Time series ..... 59
4.3.2 TEM defect analysis ..... 61
4.4 Coherence length in hashtag grown with optimal conditions ..... 72
4.5 Selective area overgrowth in-plane flakes ..... 74
4.6 Thermal annealing ..... 76
4.7 Growth of complex structures realised ..... 79
5 Conclusion ..... 81
6 Outlook ..... 83
6.1 50 nm SiN mask for thicker wires ..... 84
6.2 Study of the merging of multiple nucleations ..... 85
6.3 Global backgate ..... 86
6.4 InP(100) substrate with thermal annealing ..... 87
6.5 AlInSb buffer layer ..... 88
6.6 Flake study ..... 89
6.7 Series with (different) thermal annealing ..... 90
7 References and Acknowledgements ..... 91
8 Appendix ..... 94
8.1 A: How qubits differ from classical bits ..... 95
8.2 B: Guideline for calculating the (effective) V/III ratio ..... 96
8.3 C: Know-how of the SEM ..... 99
8.4 D: Details of sample preparation ..... 101
8.4.1 Phosphoric acid dip ..... 102
8.4.2 PECVD ..... 103
8.4.3 Spin coating ..... 104
8.4.4 Electron beam lithography ..... 106
8.4.5 Development ..... 111
8.4.6 RIE ..... 112
8.4.7 Lift-off ..... 113
8.4.8 Sample preparation for TEM ..... 114
8.5 E: High resolution SEM images ..... 115

# 1 Introduction

Nowadays computer chips can be found in every room and in every device. Each chip containing millions of bits to process and store data. Every year the number of bits on a same size chip increases and the production costs goes down, following Moore's law. The reason for researching qubits can be found in the fast innovation trend for computation power. Figure 1[6] shows the manufacturing process size of a transistor from 2000 to 2020. The physical limits for size reduction are almost reached. New building blocks like quantum bits (qubits) could be used to keep increasing the information processing. This new branch of changing the actual building blocks of a chip instead of only reducing the size is investigated intensively across the globe. Big players like Microsoft, Google and Intel are in a race to become the first company with an operational quantum computer, with the special condition of quantum supremacy. Referring to the amount of quantum bits necessary to outperform 'normal' supercomputers. A quantum computer with 49 quantum bits could already outperform a 'normal' computer for certain calculations, setting the minimum for quantum chips.[7] A reason why the qubits are in the spotlights at the moment is the predicted efficiency in information processing. It could for example be used to aid the drug development. Nowadays new medicines are found by crude guesses and trial and error. The extraordinary amount of interactions between molecules make it almost impossible for a normal computer to come up with a possible medicine. A quantum computer could do this and thereby decreasing the time before a medicine is found and could even come up with less complex medicines making them easier and cheaper to develop.

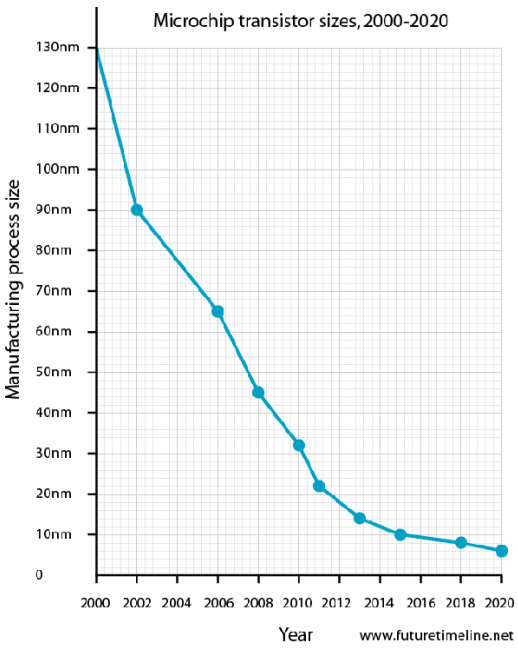


*Figure 1: microchip transistor size between 2000 and 2020. Showing a clear trend towards smaller transistor sizes.*

There are a number of ways to make these quantum bits.[1] The focus in this research will be on topological qubits. These type of qubits have the advantage of the topological protection against errors occurring. Other types of qubits are highly sensitive to uncontrolled physical interaction. Any destructive interaction may result in decoherence of the system, resulting in an error.[8] Majorana fermions could be used as topological qubits.

These semi-particles can be created in a hybrid semiconductor-superconductor device.[9] The foundation of a Majorana qubit should be a semiconductor with a high electron mobility and strong spin orbit coupling. A stable topological state requires an energy gap that exceeds the temperature of the environment, where the energy gap is mainly determined by the spin orbit interaction.[9] Therefore the III-V semiconductor InSb has been used. InSb has an electron mobility of ~30000 $\frac{cm^2}{Vs}$ at 100mK and literature indicates that Insb nanowires have a large spin orbit interaction.[9] This research

only focusses on the semiconductor part of the device. Future research could carry on towards a functioning device.

Majorana fermions could be used for calculations by letting them switch places. The trick is to not let them meet as they would annihilate each other if that were to happen (they are each other's antiparticle). This could be accomplished via different ways.[5,10] One way to accomplish this is by a hashtag design, creating a loop. Literature[11] shows that the growth of InSb nanowire loops has already been accomplished. Their InSb hashtags are grown out-of-plane and on an InP stem, shown in figure 2. The red part of the structures is InSb, the other parts of the nanowires are the InP stems. This out-of-plane approach limits the feasibility of complex structures and makes it hard to scale. In this research we will try to improve this concept by changing to in-plane nanowire networks and using selective area growth (InSANe). This method has the potential to scale to more complex designs.

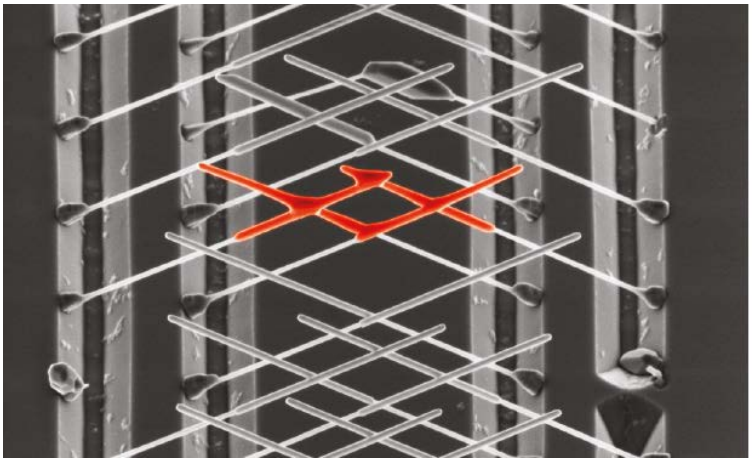

*Figure 2: Image of the out-of-plane InSb hashtags grown on an InP substrate. Special trenches ensure that the nanowires grow in a certain direction so they will meet mid-air like a military saber arch.*

The reason why out-of-plane nanowires are used in literature[11] is the huge lattice mismatch with current most used wafers like InP. Decreasing the interface area and using stems make it possible for the InSb to relax without forming defects. These defects could decrease the phase-coherence length of electrons in the semiconductor, something that should be avoided. Growing in-plane networks of InSb directly on an InP wafer gives rise to defects due to the lattice mismatch of ~10.4% and the large interface area. The main goal of this research is to make this growth work nonetheless.

# 2 Theory

In every research it is important to know what the path behind you is and what lays ahead. That's why chapter 2.1 is dedicated to quantum bits. Why are we altogether interested in these structures? As there are too many 'flavours' of qubits to investigate them all, topological superconducting qubits have been chosen as the main focus of this study. These are described in chapter 2.2. Literature[11,12,13,10] already shows the feasibility to grow these semiconductor foundation structures with varying methods and materials. For future applications in industry the devices should be scalable. Majorana fermions are used for the topological qubit. These semi-particles have special needs to be cultivated, special environments are necessary. With things like spin orbit interaction and phase-coherence length of the electrons being important, literature[14,9] suggests that InSb would be the perfect candidate for the semiconductor foundation. Therefore InSb has been used in this research, and its properties and crystal structure are described in chapter 2.3. The theory behind epitaxial crystal growth, used in this research, is explained in chapter 2.4. Different growth mechanisms are explained as are the influence of native oxides on the surface energies and Phosphor evaporation resulting in surface decomposition. For the growth it is also important which materials are present in the chamber of the MOVPE. When using MOVPE, special precursors deliver the group III and V elements for the crystal growth. These precursors are described in chapter 2.5. The phase-coherence length of the electrons could tell a lot about the transport in these in-plane nanowires. Aharonov-Bohm measurements are performed to measure the coherence length of the electrons in these structures, this principle is described in chapter 2.6.

## 2.1 Quantum bits

There are a lot of ways to make quantum bits. Each version has its own pros and cons. The 5 types of qubits that are investigated into around the globe are shown in figure 3[1]. The superconducting loops easily integrate with nowadays Silicon chip industry. But keeping it cool all the time and the easy collapse of the system are big issues they have to confront. Trapped ions are on the other hand very stable and the system lasts for more than a 1000 seconds. Long enough for a quantum system. But the need for a lot of lasers and the relatively slow operation show the trade-off. These are two examples for qubits, showing that each concept still has its flaws. One of the big concerns for almost every qubit is the destructive interaction. Any unwanted physical interaction can cause the quantum state to collapse, giving the wrong result. So called 'help-qubits' are needed as a check to correct for these errors, increasing the number of qubits required. Topological qubits are the only exception. The topological protection of the quantum system prevents collapses making it error-prove. However, it is the only qubit concept which has not produced a working device yet . Showing that it is perhaps the most difficult one to control, but maybe so much more worthwhile. That is why in this research we focus on the topological qubit by using Majorana fermions. This is described in chapter 2.2.

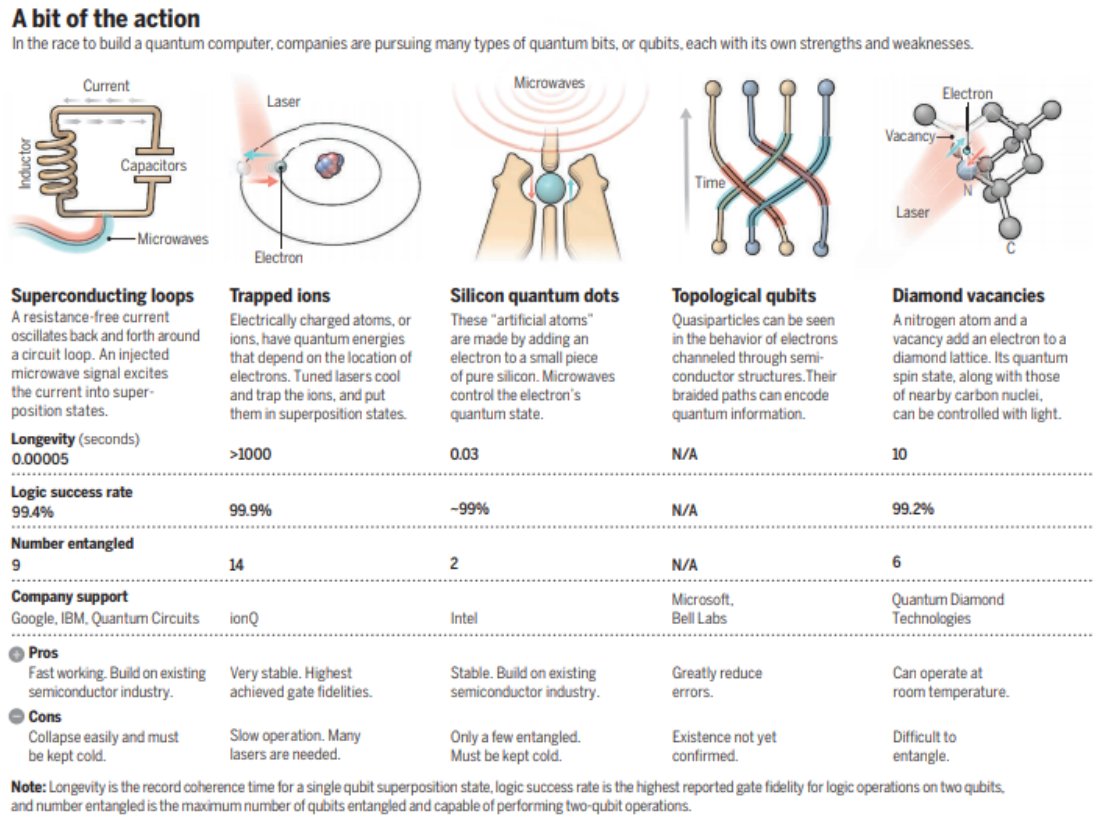


*Figure 3: The image shows the methods of creating quantum bits which are researched in the present. Each qubit has its own strength and weakness. The figure also shows which company is supporting each method, revealing on which horse they bet.*

A short introduction in the way quantum bits differ from classical bits can be found in appendix 8.1: A

## 2.2 Latest results on Majorana qubits

Our research focusses on topological qubits named Majorana fermions. The existence of these half-particles was first predicted by Ettore Majorana in 1937. The Majorana's have quite a few extraordinary properties. As shown in figure 4, the Majoranas ($\gamma_1$ and $\gamma_2$) are formed at the interface of a superconductor and a semiconductor,[15] hence the need for a hybrid semiconductor-superconductor device. This spatial separation makes it topological protected. A change in electric field, magnetic field or even temperature will not immediately destroy the Majoranas. The Majoranas are its own antiparticle, which means that if the two half-electrons would meet they would annihilate each other and disappear. They are in fact semi-particles in the sense that they are the result of the whole electronic system acting as one entity. In

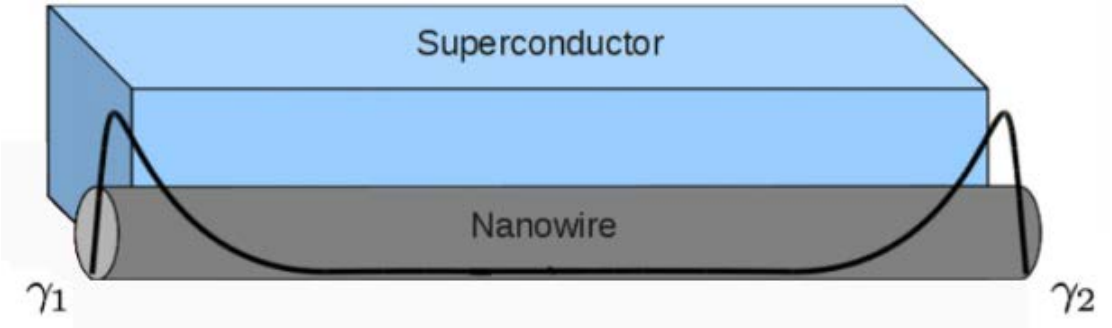


*Figure 4: Illustration of Majorana fermions forming at the edge of a superconductor and semiconductor interface. Where the semiconductor is a nanowire, a one dimensional quantum system.*

this research the framework for the Majorana qubits has been fabricated, the semiconductor nanowire network. For the essential energy gap a strong spin orbit coupling is required, this is why we use the Indium Antimony (InSb) semiconductor. More information about this III-V material and its properties can be found in chapter 2.3. Just having the Majorana fermions in a nanowire is not enough to use them in a quantum computer. Special structures are necessary to be able to use these Majorana fermions for computations. Several research groups have already investigated how such a device would look like. The structures one of them came up with are described in chapter 3.3. One common element of each design is a loop, enabling the braiding of the Majorana fermions for computations. The first InSb loop has been grown successfully by Gazibegovic et al.[11] In this research special out-of-plane InSb nanowires were grown. If the nanowires would all grow perpendicular to the substrate a loop would never form. Therefore they made a special substrate with trenches. These trenches have different (111)B facets. Nanowires grown perpendicular to these trenches cross each other mid-air with a 109.47° angle. Multiple trenches were used to create a loop above the substrate. Figure 5 illustrates this process. A small offset in coordinates of the nanowires which would meet mid-air causes the nanowires to just graze each other during growth instead of bumping into each other. This enhances the chance of the wires to merge nicely and the creation of the wanted loops. It is difficult to grow InSb directly on top of InP due to the lattice mismatch. Therefore a gold catalyst and an InP stem were used to kick start the process. The InP stem can be compared with the grafting of trees for faster growth (shown in figure 6 on the left side). A downside of this method is the degradation of the InP stem. When switching to InSb (thus significantly decreasing the phosphine pressure in the chamber) and growing under high temperatures the phosphor starts to evaporate out of the InP stem. Phosphor evaporation out of InP is described in chapter 2.5.1. After a while the stem breaks, putting a limit

on the maximum length of the InSb nanowires. Another limiting factor has to do with the way the nanowires merge. For a loop the nanowire has to merge with at least two other nanowires, one of these junctions is always created before the other. This means that the first junction has been under growing conditions for a longer time. Making that one thicker and possibly less perfect for the application. The growth process has been nicely shown in figure 5. With the nanowires facing each other kind of like a military saber arch.

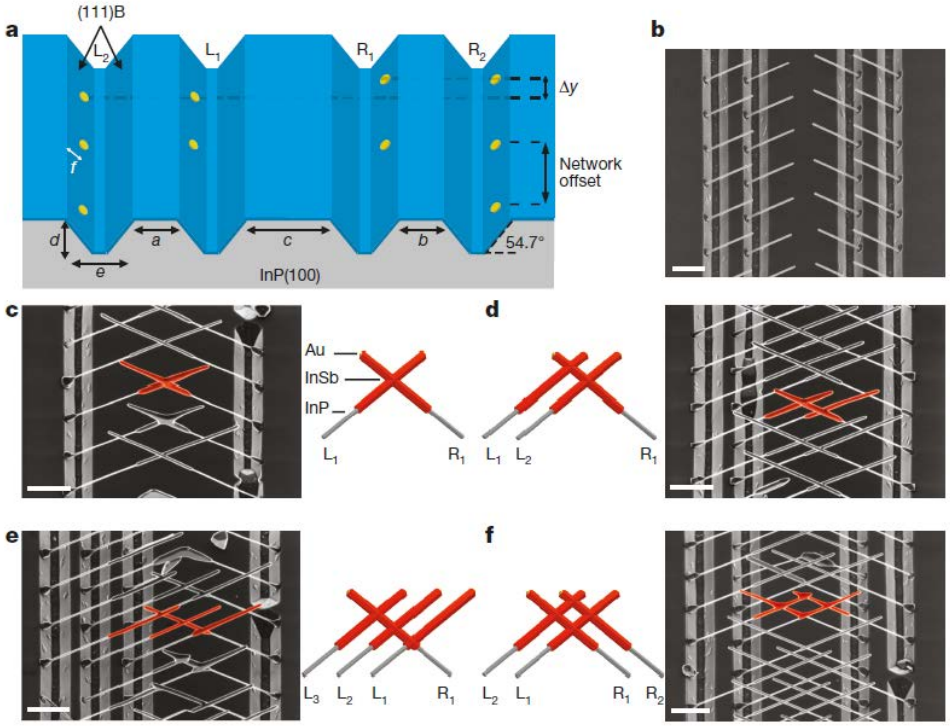


*Figure 5: 9.a shows the trenches with (111) facets used to make the InSb loops. Figure b till f show different times during growth. From the growth of the stem till the second merge to close the loop. The InSb is highlighted in red.*

To do transport measurements on these devices to check the coherence length of the electrons the loops are broken off and put flat on another surface. This has to be done to make the contacts and gates. The final setup for transport measurements is shown in figure 6. The InSb is again highlighted in red, the yellow indicates the gold contacts and the grey wires are the gate. A magnetic field is applied perpendicular to the surface. By measuring the Aharonov-Bohm effect, as described in chapter 2.6, they found a large coherence length for the electrons, an indication that these structures could be used for quantum bit applications.


*Figure 6: Final setup for the transport measurements. The loop is put down on a surface for contacting and gating. A magnetic field is applied perpendicular to the surface. Left images show the grafting of trees, comparable with the use of an InP stem.*

## 2.3 Zinc Blende (InSb) properties

In this research InSb is used. InSb is a III-V semiconductor comprising Indium (In) and Antimony(Sb) with a melting point of 530°C. This combination results in a semiconductor with a large lattice constant of 6.47Å. Figure 7 shows various III-V and II-VI semiconductors with corresponding lattice constants and energy gaps.[16] Observe that InSb has by far the largest lattice constant. This poses a problem for the growth of InSb on another (cheaper) III-V semiconductor substrate. The strain caused by the lattice mismatch will cause unwelcome defects.

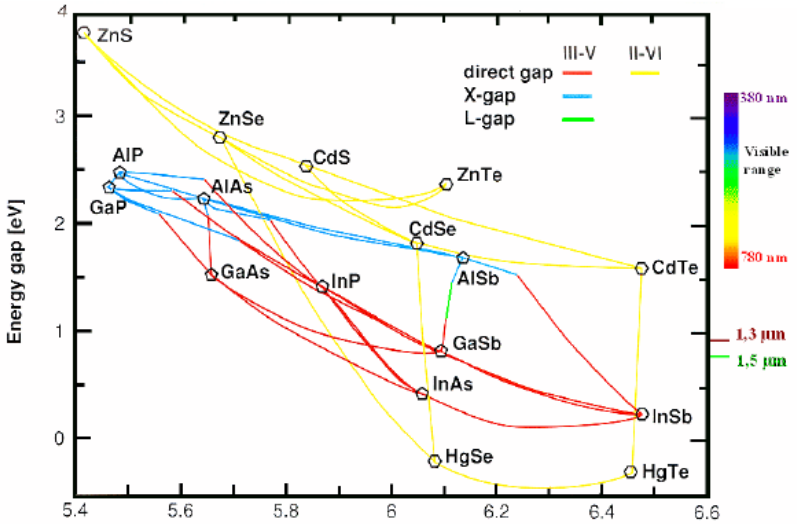


*Figure 7: The energy gap and lattice constant is shown for several III-V and II-VI semiconductors. Observe that InSb is on the far right side with a large lattice constant.*

InSb has a small bandgap of 0.17eV. Combined with a large Landé g-factor of 50 and high electron mobility at base temperature around 100mK of ~30000 $\frac{cm^2}{Vs}$ compared to other semiconductors as shown in figure 8[14], this results in a suitable candidate for Majorana qubit devices. Red indicates the electron mobilities of electrons and blue for holes. Different values can be found for the same material, this is due to induced strain. In this research an InP wafer is used as a substrate, the lattice mismatch of ~10.4% is calculated by using equation 1.

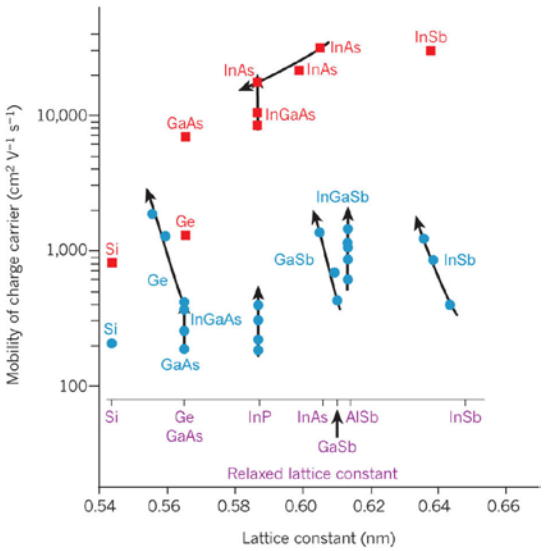


*Figure 8: Mobility of charge carriers in several semiconductors and the corresponding lattice constant. InSb can be found in the upper right corner with the highest mobility of charge carriers*

$$L_{mismatch} = \frac{a_0(s) - a_0(f)}{a_0(f)} * 100\% = \frac{|5.869 - 6.479|}{5.869} * 100\% \sim 10.4\% \quad (1)$$

Hybrid semiconductor-superconductor devices are widely discussed for their use as topological superconductors. The topological superconductor could be used to host Majorana fermions for quantum computer applications. A requisite is that topological gap exceeds the temperature at which the device operates (~50mK). The spin orbit interaction (SOI) plays a key role in determining this topological gap. Literature[9] shows that the InSb nanowires have a large Rashba spin-orbit strength of 0.5-1eVÅ, corresponding to a spin orbit energy of 0.25-1 meV. This result again underlines the promises of InSb in applications like hybrid semiconductor-superconductor devices.

### 2.3.1 InSb crystal structure and planes

InSb has a cubic face centred crystal structure. It is Zinc-blende and its space group is $F43^{-}$ m. The crystal structure is visualized with VESTA and shown in figure 9.[17] The InSb crystal orientation is dependent on the crystal orientation of the substrate. Substrates of interest for this research are the InP(100) and the InP(111)B. The difference in orientation is illustrated with planes. The green plane is the (100) direction while the red plane is the (111) direction. As the directions exhibit different bonding directions/angles between atoms parallel to the surface, they are expected to have different characteristics. This is important to determine which wafer to use as the substrate.

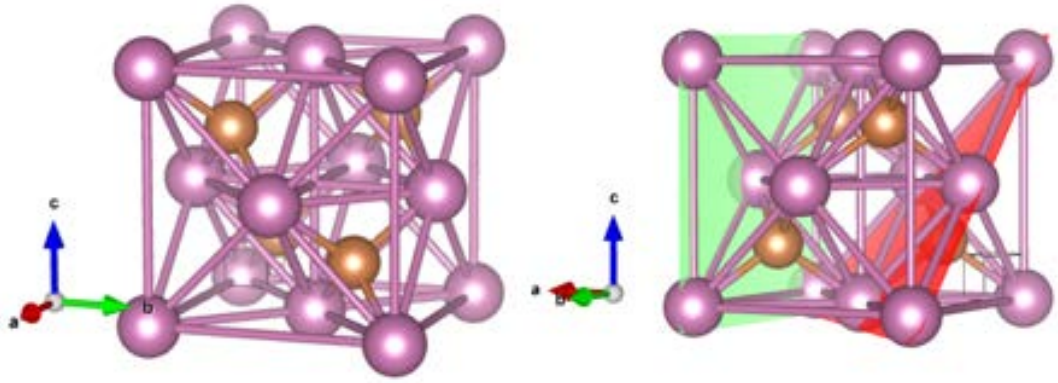


*Figure 9: Left image shows cubic face centered crystal structure of InSb. The right image shows the (100) plane in green and the (111) plane in red. Both images were made with VESTA.*

Zooming in on the (100) and (111) plane, the different geometries in these directions become visible. On the left of figure 10 the (100) plane is shown in green. This direction has 45° and 90° angles. Expected is that these directions are preferential growth directions along the surface. The (111) plane shown on the right side has 60° angles belonging to the (112) family. This first analysis would indicate that structures on the InP(100) wafer could be grown with 90° angles, while structures on the InP(111)B wafer would have 60° angles. This research focusses on the InP(111)B wafers as this seems to grow easier. (Shown in chapter 4).

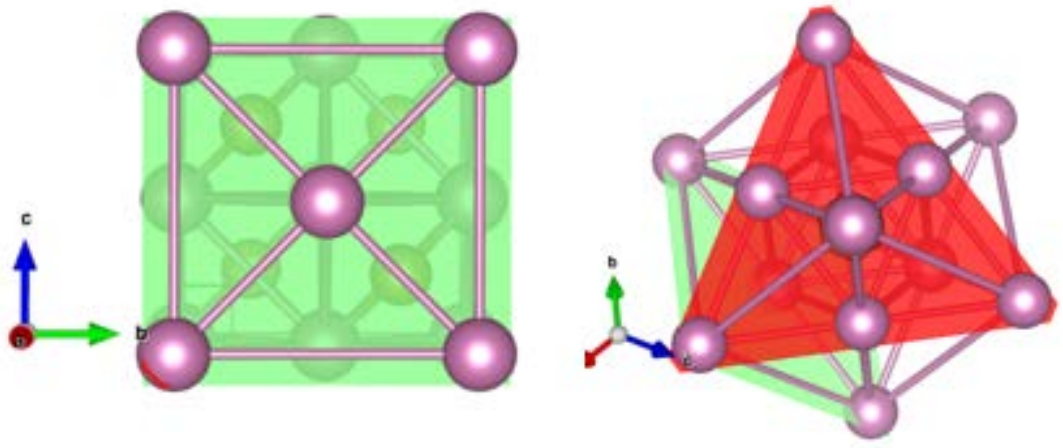


*Figure 10: The left image shows the (100) plane of the cubic face centred crystal structure of InSb with 90 degree angles. The right image shows the (111) plane with 60 degree angles.*

### 2.3.2 Side facets of nucleations

As the surface and the orientation of the trenches have crystal directions (Miller indices), so have the side facets of a nucleation. Studying these facets could tell us which facets have the lowest surface energy and are likely to form. Research performed by Chun-Yung Chi et al.[18] analyses these facets. They study the formation of GaAs nanosheets grown out of nanostripes just as the InSANe project. A GaAs(111)B substrate has been used. Due to the same zinc-blende structure and crystal direction of the substrate these results could maybe be applicable to the InSb in-plane nanowires. Figure 11 shows two SEM images of their nanosheets and the orientations of the side facets.

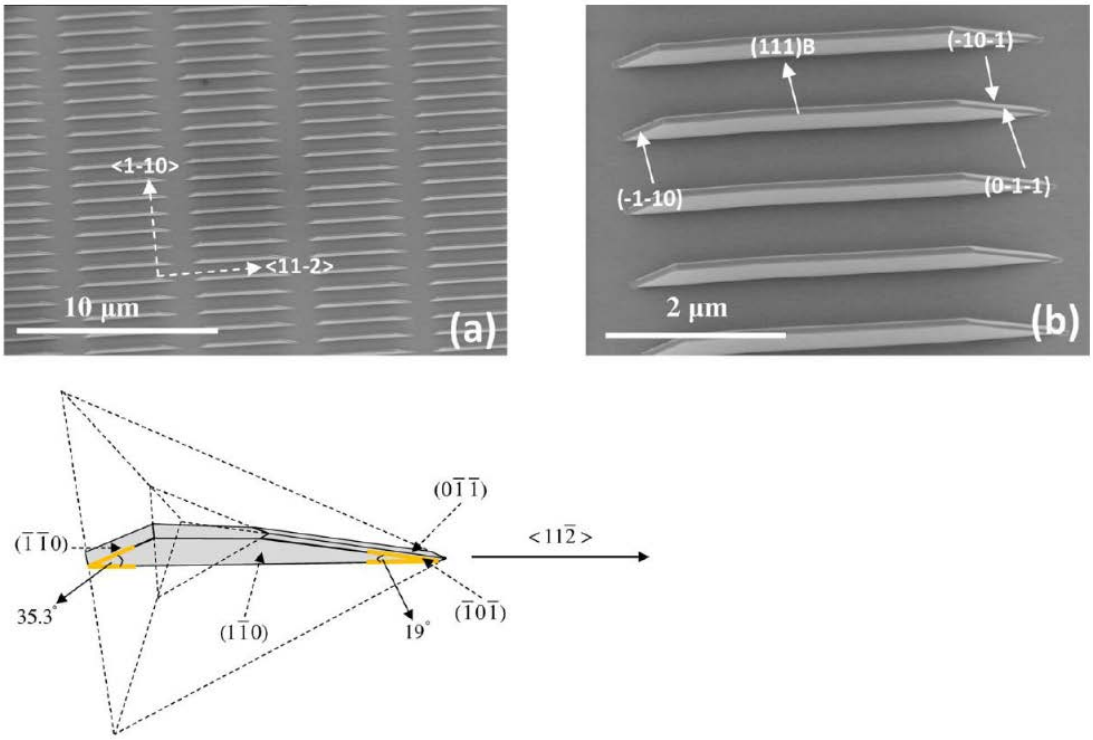


*Figure 11: Figure A shows an image of multiple nanosheets growing out-of-plane on a GaAs(111)B substrate. Figure b and c show the orientations of the side facets. Where the top facet is flat and similar to the substrate so a (111)B. The two flat sides have a (1 -1 0) facet. One inclined facet is a (-1 -1 0) facet as shown in figure c on the left. The other side has two facets. Similar like a knife. One side is the (-1 0 -1) facet while the other one is a (0 -1 -1 ) facet.*

Figure 11.c clearly shows the facets and their Miller indices. One side seems to have a flat inclined (-1 -1 0) facet, while the other inclined side has two facets, like the sharp side of a knife. These have a (0 -1 -1 ) an a (-1 0 -1) direction. All side facets are from the (110) family. This result is compared with the side facets of the nucleation from our experiment in chapter 4.2.3.

## 2.4 Epitaxial crystal growth

Epitaxial growth, first discussed by Royer in 1928[19] , is the ordered growth of ultrathin films. It uses a crystalline substrate to deposit a thin film on top which adopts the crystalline structure of the substrate, making high-quality semiconductor crystals. There are lots of ways to grow an epitaxial layer. Such as vapor-phase epitaxy(VPE), liquid-phase epitaxy (LPE), solid-phase epitaxy(SPE). Metal-organic vapour phase epitaxy (MOVPE) uses gas containing precursors from the required elements which crack and nucleate at the surface, forming an epitaxial layer. MOVPE is used in this research and will be further discussed in chapter 3.4. The nature of precursors and which ones are used in this research is discussed in chapter 2.5.

A method called the Kossel crystal, first discussed in 1927[20], describes the processes that happen on the surface. The adatoms sticking to the surface can diffuse across the surface. To minimize the energy they form terraces on the surface. A lower state of energy is found when they have more neighbours. This is shown in figure 12. The shape in which they grow depends on the surface energies.

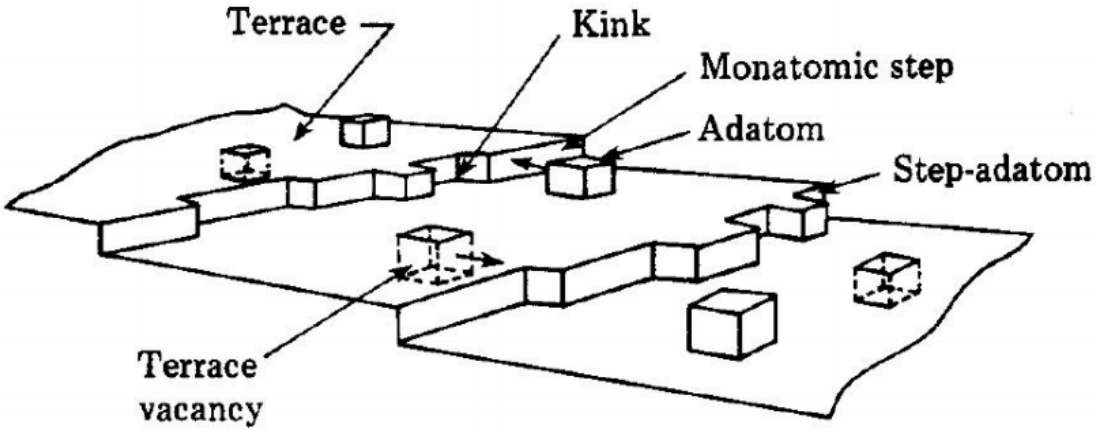


*Figure 12: Kossel crystal: surface of the epitaxial layer showing terraces and adatoms.* [58] *The adatoms diffuse across the surface and stick at places where they have the lowest energy. This is usually the place where they can form the most bonds. The surface energies determine the growth.*

When talking about hetero-epitaxial growth, three primary modes come to mind.[21] The first mode is the Frank-Van der Merwe, where the epitaxial layer is grown layer by layer. A requisite is a small lattice mismatch between the epitaxial layer and substrate and a low interface energy. This mode arises due to the stronger interaction between the atoms and the substrate compared to the atom-atom interaction. The second mode is known as the Volmer-Weber mode, where islands form and grow bigger till they connect. This is due to the stronger interaction between the adatoms than the interaction between the adatom and the substrate, lattice mismatch is a must. Bigger lattice mismatches can cause strain in the film material. If strain accommodation is not possible, lattice defects will occur, reducing the electron mobility.[22] The lattice mismatch is defined as:

$$L_{mismatch} = \frac{a_0(s) - a_0(f)}{a_0(f)} \qquad (2)$$

Where $a_0(s)$ is the lattice constant of the substrate and $a_0(f)$ is the lattice constant of the film. Materials with lattice mismatches below ~9% will grow pseudomorphically. The lattice mismatch between the materials used in this experiment

(InP and InSb) is around 10.4%. The crystal structure and properties are further discussed in chapter 2.3. There is a critical thickness of the layer after which dislocations are introduced, $d_c$. This critical thickness is defined as

$$d_c = \frac{b}{2L_{mismatch}} \tag{3}$$

Where b is the size of the unit cell of the thin layer. With a unit cell size of 0.648nm for InSb, the critical thickness $d_c$ is around 3.11 nm. As we grow structures with a height between 20 and 80 nm, dislocations and other defects are unavoidable.

The last mode is the Stranski-Krastanov mode, a coalescence of the first two modes, where first a layer grows according to the Frank-Van der Merwe mode and after the critical thickness is reached the process follows the Volmer-Weber mode, where an island landscape is formed. The critical thickness depends on the strain and chemical potential of the epitaxial layer. The three modes are shown in figure 13. Which growth mode the material will follow depends on the material properties, lattice mismatch and surface energies. Oxidation of the surface, reducing the number of dangling bonds, could change the surface energy for example. The influence of native oxides is discussed in chapter 2.4.1.

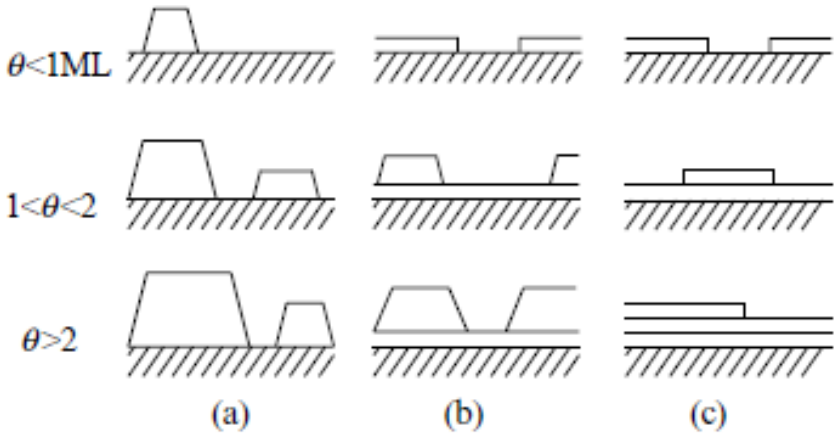


*Figure 13: Schematic illustration of the three main growth modes: "layer-by-layer"-Frank-Van der Merwe(FM); "island"-Volmer-Weber(VW); "layer plus island"-Stranski-Krastanov(SK). Where interface energy is sufficient to cause island formation, VW growth will occur; SK growth is uniquely confined to systems where the island strain energy is lowered by misfit dislocations underneath the islands.*[20]

### 2.4.1 Influence of oxidation on surface energy

As shown in the previous chapter, different growth mechanisms can happen, depending on the interaction. This interaction between the surface and the adatoms is mainly due to the dangling bonds at the surface. If this interaction is stronger than the interaction between the adatoms, layer by layer growth will happen. Native oxides block these dangling bonds, decreasing the interaction between the adatoms and the surface. This could shift the growth mechanism from layer by layer to island growth for example. As the main project of this research is to grow in-plane nanowires, pure island growth should be avoided. Therefore annealing of the surface is important. The passivation of the surface is illustrated in figure 14.

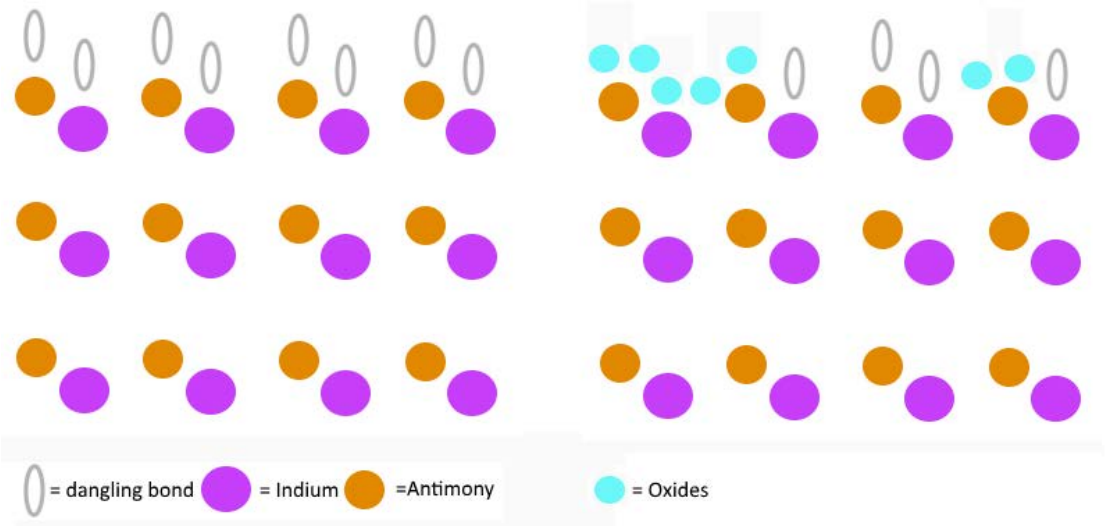


*Figure 4: Very rough sketch of the passivation of the InP surface by native oxides. The dangling bonds decrease changing the chemical potential of the surface. Note: the oxide layer is not as trivial as illustrated.*

Literature[23] indicates that the native oxide layer on chemically polished and etched InP(111) surfaces is about 30 Å thick. The oxide layer is non-homogeneous, where the outermost surface layer is Indium rich while the layer directly below (near surface) is Phosphor rich. Ion Scattering Spectroscopy (ISS) and Atomic Emission Spectroscopy (AES) have been used to detect this difference. The Indium in the near surface region (Phosphor rich) is evenly present as $InPO_3$ and $InP$. The subsurface region has small amounts of $In_2O_3$. They also indicate that the interface between the InP and the oxide layer is sharply defined.

## 2.5 Precursors

The Indium and Antimony needed for the growth of InSb are present in the growth chamber as precursors. Precursors are molecular structures which encompass specific elements. We use Tri-methyl-Indium (TMI) and Tri-methyl-Antimony (TMSb) as precursors for the growth. Mainly due to their availability in the cleanroom.

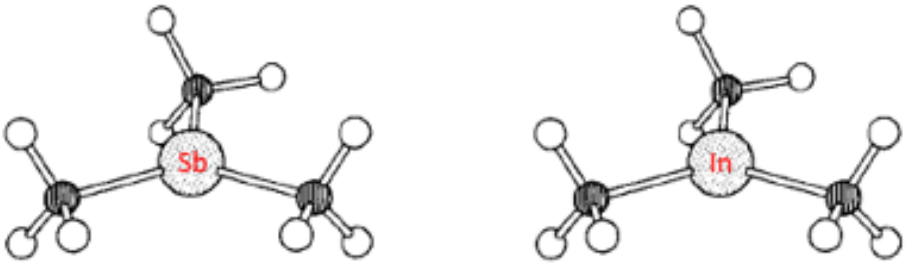


*Figure 5: On the left side the chemical structure of TMSb is shown. This precursor has three methyl groups attached. By breaking the bonds with these methyl groups the antimony is free to grow an epitaxial layer. On the right side the chemical structure of TMI is shown with the same side chains.*

Figure 15[24] shows the molecular structure of the precursors. With on the left side the TMSb molecule and on the right side the TMI molecule. Each of the two precursors has 3 methyl groups attached. For the growth to succeed the methyl groups need to detach from the element. This happens by X-C bond scission. This process is called cracking, pyrolysis or decomposition and is dependent on the temperature. The cracking efficiency increases with increasing temperature. The cracking efficiency is also dependent on the bond strength of the precursors. The bond strengths of TMI and TMSb are respectively 47 and 55,9kcal/mol[24,25], an indication that TMSb will crack at a higher temperature.[26]

There are several precursors for each element. TMSb is used for its useful vapour pressure and ready availability. Figure 16 shows the cracking efficiency for TMSb and other Antimony precursors as a function of the temperature in a He environment.[24]

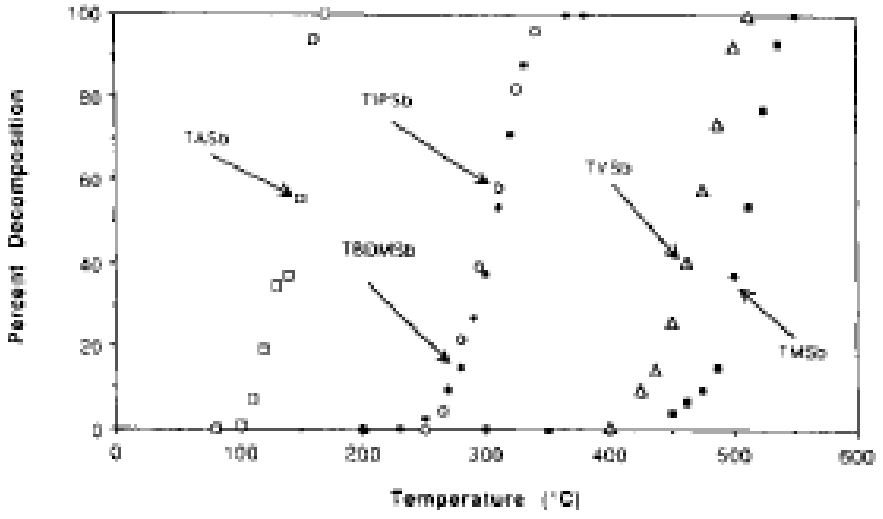


*Figure 6: Comparison of percentage decomposition versus temperature for several antimony precursors in an He ambient.(After Cao et al. ) reprinted with permission from the Journal of Electronic Materials, a publication of the Metallurgical Society, Warrendale, Pennsylvania.)*

Another research[27] shows the percentage of decomposition of TMSb (○), TVSb (□) and TIPSb (Δ) as a function of temperature for different environments. The filled shapes (●) are the results from a pyrolysis with $H_2$ and a high surface area of the reactor and the open shapes (○) are the results from a pyrolysis in $H_2$ with a low surface area. The cracking efficiency is ~40-80% for TMSb with a surface temperature of 425°C. This is already very different than the previous graph would suggest, meaning that not only the temperature is important but the environment as well. In our case $H_2$ was used to dilute the line, meaning that data from the figure below should be used.

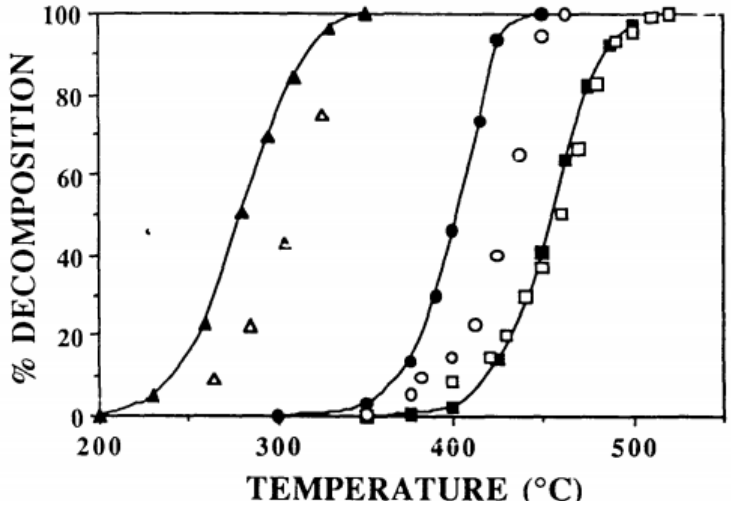


*Figure 7: Percent decomposition of Antimony precursors as a function of the temperature. Full decomposition happens at 500 degrees Celsius. An environment of $H_2$ has been used with a high (●) and low(○) surface area. The three precursors, TMSb(○), TVSb(□) and TIPSb(Δ).*

TMI has been examined more extensively. The $sp^2$ bond (In-CH3) is fairly weak. For temperatures below 480 °C (as in our case) there seems to form an involatile polymer. Figure 18 shows the percentage decomposition for TMI as a function of the temperature. It can be observed that above 400 °C the TMI is completely cracked.[28] This figure was made by Buchan et al.[28] to investigate the effect of the carriers on the

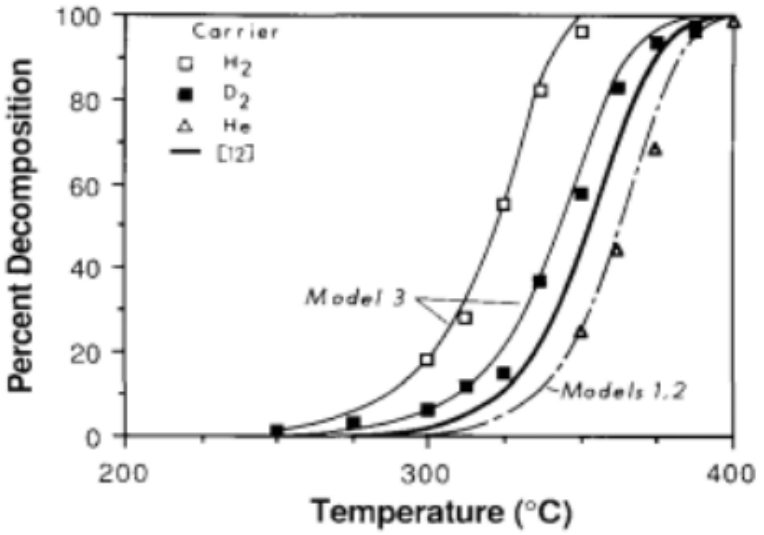


*Figure 8: Percent decomposition of TMI as a function of the temperature. Full decomposition happens at 400 degrees Celsius. Different environments are used to test the influence on the cracking efficiency.*

pyrolysis. It can be observed that a different carrier causes a shift in the cracking efficiency line. Again showing that the environment influences the pyrolysis.

The difference in cracking efficiency between TMSb and TMI is important to keep in mind. For easy checking of the Sb/In ratio in the chamber it is necessary to have a growth temperature at which the TMSb is completely cracked. If the growth temperature is below this minimum the cracking efficiency should be taken into account when calculating the V/III ratio. The guideline for the calculations can be found in appendix 8.2: B. The minimum of around 480 °C (by looking at figure 17) has consequences for the substrate. At this temperature the Phosphor in the InP wafer starts diffusing, hereby damaging the surface and changing the growth mechanisms as described in chapter 2.5.1. A phosphine pressure in the chamber could be used to reduce the diffusion at this temperature but this could result in phosphor incorporation in the InSb nanowires/networks, unwanted contamination. Due to this deadlock lower temperatures need to be used, subsequently the cracking efficiency is a significant aspect.

### 2.5.1 Thermal decomposition of InP surfaces

InP is a well-known and highly used semiconductor. When high temperatures are part of the experiment, phosphor evaporation is a real problem. Research has been done before to investigate this phenomena. Research done by Riesz et al.[29] shows that heating an InP substrate results in the deterioration of the InP surface. Macroscopic etch pits and Indium accumulation are a sign of this thermal decomposition. This is basically due to the preferential evaporation of Phosphor over Indium, resulting in Indium rich regions on the surface. This excess Indium can form Indium droplets on the surface and these droplets can progressively dissolve the InP surface. They used a quadrupole mass spectrometer (QMS) to detect the Phosphor ion current while heating the InP surface. The chamber pressure was $\leq 7 * 10^{-3}\ Pa$. The result is shown in figure 19. The Phosphor evaporation is visible around 480°C. The evaporation could already happen at lower temperatures if the InP surface is kept at that temperature for an extended timeframe. Incongruent evaporation of InP commences already at 300°C in vacuum. This problem as already been studied in the 80's by looking at the Indium droplet induced etch pits [30] or the phosphor loss by mass spectrometry[31,32]

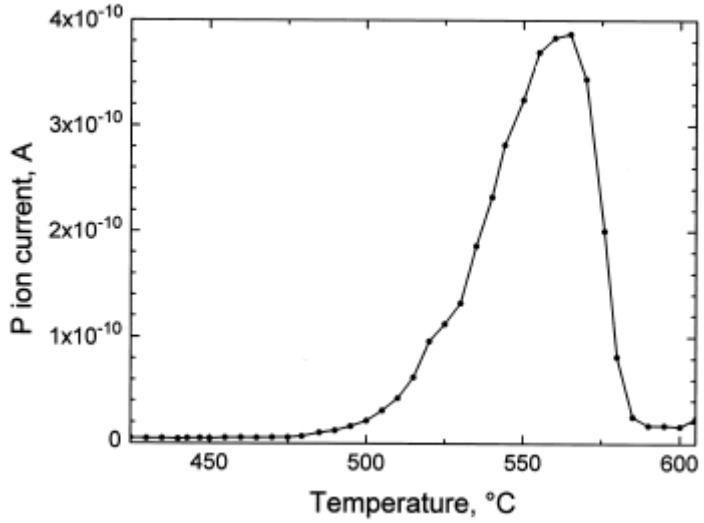


*Figure 9: A typical P evaporation curve. The heating rate is 0.6°C $s^{-1}$. The Phosphor ion current is plotted as a function of the temperature. The Phosphor evaporation is visible around 480°C.*

Prevention of this thermal decomposition of InP surfaces by Phosphor evaporation is important and can be achieved by a Phosphine pressure in the chamber. This could be applied when using thermal annealing to get rid of the native oxides without damaging the surface. A consequence is the presence of Phosphor in the growth chamber which could make the InSb less pure.

## 2.6 Aharonov-Bohm effect

The Aharonov-Bohm effect defines the phenomena where a charged particle is being influenced by an electromagnetic field which is present only in areas where the particle cannot reach. In an Aharonov-Bohm study, using the Aharonov-Bohm loops (AB loops) described in chapter 3.3.2, the phase shift of the electrons is examined by looking at the interference patterns. The interference patterns arise due to electrons move along different sides of the loop. Electron one (red) moves from entry to exit via point A while electron two (yellow) moves via B. This different path gives an interference pattern due to the magnetic field applied perpendicular to the surface.


*Figure 10: Autocad file showing the design of an AB-loop. One electron may move from entry to exit via A while the other one moves from entry to exit via B. While a magnetic field is applied perpendicular to the surface, this gives rise to an interference pattern.*

The coherence length can be examined with the Aharonov-Bohm effect. The coherence length basically is the propagation distance over which a coherent wave can travel while still showing an interference peak. As shown in figure 20, an electron can go straight from point entry to exit via A or B. It is also possible that an electron completes a full loop before exiting (entry-A-B-A-exit), or even multiple loops. The more interference peaks(loops) are visible in the data, the bigger the coherence length is. Many interference peaks would indicate a very crystalline nanowire with little to no defects. In chapter 4.4 the results are shown for our AB-loops.

# 3 Experimental Methods

In this section the experimental methods are discussed. First the growth mechanism behind the InSANe project is explained in chapter 3.1. In chapter 3.2 the growth scheme is shown, indicating special parameters during growth. As the growth is in-plane, there are an infinite amount of possible designs that can be grown. The designs used in this experiment are clarified in chapter 3.3. In this research metalorganic vapour phase epitaxy (MOVPE) is used to grow in-plane InSb nanowires and networks on an InP substrate using selective area growth, the MOVPE steps are described in chapter 3.4 . After growth the results are observed using a scanning electron microscope (SEM) , for which the ins and outs are explained in chapter 3.5. Another well-known method to analyse the crystal structure of the grown structures is the transmission electron microscope (TEM), a short explanation can be found in chapter 3.6. The final chapter is dedicated to the numerous of fabrication steps which are needed to use selective area growth with help of a SiN mask. These are described in chapter 3.7, an extensive description of each step can be found in appendix 8.4 D.

Side note

Wafer cleaning is important during every step in the fabrication process to ensure good quality. Contaminants such as solvent stains, dust particles or smoke particles can have adverse effects during oxidation and evaporation. Solvents stains can be detected using dark field microscopy. Picture 21 shows the clean room classification system. [33] The cleanroom that has been used to process the wafers falls in the category ISO 7.

| Class | Maximum Particles / m³ | | | | | | U.S. Federal Standard 209E Equivalent |
|---|---|---|---|---|---|---|---|
| | ≥0.1 µm | ≥0.2 µm | ≥0.3 µm | ≥0.5 µm | ≥1 µm | ≥5 µm | |
| ISO 1 | 10 | 2 | | | | | |
| ISO 2 | 100 | 24 | 10 | 4 | | | |
| ISO 3 | 1,000 | 237 | 102 | 35 | 8 | | Class 1 |
| ISO 4 | 10,000 | 2,370 | 1,020 | 352 | 83 | | Class 10 |
| ISO 5 | 100,000 | 23,700 | 10,200 | 3,520 | 832 | 29 | Class 100 |
| ISO 6 | 1,000,000 | 237,000 | 102,000 | 35,200 | 8,320 | 293 | Class 1000 |
| ISO 7 | | | | 352,000 | 83,200 | 2,930 | Class 10,000 |
| ISO 8 | | | | 3,520,000 | 832,000 | 29,300 | Class 100,000 |

*Figure 11: IEST ISO 14644-1 International Standard for Cleanrooms. On the left side the ISO number can be found, each level has a strict maximum number of particles per size. On the left side the equivalent U.S. Federal standard 209E can be found for comparison*

### 3.1 Scalable devices: InSANe

The discussed paper in chapter 2.2 shows the feasibility of growing InSb devices on an InP substrate. The downside is the limited scalability of these devices. The length is limited due to the InP stem and creation of one junction before the other as explained before. For quantum computer applications it is important to increase the scale. Therefore another approach must be found to solve these problems. Table 1[34] compares the pros and cons for two different growth mechanisms, the 1D nanowire growth as used by Gazibegovic et al.[11] and the growth of an epitaxial 2D layer. As visualised by the table, the 2D layer growth and 1D nanowire growth complement each other. Therefore a growth mechanism combining these two techniques would be ideal. This mixture is investigated in this research, called In-plane Selective Area Networks (InSANe).

*Table 1: Comparison between epitaxial 2D layer growth and 1D nanowire growth. Advantages and disadvantages are shown for both techniques.*

| **2D layer growth** | **1D nanowire growth** |
|---|---|
| + Little substrate processing | - Extensive substrate processing |
| - Defects due to lattice mismatch | + Accommodate significant lattice mismatch |
| + Scalable | - Scalability is limited |
| + No catalyst required | - Requires a metal catalyst for defect free wires |

Combining both techniques would result in an in-plane nanowire. A nanowire grown from a single point creeping over the surface. Some method would have to be used to guide the nanowire in the right direction, much like tree shaping as shown in image 22 on the right side. In this case a SiN mask was used. The mask prevents growth, so only on the places without the mask growth is possible. The desired design is etched into the SiN mask exposing the InP underneath, enabling the growth. Figure 22 shows the result of this combination on the left side. Where the structures constitute of only InSb. First a nucleation is formed somewhere on the design. With new material reaching the nucleation, it starts to grow and fill the design. This method needs way less substrate processing than the out-of-plane nanowires. Growing in-plane also makes the devices easy to scale. The large lattice mismatch between InSb and InP causes defects due to the large interface area. TEM can be used to see if these defects stay at the interface. This would result in a defect-free region on top.

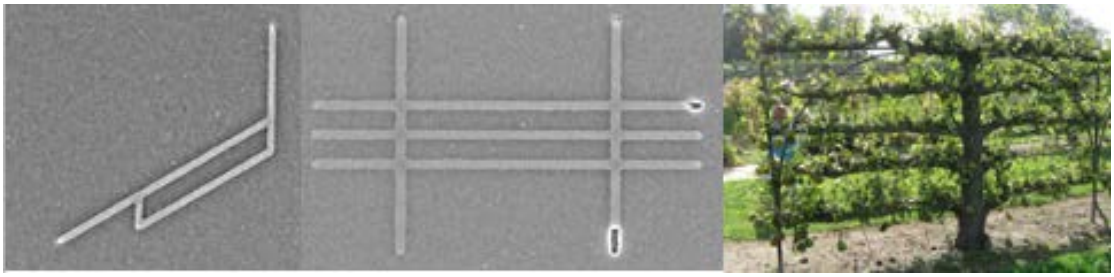

*Figure 12: Left and middle image show the result of combing both techniques. In-plane InSb networks/loops. The dark region in the middle is an empty trench. The right image shows the tree shaping of apple trees, guiding the growth much like the SiN mask.*

This method to grow in-plane networks is also used by Krizek et al[12] to grow InAs networks. By using a GaAs(Sb) buffer layer to accommodate for the lattice mismatch with the substrate they are able to grow the desired structures. Figure 23 shows their results. They use an InP(001) wafer with $SiO_x$ mask, with crystal growth directions in the (110) and (100) direction.

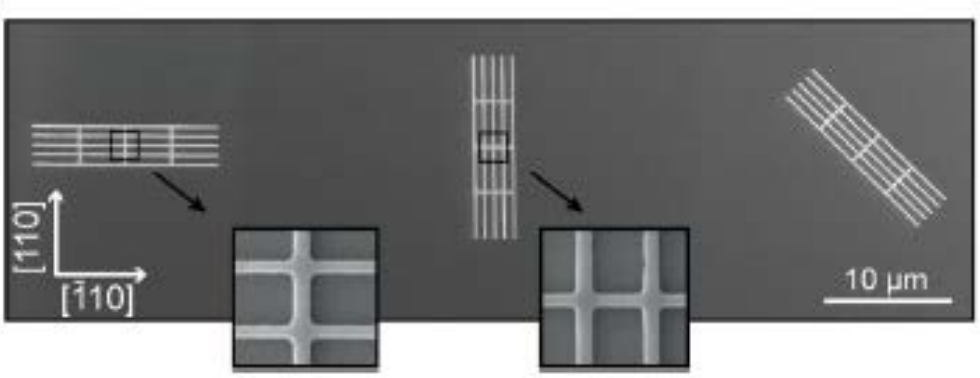


*Figure 13: SEM image of the grown InAs nanowires on a GaAs substrate with help of a GaAs(Sb) buffer layer. The buffer layer is used to accommodate for the stress.*

This research shows that the growth of III-V semiconductors is possible using the vapour-liquid-solid method (VLS) and selective area growth on a substrate with a large lattice mismatch. It illustrates the feasibility of growing large devices with this method. For Majorana fermion devices, a strong spin orbit coupling is essential. Therefore InSb would be even more suitable than InAs.

Other research done by Desplanque et al.[13] shows the growth of InSb on a GaAs substrate. They used a semi-insulating GaAs(001) substrate with an AlGaSb buffer layer covered with $SiO_2$ and grew InSb trenches using selective area growth with the atomic hydrogen assisted MBE. Their results are shown in figure 24. The (110) growth directions were used along the (001) surface with nanostripe openings varying in width from 50nm to 500nm. The images clearly show a better controlled growth at lower widths. The designs are still limited in complexity.

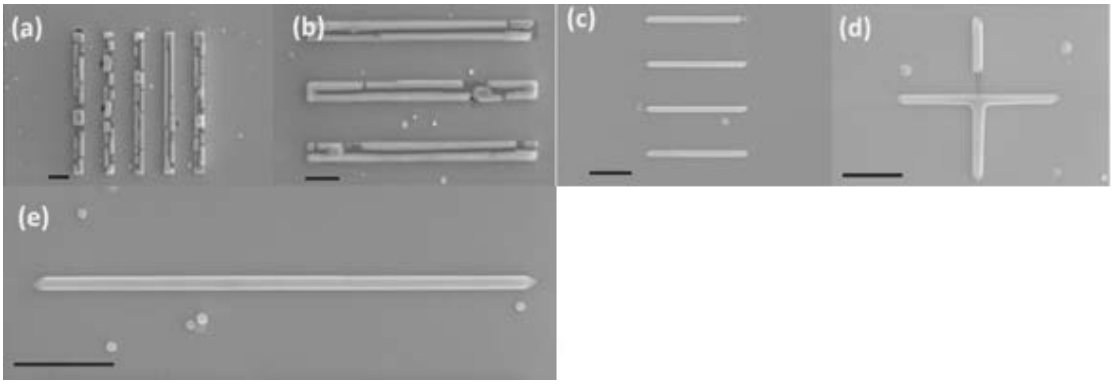


*Figure 14: SEM images from the InSb filled trenches on a GaAs(001) substrate with an AlGaAs buffer layer. Figure a and b have an opening with a width of 500nm, clearly showing island growth. Figure c is a design with a width of 50nm. Figure d's design has a width of 50nm. Figure e has again a design with a width of 50nm. Showing the feasibility of this method, if using small widths.*

## 3.2 Growth scheme

The InSb networks are grown using a MOVPE. The growth temperature is 460°C. This is the temperature of the heater itself. As there is some material between the heater and the top of the wafer and there is a gas flowing over the wafer, the actual temperature at the surface is expected to be 30-40 degrees less. (~425 °C). Heat up is performed with 30 sccm (Standard cubic centimetre per minute at 273K) of TMSb or a molar fraction of 1.19E-3. After the growth temperature is reached, the flow is set to the amount of TMSb during growth. After a stabilisation time of 3 minutes the Indium line is opened. The growth window is defined as the total time the Indium line is open. After growth the Indium line is closed and the heater stops heating. The cool down is performed under a TMSb flow again for 3 minutes after which the TMSb line closes as well. The growth process is shown in figure 25. With the temperature in °C and the time in minutes. At the top is indicated when each lines opens and closes. It is important to mention that during the heat up the system overshoots its target and reaches around 480°C before stabilising at 460°C. The growth window is 40 minutes in this case.

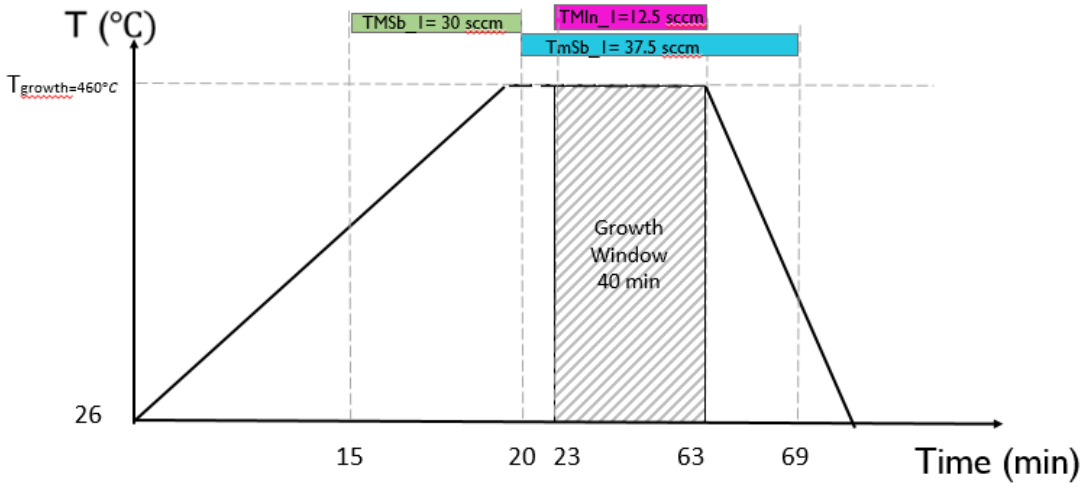


*Figure 15: Illustration of the growth scheme. The temperature is shown as a function of the time. The heat up to 460 °C is done with an TMSb pressure, the lines are adjusted to the growth parameters and after the TMSb line is stable the TMI line opens, indicating the start of the growth window.*

For the experiments the molar fractions of TMI and TMSb have been varied, as has the length of the growth window.

## 3.3 Designs

In this research several experiments have been performed. Each experiment has its own design fine-tuned for its purpose. The different designs are described in the next chapters. To investigate how the growth is dependent on the growth orientation along the (111) surface, a rainbow design has been made. This is described in chapter 3.3.1. An interesting observation from the first runs is the ability to grow well in the (110) and the (112) orientations. Special designs have been made to investigate the differences in these orientations, these are shown in chapter 3.3.4 The main goal of this research is to grow an InSb foundation for qubit applications. These designs are described in chapter 3.3.2. A side mission is to investigate the flake forming that was observed during the growth of the main goal. The InSb surpasses the SiN mask in height and starts to form a nice 2D layer on top of the SiN mask. The designs for this side quest are described in chapter 3.3.3. At last complex designs have been made to show the ability to control the growth. These complex designs can be found in chapter 3.3.5.

### 3.3.1 Rainbow design

A rainbow design is used to investigate the directions in which the InSb grows nicely. The design is basically a block of nanostripes with varying length and width. The block has been duplicated while rotating 10 degrees every time, this is shown in figure 26.

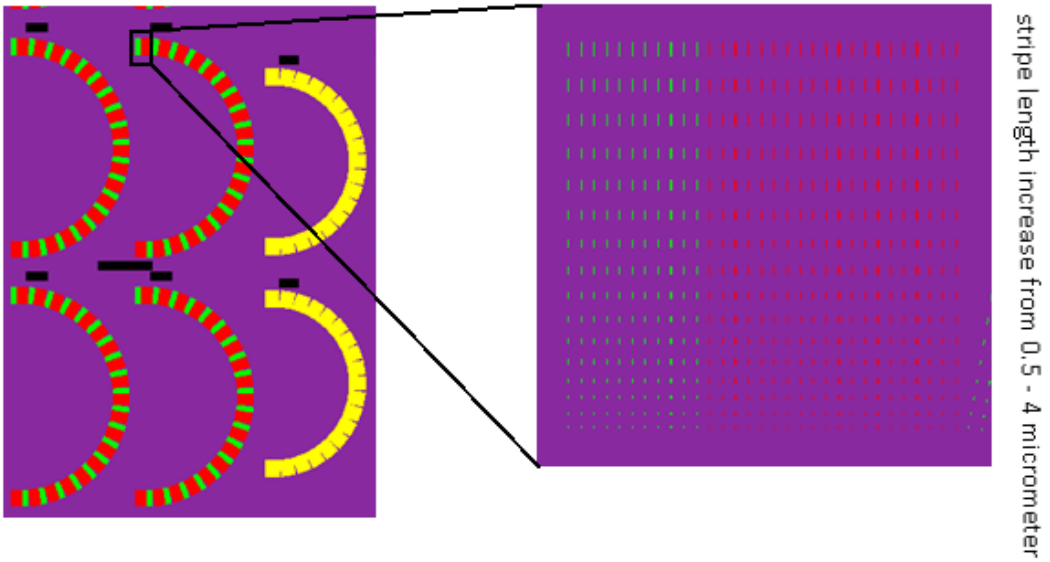


*Figure 16: Illustration of the rainbow design to check to growth in different directions. A zoomed in image on the right shows that for each angle a block of nanostripes with varying length and width has been used.*

The distance between each nanostripe/opening is 10 micrometre to ensure that the 'collect' area for each stripe is the same. Meaning the area from which the material diffuses into the trench. This 10 micrometre is expected to be more than the diffusion length. Meaningful to add is that after an Ebeam exposure the 20 nm width trenches are in fact 35 nm in width. The Ebeam cannot write smaller feature sizes. The trenches/nanostripes in the SiN mask are filled with crystalline InSb. As the InSb is unable to nucleate at the SiN interface the growth only happens in the trenches. However, when growing for a long time the InSb nanowire reaches out of the trench. This is shown in figure 27.[35]

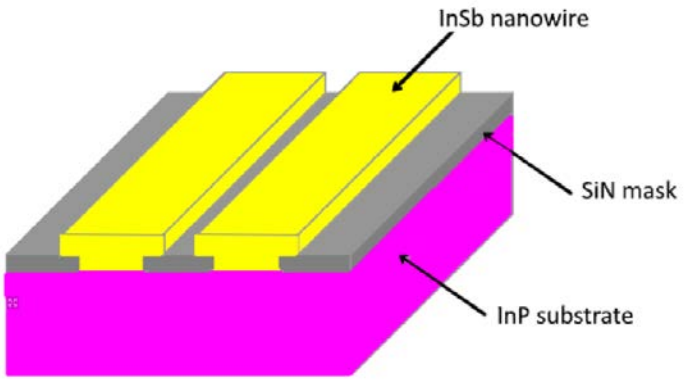


*Figure 17: A schematic view of the device. An InP(111)B substrate with a SiN mask on top. Damming the InSb growth inside the trenches.*

### 3.3.2 InSb in-plane selective area growth networks

For the main experiment different designs have been used. As the purpose of this experiment is to grow nicely grown nanowires/devices, the growth directions along the surface should be chosen correctly. The results from the rainbow design from chapter 3.3.1 are discussed in chapter 4.1. Summarizing, the (110) and (112) directions grow well on an InP(111)B substrate. These crystal directions are shown in figure 28 relative to the wafer (left image). Where the flat of the wafer is a (110) crystal direction. The (110) and (112) family of directions are alternating each other, every time having an angle of 30 degrees between them as shown in the figure. An exemplar design is shown at the bottom of the wafer, only using the (112) directions. The right image shows a real InP wafer, where the dark blue is the SiN mask, the designs are visible.

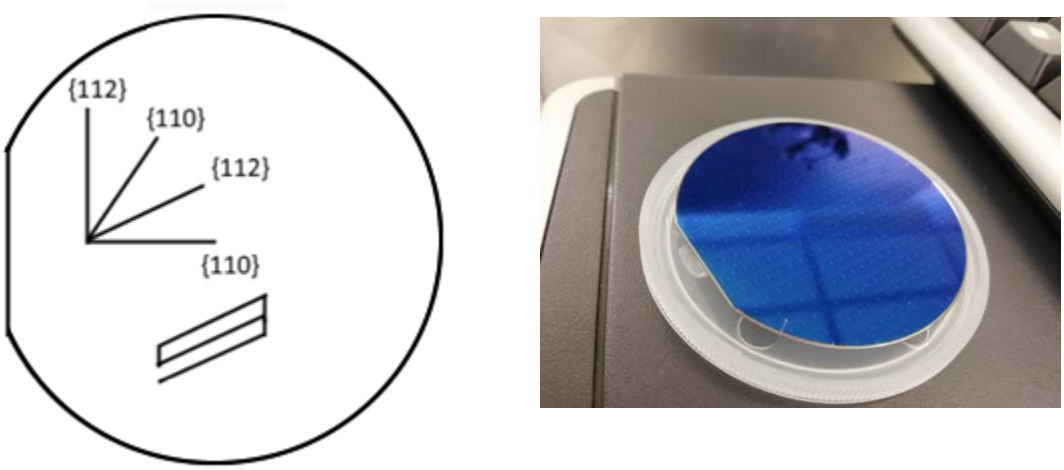


*Figure 18: Illustration of an InP(111)B wafer with a (110) flat shown left on the left side. The crystal (112) and (110) directions are shown. An exemplar design only using (112) directions can be found in the bottom, looking like a nine. Right side shows an image of a real InP wafer with design.*

Growing in other directions on the surface results in bad growth, as the InSb wants to grow in one of above mentioned directions as these facets have the lowest energy. This results in selective area overgrowth, forming a 2D plane on top of the SiN mask. The selective area overgrowth has been used to make large 2D planes of InSb for the first time. This is discussed in chapter 4.5. The main goal in this research is to make InSb devices for Majorana qubits. There are already a lot of papers discussing different designs for the qubit devices.[36] One paper by Plugge et al. is used as a guideline for our research. In this paper, a concept of a Majorana one qubit device is drawn, this concept is shown in figure 29.

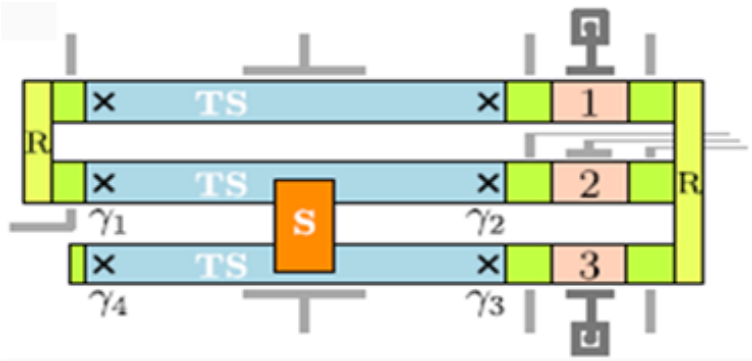

*Figure 19: A drawing of a Majorana qubit device by Plugge et al. The γ's represent the Majorana's, where 1 and 2 form the first couple and 3 and 4 the second. The orange S stands for a superconductor bridge. TS is a topological superconductor. Necessary gates are also shown.*

Here, the full 'nine' like design foundation is made out of an InSb semiconductor indicated in blue, green and pink. The orange part is made out of a superconductor. To make it easier for the transport measurements to put contacts on

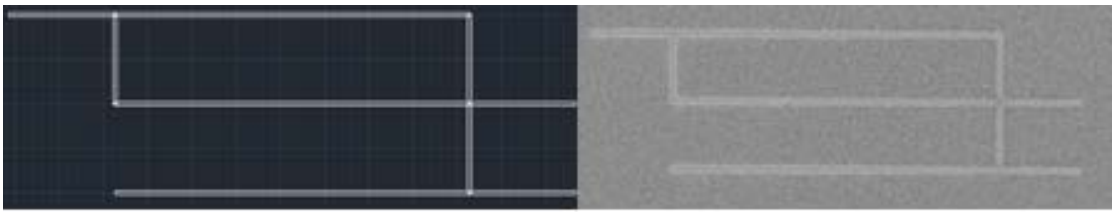

*Figure 20: Left image shows the Autocad design made for the Ebeam. As the design is made out of rectangles, the smooth transition at corners is ensured by making crosses at each corner from the 4 corners. Right image shows a SEM image from the InSb network with the same design.*

the device, several 'arms' are added to the design. The electronic mask for the ebeam, made with Autocad and Visual Basic, looks like figure 30 on the left side. The design already resembles the intended design from the paper.

Figure 30 shows the final result on the right side with a SEM image. The dark grey area is the SiN mask. The light grey design is the InSb grown on top of the InP wafer. Other designs have been grown as well for other transport measurements, such as the Aharonov-Bohm effect design. All designs are shown in figure 31. Where the 1 Majorana fermion couple and 1 qubit device are like suggested by Plugge et al.[36]. The AB-loops (Aharonov-Bohm effect) are used to check the coherence length of the system via transport measurements. More information can be found in chapter 2.6. The hashtag can be used for the Aharanov-Bohm effect measurements as well.

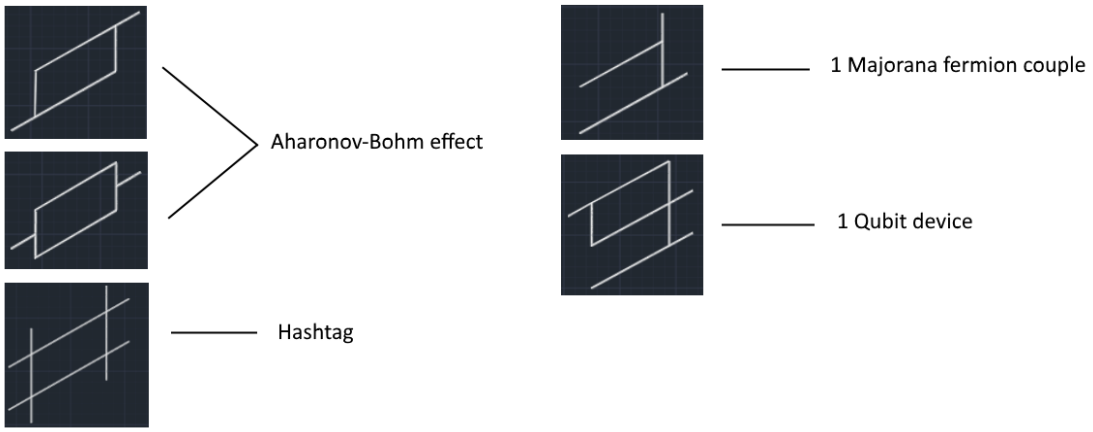


*Figure 21: All designs for the In-plane network project are shown. Two designs for Aharonov-Bohm effect measurements, two designs for Majorana's, two devices for the electron teleportation measurement and different designs like a hashtag to check the growth.*

### 3.3.2.1 Majorana box qubit device designs

Research done by Plugge et al.[36] gives schematics for possible Majorana qubit designs. The unit is made from three hybrid semiconductor-topological superconductor wires, where two of these wires are coupled by a superconductor bridge and the third acts like an interference arm. This way topologically protected qubits can be realised by using existing techniques.

The design for the one qubit box is already shown in the previous chapter. Scaling this design would result in something like showed in figure 32. Where the two qubits are connected by quantum dots 4 and 5, allowing for readout of their joint parity. The other quantum dots serve as a 'read and manipulate' button for each qubit individually.

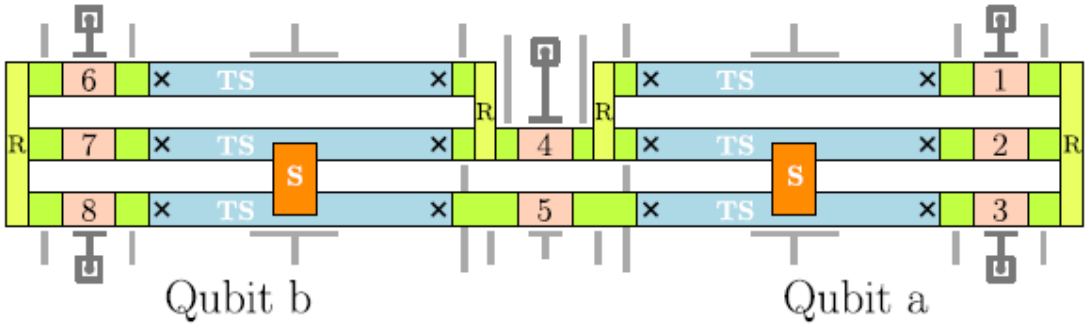


*Figure 22: 2 qubit device where the two qubits (a and b) are connected via two quantum dots. Quantum dots 4 and 5 can be used for readout of their point parity. The other quantum dots can be used to manipulate and read the qubits individually. The orange block is a superconductor, the blue part is a topological superconductor on top of a semiconductor nanowire. X marks the spot where Majorana's are formed.*

One step further would result in a four qubit device as shown in figure 33. The different qubits are again connected via quantum dots for readout of the joint parity.

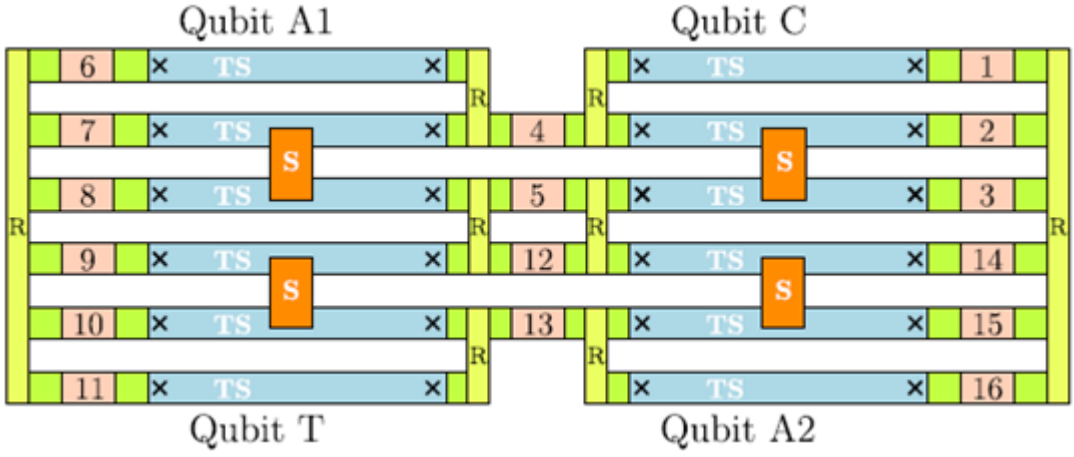


*Figure 23: A four qubit device schematic from literature. Basically mirroring the two qubit device and adding a few connections.*

### 3.3.3 InSb in-plane selective area overgrowth

The side project is the selective area overgrowth for InSb in-plane flakes. The starting point is the same as with the network project. A SiN mask covers the InP surface, the design is etched into the SiN. But instead of following the crystal directions of the (112) and (110) family (alternating (110) and (112) with 30 degrees in between), the designs are now aligned exactly in between the angles of these two families (15 degrees). This is shown in figure 34. The designs are again grown on an InP(111)B substrate with the flat in the (110) direction.

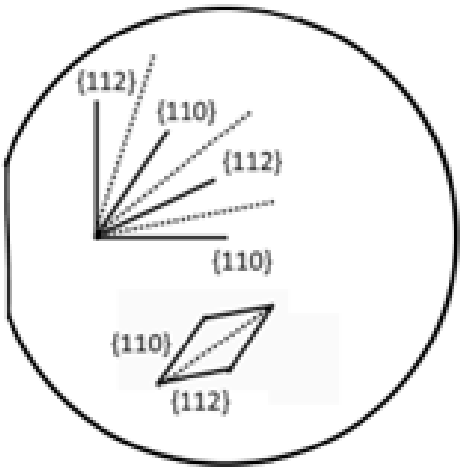


*Figure 24: Illustration of an InP(111)B wafer with a (110) flat shown left.. The crystal (112) and (110) directions are shown. This time the design has been grown with directions directly in between these two families. An exemplar design only using these directions can be found in the bottom, looking like a parallelogram. The side facets are (110) and (112).*

Here the dashed lines are the directions which are used at least once in each design. Designs with only dashed line directions have been made, as well as the combination of a dashed line and a (110) or (112) direction. After reaching over the SiN walls, the InSb wants to relax in the (110) and (112) directions. It forms a parallelogram as shown in figure 35. Special designs which use these 'in between' angles have been used to optimize the total area of the flakes and to create a big 2D layer.

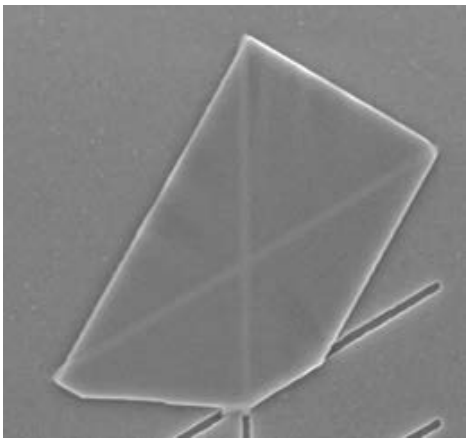

*Figure 25: SEM image showing the in-plane selective area overgrowth of InSb on an InP(111)B substrate. The InSb hovers over the SiN mask as it does not attaches to it. The parallelogram is formed by relaxtion in the (110) or (112) direction.*

Four designs have been made to investigate the growth of these in-plane flakes. Hexagonal shapes like beehives, leaf nerves with the flakes as leaf tissue, a zigzag design and a triangle. All shown in figure 36.

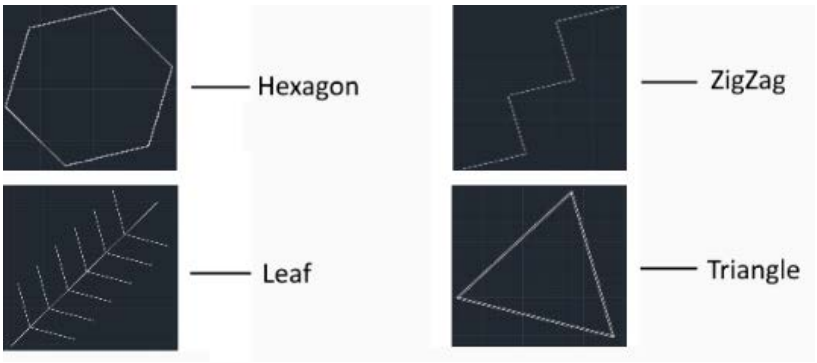


*Figure 26: All designs for the in-plane selective area overgrowth project. The hexagon, leaf, zigzag and triangle. All have lines with angles in between the (110) and (112) direction.*

### 3.3.4 Comparing (110) with (112) project; electron mobility and nucleation/growth process

As told before, in this research the (110) and (112) directions are compared. To check if there is a difference in electron mobility a L-shape has been made. An angle of 90 degrees and one in the same direction as the flat makes sure that one side of the L is a (112) direction while the other one is a (110) direction. Figure 37 shows such a design on the left side.

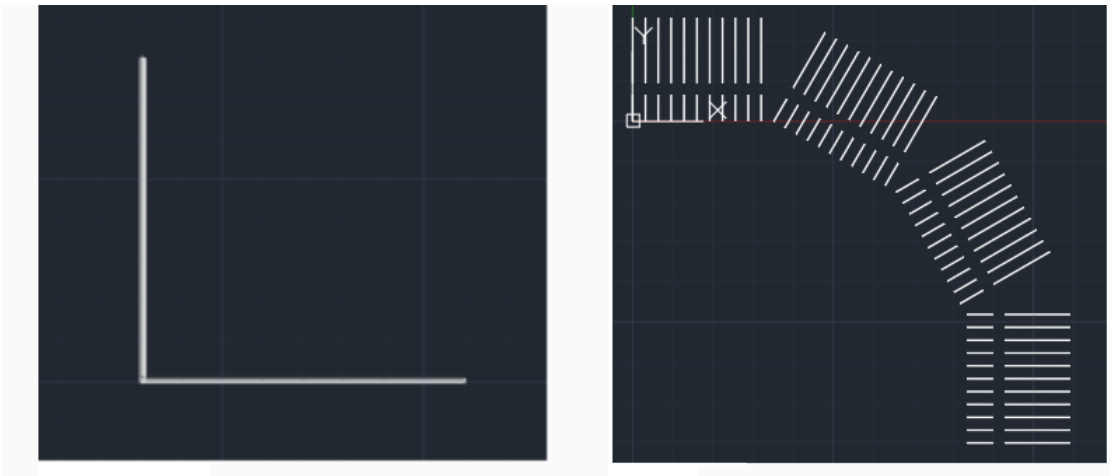

*Figure 27: Left image shows a L-shaped design to measure the electron mobility difference between the two directions. Right image shows the nucleation design. Where the 0 and 60 degree block are the (112) direction and the 30 and 90 degree block are the (110) direction. The nanostripes are 20 and 50 micrometer long to have enough nucleation per stripe.*

To investigate if the nucleation process is different for the (110) and the (112) direction, long nanostripes are used. Trenches of 20 and 50 micrometre long have been repeated ten times for 0, 30, 60 and 90 degrees. Where the 0 and 60 degrees are the (112) direction and the 30 and 90 degree are the (110) direction. Multiple nucleations are expected in every trench. Measuring the distances between nucleations and the length of nucleations could show a difference between the two directions. 10 Repetitions of the lines are used to do statistical analysis.

### 3.3.5 Complex designs

More complex designs have been made to show the excellent control over the growth. In these both the (112) and (110) directions have been used. Firstly, figure 38 shows the design for the 4 qubit device as described in chapter 3.3.2.1. Each rectangle is 1500 by 250 nm. The lines have a width of 20 nm.

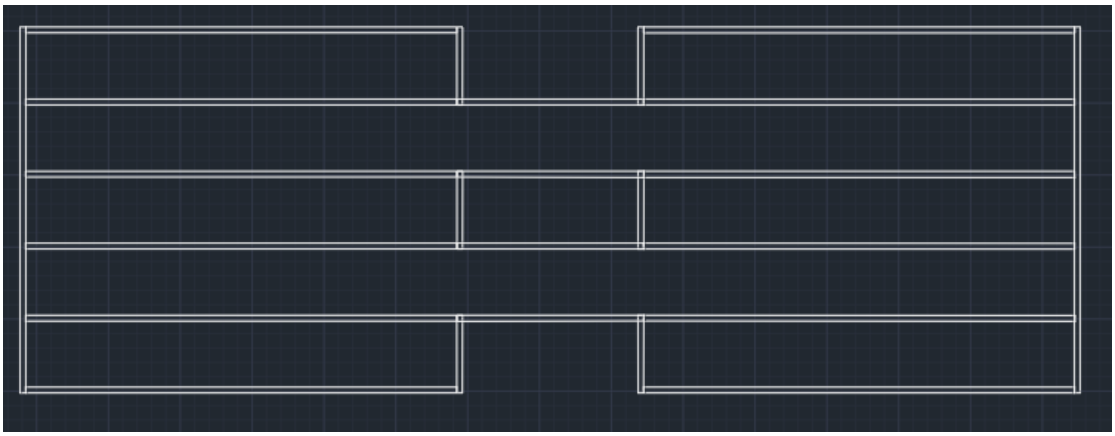

*Figure 28: Design of a four qubit device by Plugge et al. The design uses (112) and (110) directions. Each rectangle is 1500 by 250 nm and the lines have a width of 20 nm.*

Other complex designs have been by writing words/phrases for promotion and again to show the ability to grow complex structures. Two of these designs are shown below in figure 39. 'AND@TUE' and 'Microsoft' (sponsor). As only certain directions are possible to grow, the letters have only vertical and horizontal lines. The explode function of Autocad has been used to create these designs and a special square font called '5 Darius'.

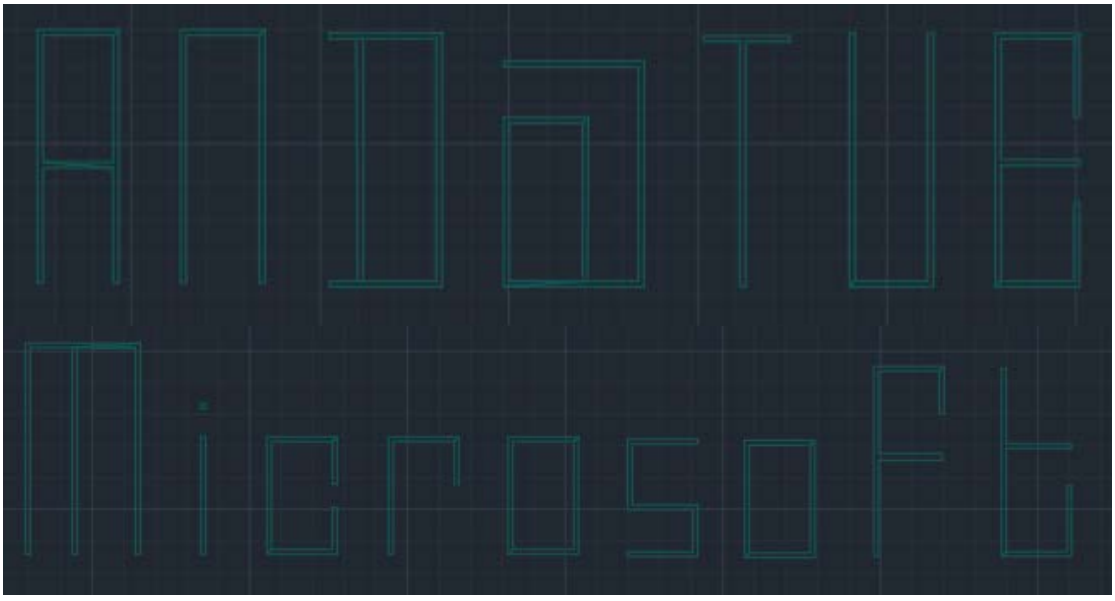

*Figure 29: Image of the complex designs from Autocad of the phrases 'AND@TUE' and 'Microsoft'.*

## 3.4 Metalorganic vapour phase epitaxy

Metalorganic vapour phase epitaxy (MOVPE) is a method to deposit thin crystalline layers on a surface. There are a few ways in which this growth can happen, mostly depending on the lattice mismatch. This is described in chapter 2.4. MOVPE is used in this research to deposit Indium Antimony (InSb) on an InP substrate. The Indium and Antimony reach the chamber as precursors, Trimethyl-Indium (TMI) and Trimethyl-Antimony (TMSB). The temperature in the chamber results in cracking or pyrolysis of these molecules. The amount of precursors which have lost their side chains is given by the cracking efficiency as illustrated in appendix 8.2: B. If the atoms/precursors will stick to the surface or not depends on the sticking coefficient. This sticking coefficient gets lower when the temperature increases. The atoms sticking to the surface can diffuse on the surface. As the atoms can't nucleate on a SiN layer, openings in the SiN have been made to expose the InP substrate underneath. This is explained in chapter 3.7. The atoms can form a nucleation there and result in InSb growth. The shape, crystal structure and defects depend on the substrate and the lattice mismatch between the substrate (InP) and InSb. These steps are shown in figure 40.[37] The pressure in the glove box is slightly higher (2mbar) than atmospheric pressure, with a concentration of $h_2o$ and $h_2 < 1\ ppm$. This ensures that in case of leakage the glove box will not get contaminated.

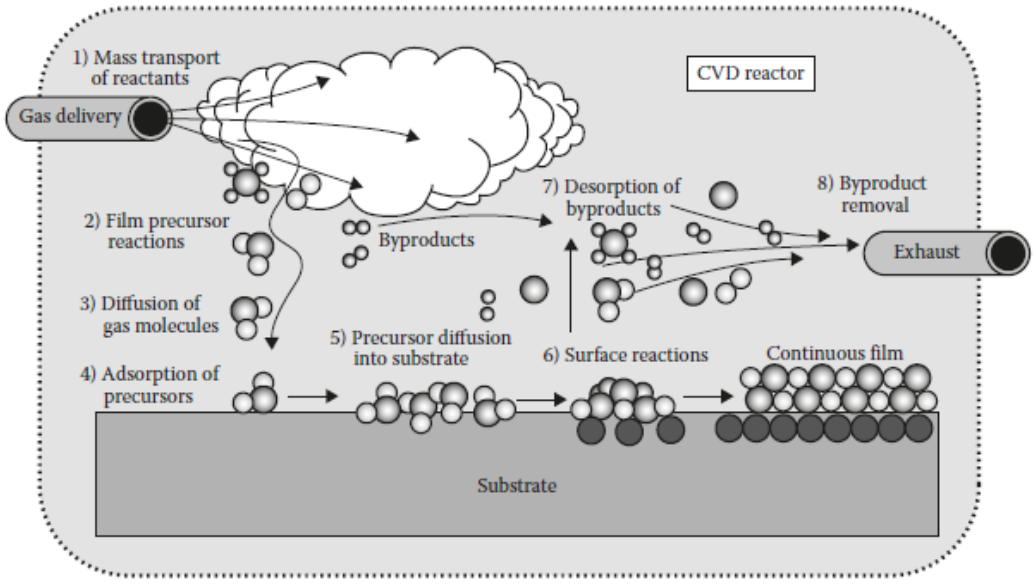


*Figure 30: Schematic view of the processes happening inside a MOVPE. A main gas flow ensures the continuous supply of precursors. The precursors can crack and transport to the surface. Where they can stick to the surface depending on the sticking efficiency. They can diffuse across the surface and form a nucleation..*

To ensure even distribution across the surface, the wafer rotates slowly around its axis. In around 6 seconds the wafer completes one rotation. The substrate is put on a heater to crudely control the temperature of the substrate, hereby controlling variables like the sticking coefficient, cracking efficiency, diffusion and desorption. In this experiment the temperature of the heater was 460°C. The temperature of the wafer would approximately be 30-40°C less, so 420-430°C. This is due to the material between the heater and the wafer surface and due to the air flow over the surface. The ratio of Indium compared to Antimony has a huge effect on the growth, as has the total

volume and flow of precursor gas. The ratio of the precursors in the main gas flow is not the same as the ratio of the corresponding atoms available for growth. The cracking can alter the ratio drastically. The ratio of precursors in the chamber is called the normal V/III ratio and the ratio of atoms available for growth is called the effective V/III ratio, where the cracking efficiency is included.

To calculate the normal and effective V/III ratios, first the vapour pressure needs to be calculated as it relates to the tendency of the precursors to evaporate from the liquid. The precursors are in a so called bubbler. A flow of $H_2$ bubbles through the precursor liquid taking some material with it. After calculating the vapour pressure the molar flow can be calculated. With help of the total volume flow the molar fraction is known. The ratio between the molar fractions gives the normal V/III ratio. Involving the cracking efficiency will give the effective V/III ratio. The exact steps and equations are shown in appendix 8.2: B

Using the best recipe for InSb networks (12.5sccm TMI and 37.5sccm TMSb, molar fraction of 3.49E-7 and 1.49E-3 respectively), a normal V/III ratio of 4282.1 is found while following the guide. The effective V/III ratio is 962.9. This difference is huge and caused by the partially cracked TMSb. All of the TMI precursor material is available for growth, while only around 20-25% of the TMSb precursor material is.

## 3.5 Scanning electron microscope

In this research a scanning electron microscope (SEM) from ZEISS has been used. This Gemini 1 is a field emission SEM and is designed for high resolution imaging. It has a vacuum system operating at $> \ 5 * 10^{-5}$ Torr. The SEM works by focusing a beam of electrons that targets the surface. From electrons reaching the detector an image of the sample can be made. The electrons can reach the detector after their interaction with the atoms, this can happen in various ways and is described in the next paragraph. The electron beam moves in a raster scan pattern across the surface to get an image of a bigger area. The resolution can be better than 1 nanometre.

On the left side of figure 41 a typical SEM image is shown of a trench in the SiN mask with InSb nucleations. By looking at the contrast it is possible to distinguish different regimes. Brighter areas are usually caused by sharp edges or higher objects. In this case, the two vertical white stripes are the edges of a nanostripe. This is basically an opening in the SiN mask, exposing the InP wafer underneath. An illustration of a typical nucleation is shown on the right side. Where the InP substrate is blue, the SiN mask is green and the InSb nucleation red. With this knowledge it is possible to tell that the darkest areas are the InP, on which 3 nucleations can be spotted. In the middle the interpretation of the SEM image is shown with corresponding colours for convenience. More information about the SEM can be found in appendix 8.3: C.

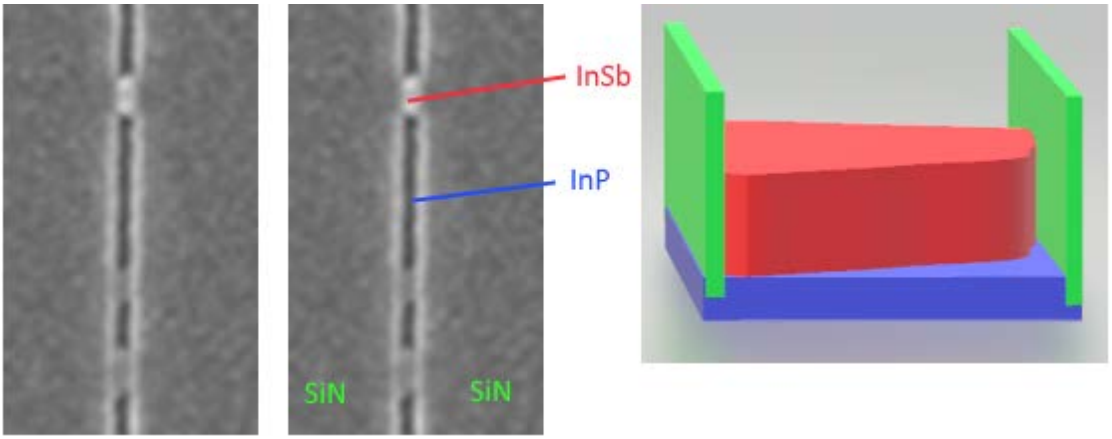


*Figure 31: On the left side two typical SEM pictures are shown, the different materials are pointed out. On the left side a 3D animation is shown. Where the green represents the SiN, the blue part is InP and the red block is the InSb nucleation.*

### 3.6 Transmission electron microscope

A Transmission Electron Microscope (TEM) is utilized to check the crystal structure and defects of the nanodevices. A TEM uses a beam of electrons transmitting through the sample to get an image. Usually a small ultrathin filament(<150nm thick) of the sample is required. The interaction of the electrons with the atoms, while passing through the sample, is used to form a magnified and focused image. The high resolution is basically due to the smaller Broglie wavelength associated with electrons compared to light.

The theoretical maximum resolution can be calculated as follows:

$$d = \frac{\lambda}{2n\,sin(a)} \approx \frac{\lambda}{2NA} \tag{4}$$

With the Broglie wavelength :

$$\lambda_e = \frac{h}{\sqrt{2m_0E\left(1+\frac{E}{2m_0c^2}\right)}} \tag{5}$$

Magnetic lenses are used to guide the electrons through the column. The angle of convergence can easily be changed by varying the electrical current through the coils. The mean free path of the electrons needs to be bigger than the distance from the source to the image recording system. This requires a vacuum system. Typical values are around $10^{-5}$ Torr. A schematic view of the TEM column is shown in figure 42. [38]

The scanning TEM is used in different modes. One of which is the high angle annular dark field mode (HAADF-STEM). An annular dark field(ADF) method avoids generally the main beam and only detects the scattered electrons with an ADF-detector. The optics distinguishing between dark and bright field modes is put after the specimen. The high angle part originates from the high angle at which the detectors look at the transmitted electrons. Only Rutherford scattered electrons, scattered by the nucleus of the atoms, are used to form the image. This method is highly sensitive to the number of atoms in the specimen, hence the requirement of ultrathin filaments.

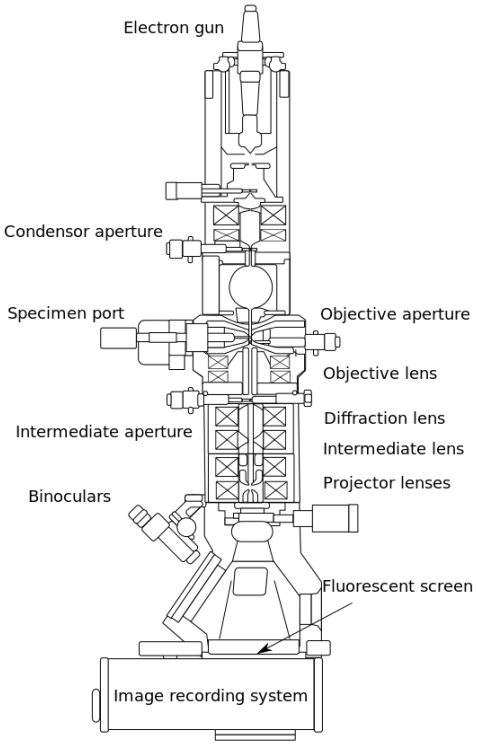


*Figure 32: A schematic view of a typical TEM. With the electron gun on top, passing through the specimen and various lenses before reaching the image recording system.*

In contrast, bright field transmission electron microscopy (BF-TEM) forms an image of the main electron beam passing through the sample. Where on some places the beam is weakened due to interaction with the crystal lattice. Image 43 shows an InSb network. For the left image the BF-TEM mode was used, while the right image was made using the HAADF-STEM mode.

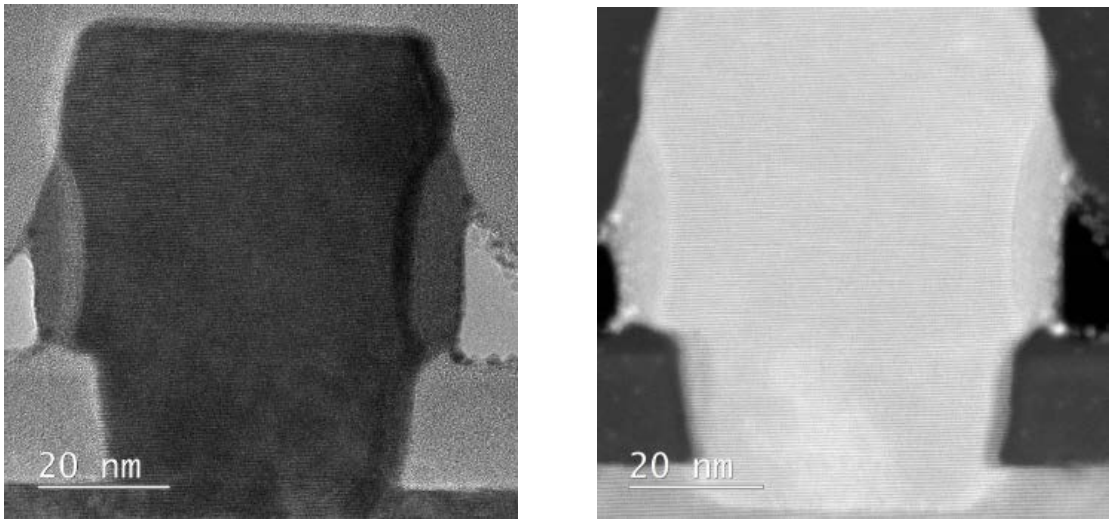


*Figure 33: Two images of the same InSb in-plane wire. The left image was produced using the BF-TEM mode. Only looking at the Rutherford scattered electrons. The right image was made using the HAADF-STEM mode, looking at the weakened beam directly.*

For spotting the misfit dislocations and defects in the nanowire, HAADF-HRSTEM has been used. (HR standing for high-resolution). This is shown in figure 44 on the left side. Spotting the misfit dislocations is easier by performing a fast Fourier transformation (FFT). The horizontal lines in figure 44 on the right side represent the crystal planes. The red circle shows an area where one plane suddenly splits and becomes two planes (a misfit dislocation). This is caused by the lattice mismatch between InP and InSb.

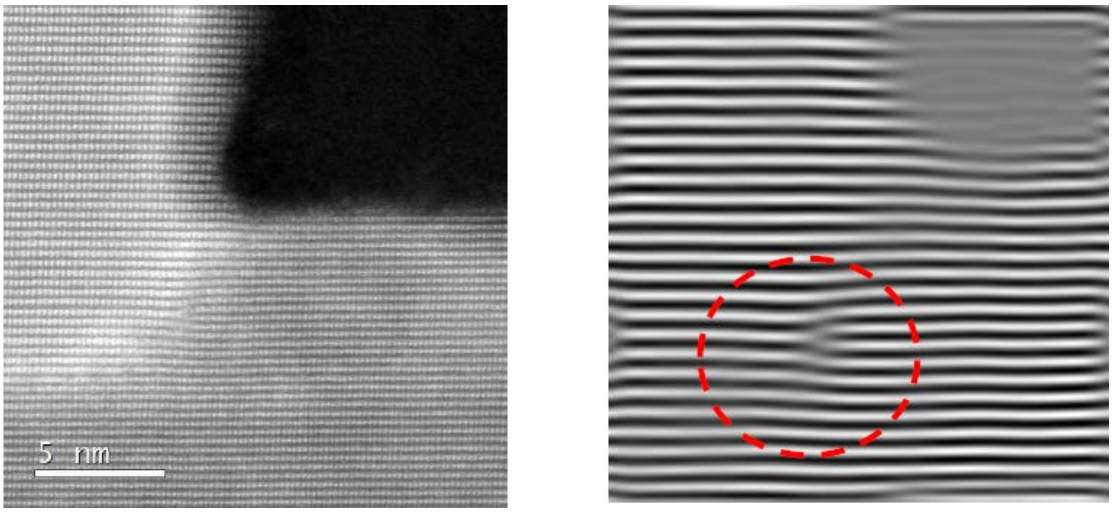


*Figure 34: The left image shows an HR-STEM image of the interface between the InSb and the InP. Due to the lattice mismatch several misfit dislocations are expected. The right image is a fast fourier transformation of the interface. Clearly visible is the misfit dislocation encircled in red.*

### 3.7 Sample preparation

A 2 inch undoped InP(111)B wafer from AXT© has been used as the substrate. With an offset in crystal orientation of (111)±0.5° and a (0-11) ±0.5° flat. InSb is grown directly on top of the InP on a selective area. It is important to share that the lattice mismatch between InP and the InSb is huge, around 10.4%. The sample preparation process before growth is shown in figure 45.[34] The surface of the wafer is first deoxidized with a 3 minutes Phosphoric acid dip. Then a SiN layer of around 20nm is deposited on top of the wafer using PECVD, the thickness of the SiN layer is checked with a refractometer. Afterwards a positive resist (ZEP520A) in combination with fullerene (buckyballs) is put on the SiN layer, preparing the wafer for the electron beam patterning. The electron beam targets the positive resist with electrons according to the design, cutting the polymers locally into small pieces. Then the wafer is developed, removing the small pieces of polymer. The RIE is used to transfer the design from the positive resist into the SiN layer, with help of n-amyl acetate and MIBK-IPA, exposing the InP wafer underneath. A lift-off using PRS3000 is performed to remove the negative resist. Before the growth the sample is cleaned using an $O_2$ plasma and another phosphoric acid dip to deoxidize the surface. To make better use of the available materials the wafer has been cut in smaller pieces. Selective area growth is performed with a MOVPE to deposit InSb in the nanostripe designs.

In Appendix 8.4: D each step of the fabrication has been explained in more detail.

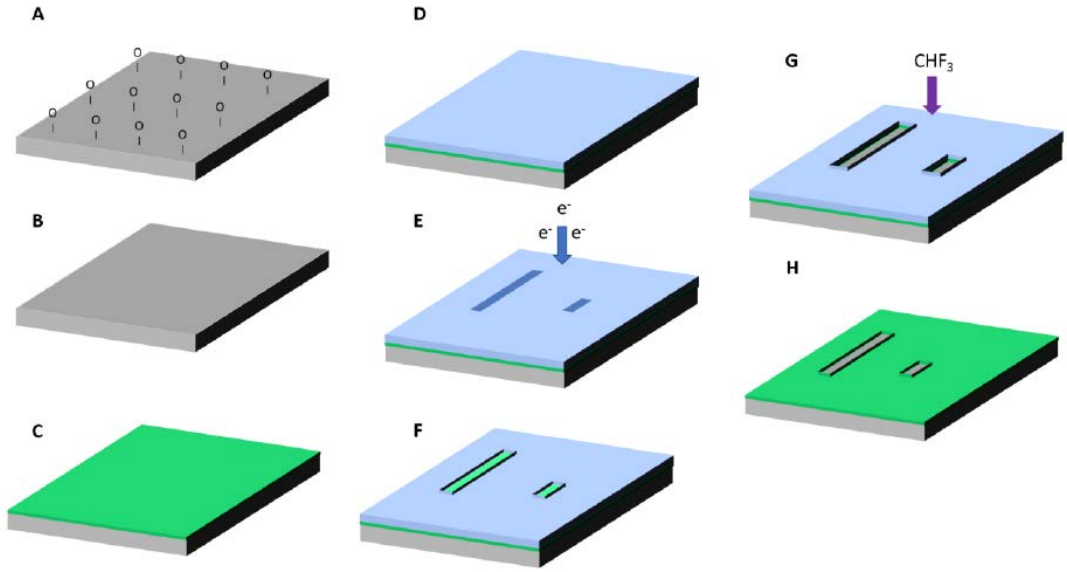


**A** oxidized wafer

**B** oxide removed (dil. H3PO4 dip)

**C** SiN layer deposited (PECVD)

**D** photoresist layer (spin coater)

**E** Ebeam exposure

**F** Result after Ebeam

**G** Reactive ion etching (RIE)

**H** Lift off/ removal of resist layer

*Figure 35: Illustration of the fabrication steps to go from an oxidized InP wafer to an InP wafer with a SiN mask with the design engraved into it. Here it is ready for growth . For every step an explanation can be found at the corresponding letter.*

# 4 Results and Discussion

In this section the results of the research are shown and discussed. As the research is constituted by several main subjects, the result section is divided in multiple segments. In Chapter 4.1 the search for optimal growth conditions is described. Here the main goal was to find the best parameters for growth. Chapter 4.2 shows the study of the nucleation mechanism. How and where does the InSb nucleate, which facets does it form, what is the influence of the growth parameters and what is the difference between the (110) and the (112) orientation.

Chapter 4.3 is dedicated to the study of the growth mechanism and the defects forming due to the lattice mismatch. A TEM analysis was performed to study the defects. Aharonov-Bohm measurements were performed on a well grown InSb hashtag structure, the results are shown in chapter 4.4.

A side project is the study of the flakes. Sometimes the InSb likes to form a 2D structure on top of the SiN mask when it outgrowths the trench in the SiN mask. The goal of this experiment is to make these flakes as big as possible. The results are shown in chapter 4.5.

The yield of the main experiment is ~60%. A special step called thermal annealing is performed to remove the native oxides from the InP surface in the trenches. This could improve the yield. The results of adding this thermal annealing step are shown in chapter 4.6. Finally, the first results of the complex designs are shown in chapter 4.7.

## 4.1 In search of the optimal growth conditions

The optimal conditions to grow InSb directly on top of InP(111)B were found by varying one condition at a time. The best result by trial and error was while having a TMI molar fraction of 3.49E-7 and a TMSb molar fraction of 1.49E-3. This corresponds to 12.5 sccm and 37.5 sccm respectively. The possible variation in growth temperature is very limited due to the Phosphor evaporation and cracking efficiency of the TMSb precursor thus cannot be varied much. As a volume flow of 6000 sccm and a growth window of 30 minutes resulted in nicely filled networks, this was kept the same as well. So only the V/III ratio has been varied.

To investigate the effect of the V/III ratio, two separate series have been performed. One while changing the TMI concentration while keeping the TMSb constant at 37.5 sccm and one while changing the TMSb concentration while keeping the TMI constant at 12.5 sccm. The choice of investigating the effect of both concentration separately instead of only changing the V/III ratio was made because the growth seems to be Indium limited. This would be better visible by separating the two.

Figure 46 has been made to illustrate the influence of the TMI concentration. One SEM image has been taken from every TMI concentration sample which seemed to be the average of that sample. The TMI concentrations are shown in the right bottom for every image, where ‘cc’ is short for ‘sccm’. The SEM images of the same design have been used for easier comparison. Only the length and width of the designs vary a bit sometimes. (In that case the correct size designs were not representative for the sample). Increasing the molar fraction of TMI in the chamber seems to have the same effect as increasing the growth window. The growth seems indeed limited by the amount of Indium available. The trenches are only filled partially for lower concentrations of TMI, increasing the concentration results in longer and thicker nucleations. After 17.5 sccm of TMI another trend appears. flake forming seems to happen for higher concentrations of TMI. This could be used in the flake project described in chapter 4.5.

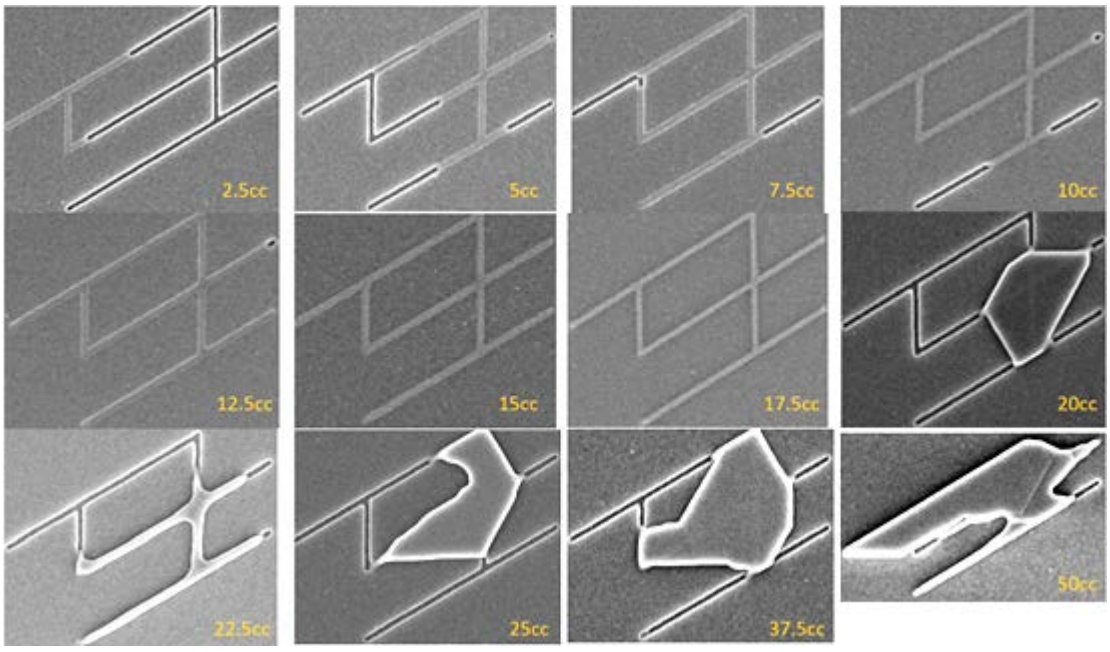


*Figure 36: SEM images of the TMI series. The growth seems to be Indium limited. After 17.5 sccm of TMI flakes start to form.*

The same procedure has been done for the TMSb series. In this case the TMSb concentration didn't show the same kind of influence as the TMI. This could be due to the high V/III ratio, resulting in an excess of Antimony. The only interesting observation was for the two lowest amounts of TMSb as shown in figure 47. There seem to be a lot of nucleations per design. This could be caused by a decreased diffusion length. Another possible explanation is that these samples were more oxidized, thereby passivating the surface, promoting island growth.

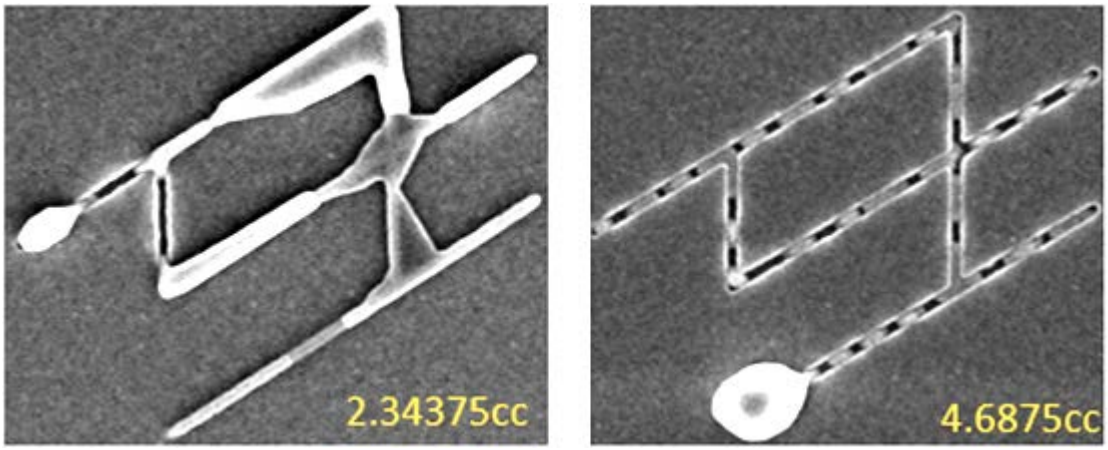


*Figure 37: Two SEM images of the lowest concentrations of TMSb in the Antimony series. Both seem to have a lot of nucleations in the design.*

With this information, the optimal parameters were found. The conditions found earlier seem to indeed give the best result: a TMI molar fraction of 3.49E-7 and a TMSb molar fraction of 1.49E-3. Slightly higher concentrations of TMI would result in thicker wires but decreases the yield. Thus the highest yield was found with a V/III ratio of 962.9, and is shown in figure 48. A yield of ~60% can be achieved with these conditions. Each design has been repeated 4 times above each other. When zooming out to see more structures in one view, only the bad grown structures are visible. The sharp edges related to flake forming and other bad growth give a high contrast with the SiN mask. The electrons from the SEM scatter more at the edges. So by looking at the

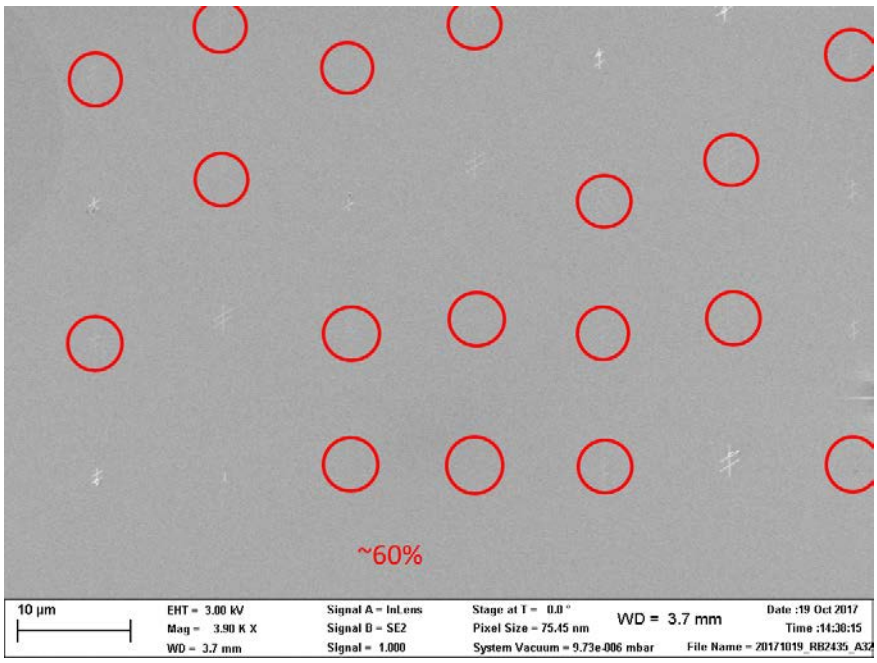


*Figure 38: SEM image showing the yield of the normal growth. Around 60% is grown correctly.*

places where no structure is visible but where one should be, we can determine the yield. For convenience these places are encircled in red. This relates to a yield of ~60%. After taking this image every design was checked while zoomed in to ensure that they grew well.

A few well grown structures are shown in figure 49. Showing that the semiconductor part of the devices can be grown successfully. To form the hybrid structures a superconductor should be evaporated on top of these InSb structures. The next step is to improve the yield. Varies methods can be examined such as a buffer layer to accommodate for the lattice mismatch. A very promising method has already been tested, the thermal annealing of the surface before growth. Left over native oxides could change the surface energy and thereby changing the crystal growth mechanism as described in chapter 2.4.1. The results of thermal annealing are shown in chapter 4.6.

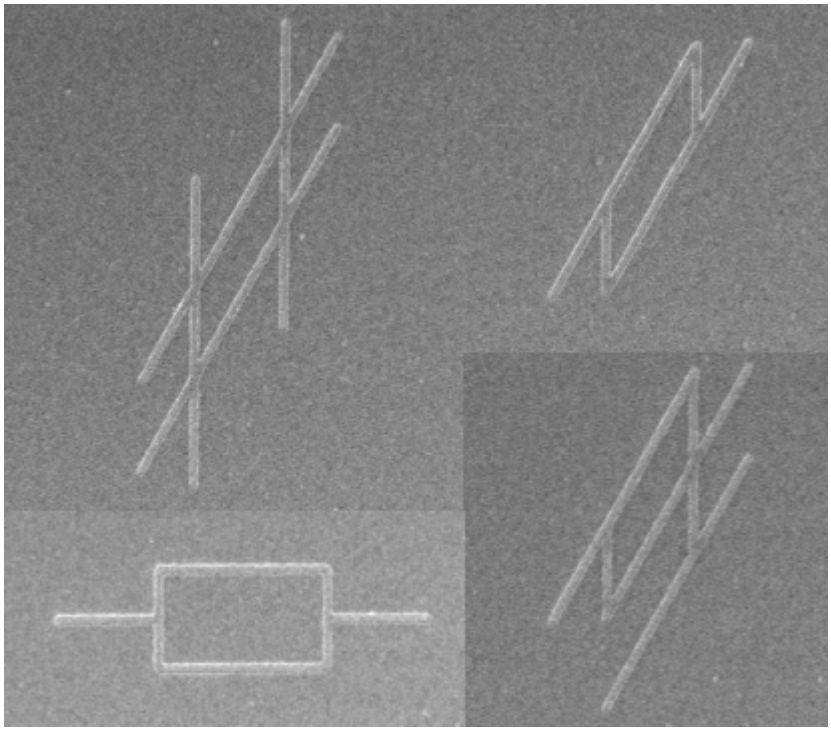

*Figure 39: 4 SEM images showing good results while growing with the optimum conditions. All designs grow well.*

The structures on an InP(111)B wafer are expected to grow nicely in the (112) directions with a 60° angle as shown in figure 50 on the left side. Interestingly stripes with a 90° angle to a (112) direction grow nicely as well. This would mean that the (110) directions work as well. To examine this phenomena a rainbow design with different angles has been used. This is described in chapter 3.3.1. The results prove that the (110) orientation works as well. This is also shown in figure 50 on the right side. In the next experiments these two orientations are compared.

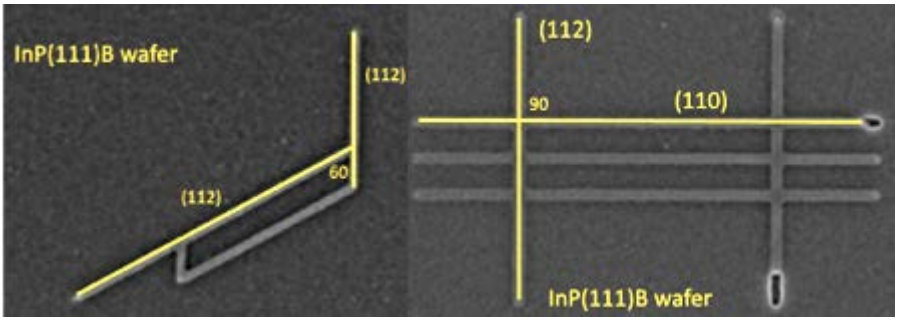


*Figure 40: Left image shows a grown InSb network with only (112) directions and a 60 degree angle between them. The right image shows a design with a combination of the (112) and (110) direction with a 90 degree angle between them. Both designs seem grow well and are grown on an InP(111)B wafer*

## 4.2 Study of nucleation mechanism

This chapter is dedicated to the investigation between the (110) and (112) crystal orientations along the (111) surface. The different crystal orientations could have different growth mechanisms. For structures with a 90 degree angle both directions would have to be used. The growth of the InSb devices could be divided in two steps, the nucleation and the additional growth. First the nucleation has been examined by growing for 1 minute and measuring the average distance between nucleations in a trench. Multiple nucleations form in a nanostripe of 50 μm, using the nucleation design made for comparing (110) and (112) as described in chapter 3.3.4. Further research into the crystal facets of the nucleation is done in chapter 4.2.3

The variables that have been varied to examine the nucleation are the TMI and TMSb concentrations in the chamber For each experiment one variable has been changed while having the other variables fixed. For the data in chapter 4.2.1 the TMI concentration has been altered, while for chapter 4.2.2 the TMSb concentration has.

### 4.2.1 Indium series

In this chapter the results of the Indium series for investigation of the nucleation mechanisms are shown. The goal of this experiment is to see how the average distance between nucleations changes when changing the TMI concentration and to see if there is a difference between the (110) and (112) direction. Multiple nucleations per network could cause defects when not merged correctly, therefore this is an important aspect for good growth. The TMSb concentration is fixed with a molar fraction of 1,49E-3. The temperature is set at 460°C and the volume flow at 6000 sccm. A growth window of 1 minute is used to investigate the nucleation mechanism. A growth window of 1 minute is used because longer growth would result in larger nucleations, this makes it harder to see where the nucleations started.

The design used for this experiment is shown in figure 51 on the left. Where both the (110) and (112) directions are present. The right side shows two nucleation in a (112) direction nanostripe delineated in red. The distance is measured between the nucleations as shown in the figure. The distance between at least 101 nucleations (except for very low TMI concentration) has been measured and averaged. There could be a correlation between this average distance between the nucleations and the diffusion length.

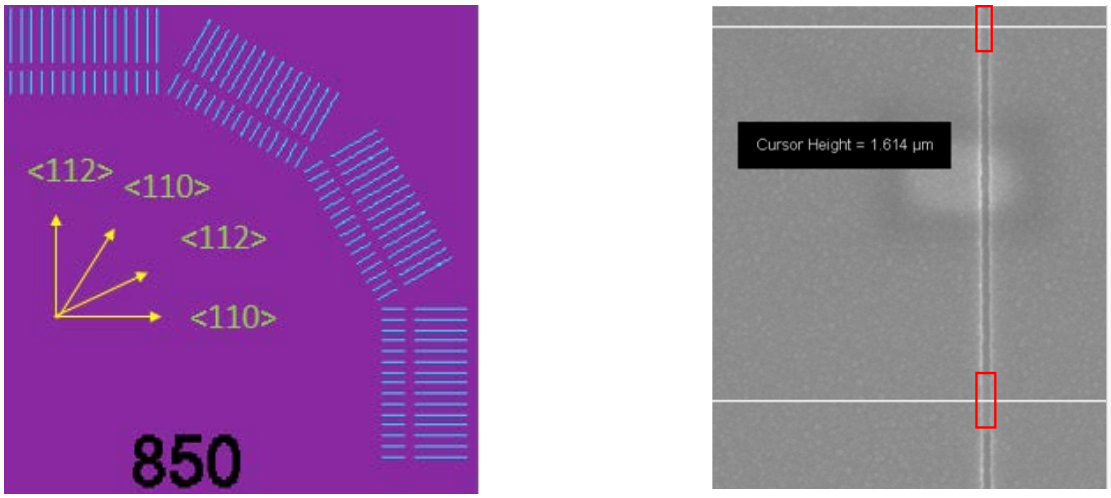


*Figure 41: Left shows the rainbow design with both the (112) and (110) directions. 15 Stripes of 20 and 50 micrometer are etched in each direction. Right shows the analyzing method. The distance between nucleations has been measured. The two nucleations are encircled in red.*

For each TMI molar fraction every distance between two nucleations in several nanostripes for both the (110) and (112) has been measured. To be able to statistically get a result at least 100 distances are measured for each data point. The average, sigma and uncertainty in the average have been calculated from this data. With the uncertainty in the average being sigma divided by the square root of the number of data points. The distance between nucleations is not exactly the same in the same nanostripe because the nucleation location is mostly random. This results in a large distribution as shown in figure 52. This is a histogram of distances occurring when having a TMI concentration of 20 sccm.

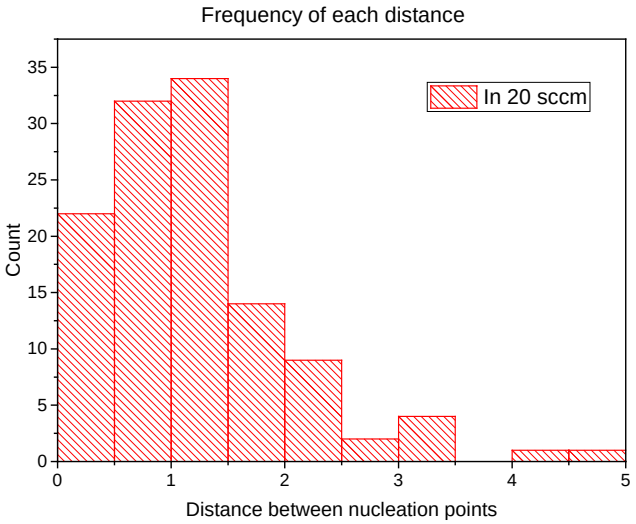


*Figure 42: Histogram with the frequency of each distance for the TMI 20sccm. The distribution looks normal or Gaussian, indicating a random nucleation location.*

The large distribution in distances between two nucleations results in a large sigma interval. However, this does not mean that the uncertainty in the average is huge. Figure 52 also shows that the distribution of the distances is 'normal' or Gaussian, suggesting that it is a random process without additional processes. The final result of the Indium series is shown in figure 53. With the mean distances including uncertainty in the mean and the sigma interval as a function of the TMI molar fraction in the chamber.

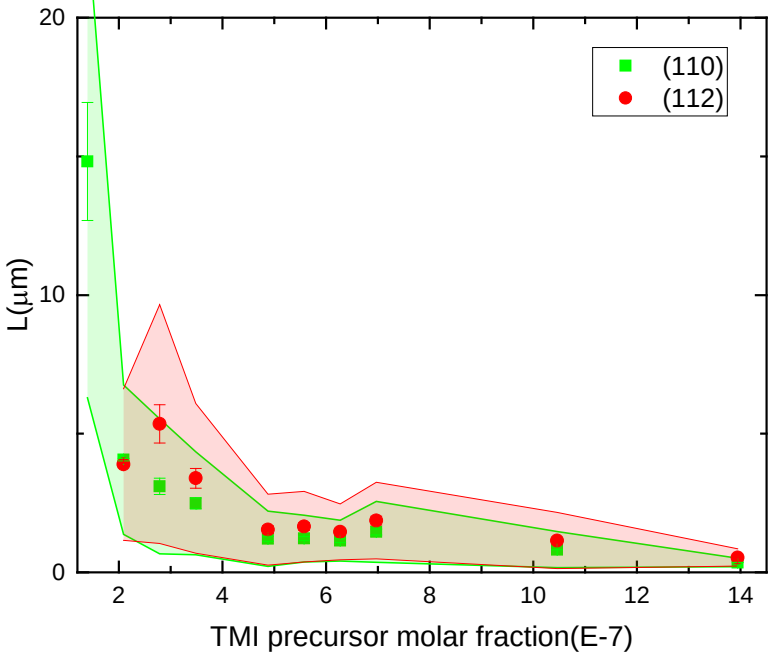


*Figure 43: Mean of the distances between nucleations with the uncertainty in the mean and the sigma interval as a function of the TMI molar fraction. Observe the difference between the (112) and the (110) direction.*

Figure 53 of the mean distance between nucleation per TMI molar fraction needs some further explanation. The (112) data point (red) for the TMI molar fraction of (6.97E-8) is not present. The nanostripes were completely empty in this case, making it impossible to measure the distance between nucleations and indicating a mean distance of more than 50 micrometre. Moreover, keep in mind that the red and green bundle are the sigma intervals, not the uncertainties. The uncertainties are so small that they are barely visible.

There are two interesting aspects in this graph. Firstly, the figure clearly shows an increase in the average distance between nucleations if the TMI molar fraction decreases. For concentrations below the 2.79E-7 it looks like the mean distance blows up, scarcity of nucleations under these conditions makes it hard to find enough datapoints. This could be caused by a shortage of Indium as results from chapter 4.1 show that the growth is Indium limited. This is interesting because the growth of a III-V semiconductor is usually limited by the group V. The second interesting observation is that almost all (112) data points are above the (110)'s. This would mean that in the (112) direction there are less nucleations per micrometre, so there is indeed a difference between the (110) and (112) direction. This difference could be caused by a different diffusion length of the materials for the two orientations. Less nucleations per micrometre would be beneficial for our devices, so the (112) directions would be the better of the two. The second datapoint seems to not follow this trend. The reason for this is unknown.

Note: Larger distances between nucleations does not have to be directly related to a larger diffusion length of the adatoms. Different variables such as passivation of the surface or just a shortage of Indium could also cause it.

### 4.2.2 Antimony series

In this section the Antimony series results are discussed. In same line as the Indium series discussed in the previous chapter, every variable except for the antimony molar fraction has been fixed. With a growth temperature of 460°C, an Indium molar fraction of 3,49E-7 and a volume flow of 6000 sccm. The distance between nucleations has again been measured for both the (110) and the (112) direction. The growth window is again 1 minute, making it easier to spot where the nucleation started.

In figure 54 the (110) direction is again shown in green and the (112) direction in red. The horizontal axis is this time logarithmic due to the spread of molar fractions of TMSb that were used for this experiment.

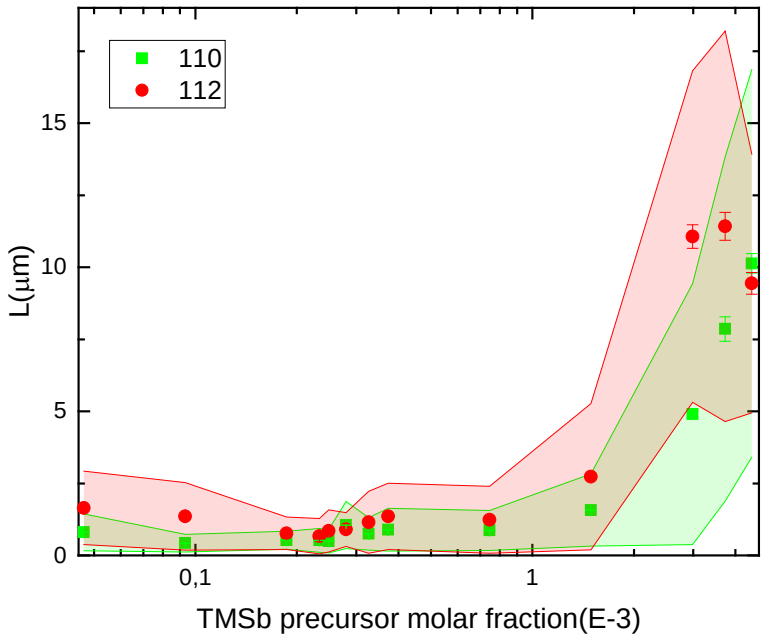


*Figure 44: Plot of the mean distance between nucleations for varying TMSb molar fractions. The (112) directions again seems to have less nucleations per micrometer. High amounts of TMSb cause a huge increase in the mean distance.*

This time there are 3 interesting aspects of the graph. For higher amounts of TMSb molar fractions the average distance between nucleations seems to go up rapidly. This time it cannot be explained by a limited amount of Indium available for growth as the TMI concentration stays the same. However, it is possible that high concentrations of TMSb could passivate the surface and thereby decrease the growth. The normal V/III for a molar fraction of 2.99E-3 is 8564.3. Meaning that more than 8500 TMSb molecules are present in the growth chamber for 1 TMI molecule. The second interesting aspect is that again the (112) direction has a larger distance between nucleations on average, meaning less nucleations per micrometre and therefore slightly better for the network application. Thirdly, around 1.87E-4 TMSb there seems to be a small dip in the graph. This corresponds with an effective V/III ratio of 120.4, calculated by using the guide in Appendix 8.2: B. Figure 55 shows a zoomed in image of this region, with a linear scale this time.

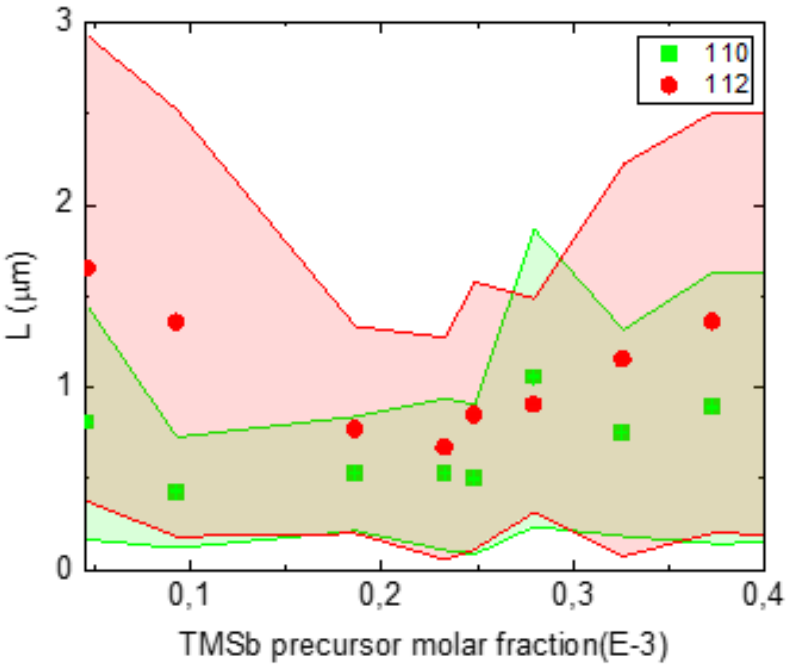


*Figure 45: Zoomed in image of the dip-region in the Antimony series. Multiple molar fractions around this dip have been studied to be able to call it a real significant dip.*

Multiple molar fractions of TMSb around the dip have been grown and analysed. There clearly seems to be a downward and upward trend for both the (110) and the (112) orientation, where the dip in the (112) is more pronounced. The cause of this increase in nucleations is not known. It could be the turning point where the system goes from an Antimony rich growth to an Indium rich growth. Whatever the cause may be, for network devices it is best to stay away from this dip, as multiple nucleations per device could cause defects when merging.

### 4.2.3 Nucleation process and side facets

In this chapter the nucleation process is discussed. The start settings are an InP wafer, a SiN mask for selective area growth and a flow of TMI and TMSb over the surface, where due to the temperature all of the TMI is cracked and the TMSb partly. As it can't nucleate on the SiN surface, the only place it can is in the trenches where the InP is exposed. The nucleation seems to happen near the SiN wall in the trench, as figure 56 illustrates. The SiN wall is green, the InP substrate blue and the InSb nucleation is shown in red. Figure 57 shows a SEM image of a nucleation starting near a SiN wall. The nucleation is barely visible, therefore it is delineated with red on the right side.

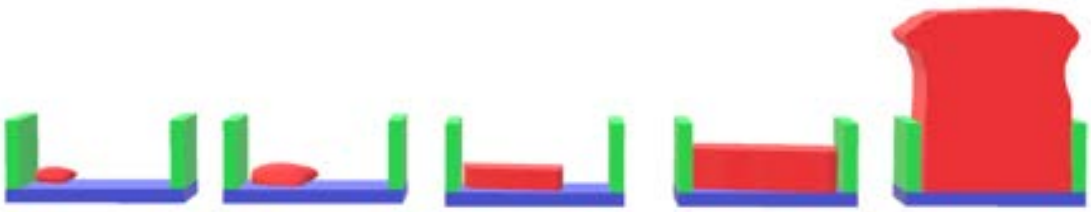

*Figure 46: Illustration of a side view of a nucleation with the SiN mask in green, the InP substrate in blue and the InSb nucleation in red. The nucleation seems to start at the edge of the trench. If it gains a curtain volume it forms visible favorable facets. The top of the nucleation is flat (111) direction. After a while the InSb can grow thicker than the SiN mask.*

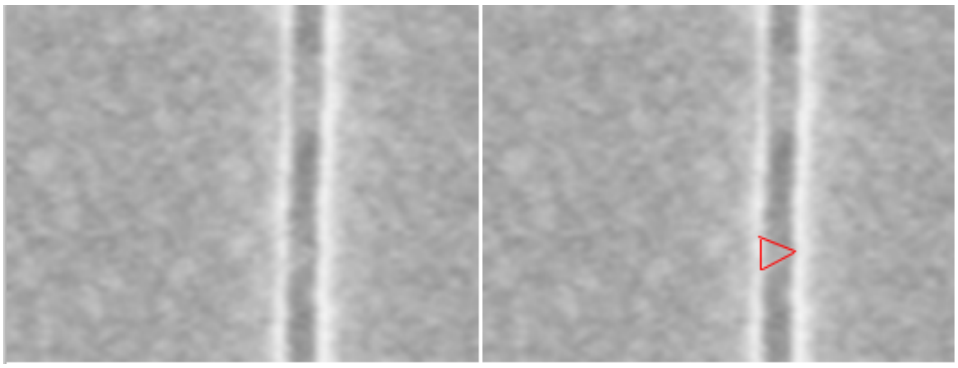

*Figure 57: SEM image showing a nucleation starting near a side wall. On the right side the nucleation is delineated in red.*

Figure 56 shows the side view of a nucleation. The nucleation seems to start (most of the times) at the edge of a trench near the SiN wall. Maybe because of rough edges , it could be explained by comparing it with a liquid flow, where the velocity goes down near the edges. This process is shown in figure 58.[39] Rough edges will cause a lower velocity in the ficinity of the edge, making it easier to nucleate.

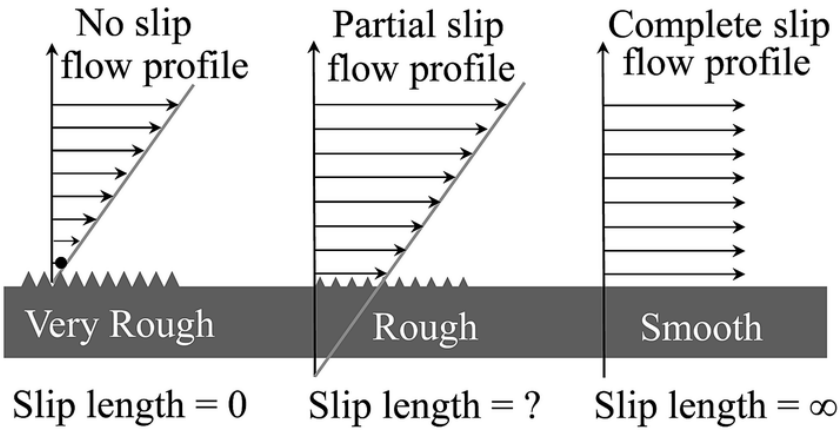

*Figure 47: Flow profile of a liquid material near an edge. The roughness of the edge determines the slip length. The rougher the edge, the lower the velocity near this edge.*

After some growth visible low energy facets start to appear, such as the flat top of the nucleation which is a (111) facet as it runs parallel to the (111) substrate. If the growth window is even longer the nucleation can be thicker than the SiN mask. The InSb seems to stay away from the SiN mask. Figure 59 shows a top view of the same nucleation. Observe again the nucleation at the edge and the formation of other facets. If the InSb grows thicker than the SiN mask it starts to grow thicker than the trench width.

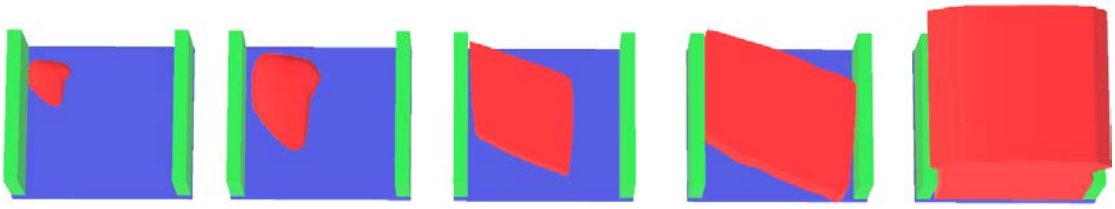

*Figure 59: Illustration of a top view of a nucleation with the SiN mask in green, the InP substrate in blue and the InSb nucleation in red. Observe again the facets forming after some time and the nucleation starting at the edge. After some time the InSb can outgrowth the SiN mask and grows thicker than the trench width.*

The facets that form after some time are interesting. They could tell something about growth processes happening. The top of the nucleation is parralel to the substrate, so a [1 1 1] facet. In the case of a wire in the [1 1 -2] direction, the two side facets facing the SiN mask are a [1 -1 0] facet. The ends of the nanowire are different. One side seems to be inclined and flat while the other has two orientations like the sharp side of a knife. This phenomena resembles the shape of the nanosheets discussed in chapter 2.3.2 and analysed by Chun Yung Chi et al.[18] They suggest that the side facets are of the (110) family as well. For a wire in the [1 1 -2] direction, the inclined flat side facet would be a [-1 -1 0] facet, while the two facets at the other end would be a [0 -1 -1] and [-1 0 -1] facet. Figure 60 shows two SEM images, one of a wire in the (112) direction and one in the (110) direction. The suggestion of Chun Tung Chi et al. that the side facets are all of the (110) family is shown as well.

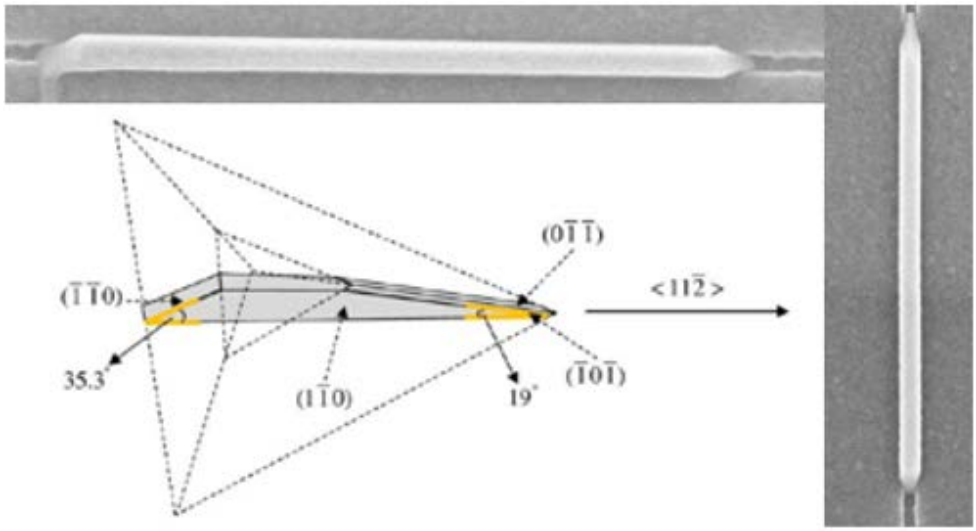


*Figure 48: Two SEM images showing a nanowire in the (112) and in the (110) direction. Both have an inclined side facet on one side and a sharp 2 facetted structure on the other side. The suggestion from Chun Tung Chi et al. is shown as well*

It seems plausible that the structure they investigated has the same facets as the InSb nanowires in this experiment. To check if this is indeed the case, a TEM image with a side view of the flat inclined facet is used. The angle should be around 35.3° to agree with them. Figure 61 shows the TEM image with the inclined angle.

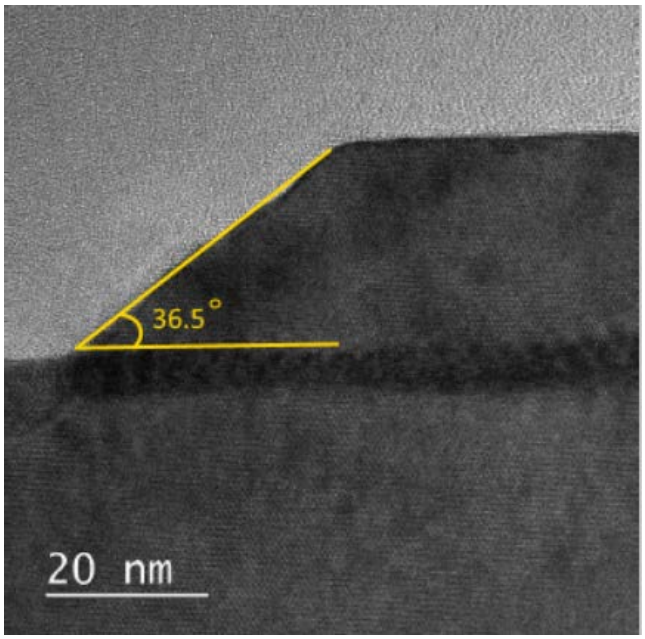


*Figure 49: TEM image of a side view of an inclined side facet. The inclined angle is around 36.5°.*

The inclined angle is around 36.5°. This is close to the 35.3° mentioned in literature. The uncertainty in this measured angle is big enough to call it plausible that the side facet is a [-1 -1 0] plane.

These side facets are visible in fully grown structures. Small nucleations also show favourable side facets as illustrated in figure 62. The angle with a line perpendicular to the SiN sidewalls of the trenches is around 30° when having a top view. The 30° angle is probably the start of the formation of one of the (110) side facets. The [-1 -1 0] facet would be perpendicular to the sidewalls when having a top view, this one is probably formed later. The other two side facets do show an angle around 30° when having a top view.

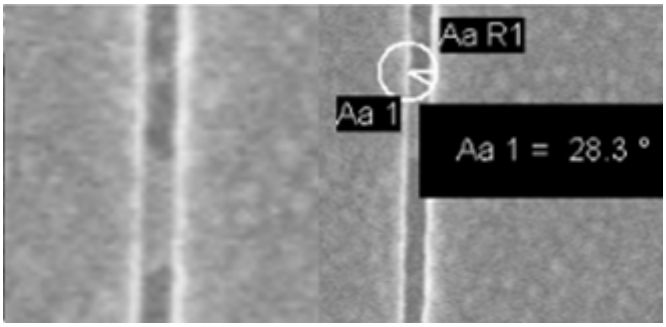


*Figure 50: SEM image of a nucleation already showing favourable side facets. The angle with a line perpendicular to the SiN walls of the trench is 30°*

## 4.3 Study of growth mechanism and defects

In this chapter the growth mechanism of the InSb nanowires and the defect are studied. To see if the additional growth is linear with time, the growth window has been varied. Non-linear growth could be an indication of multiple growth mechanisms. Other parameters are fixed at the values of the best recipe. TEM images are used to investigate the defects caused by the lattice mismatch and to see how crystalline the InSb is. A differentiation between the (110) and (112) orientation has been made to see if there is a difference. Chapter 4.3.2 shows the TEM results.

### 4.3.1 Time series

A time series has been performed to investigate how fast the nucleations grow and to see if this grow is linear. This time every variable is fixed except the growth window. The best recipe with a TMSb molar fraction of 1.49E-3, a TMI molar fraction of 3.49E-7, a temperature of 460°C and a total volume flow of 6000 sccm has been used. This time not the distance between nucleations but the length of the nucleations has been measured. The average length is expected to increase when increasing the growth window. The same rainbow design as with the Indium and Antimony series has been used with 50 micrometre long nanostripes in the (110) and (112) direction. Again discriminating between the two directions to see if there is a difference.

The first results showing the total covered area (the total length of InSb in a 50 micrometre nanostripe) for the (110) and the (112) direction are shown in figure 63. The results are from old time series, where less datapoints are available, see it as a rough sketch until the final data arrives. The data from the new time series are still being analysed at this moment.

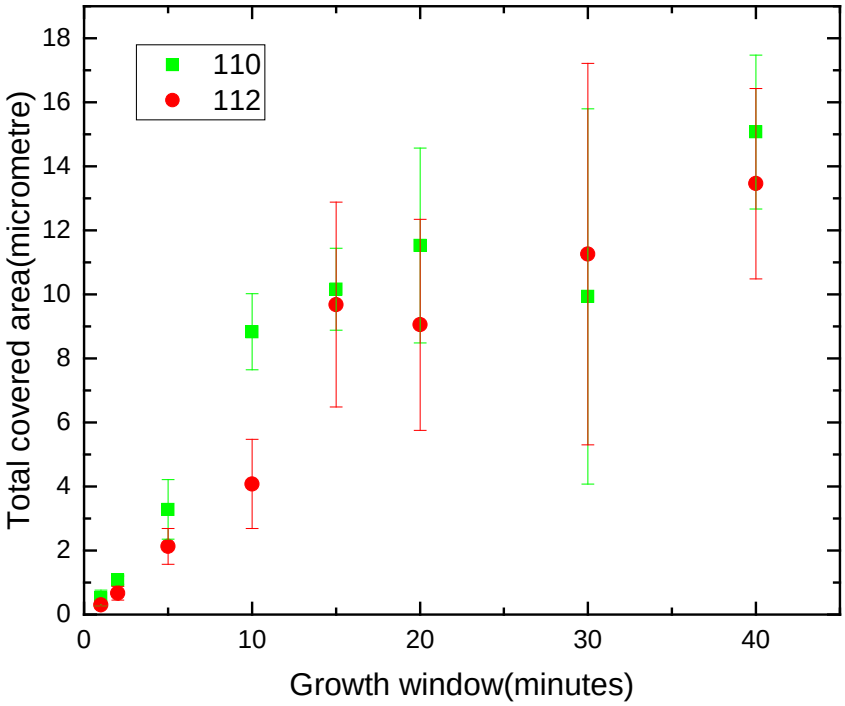


*Figure 51: Time series with the covered area as function of the growth window. A possible difference between the (110) and (112) directions is not visible. There is a clear linear trend.*

There is no visible difference between the (110) and (112) direction. There is however a clear linear trend. The total length of the nanostripe that is covered with InSb is linear dependent on the growth window. This is better visualised in the next graph. Figure 64 shows the total covered area in micrometre. This time the (110) and (112) direction are taken together and averaged to improve the statistics. The nucleations also started to grow wider as soon as they reached the height is the SiN mask. This width has also been taken into account.

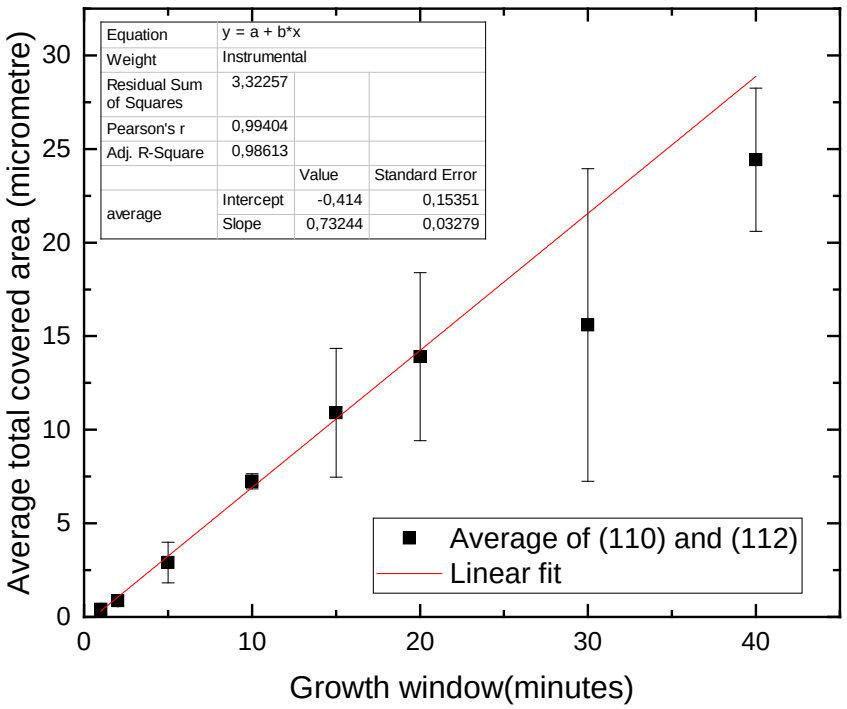


*Figure 52: Graph of the total covered area averaging the (110) and (112) direction as a function of the growth window in minutes. A linear trend is visible and a linear fit has been made.*

The slope of the linear fit tells us that with this recipe we are able to grow 0.73244 micrometre of InSb nanowires per minute.

Figure 65 shows a few SEM images of a structure grown while varying the growth window. The growth of structures instead of lines has also been analysed. The dependence on the growth window is shown on the right side. Again a semi linear dependence is found. After 20 minutes the trench is fully filled and the growth becomes less trivial.

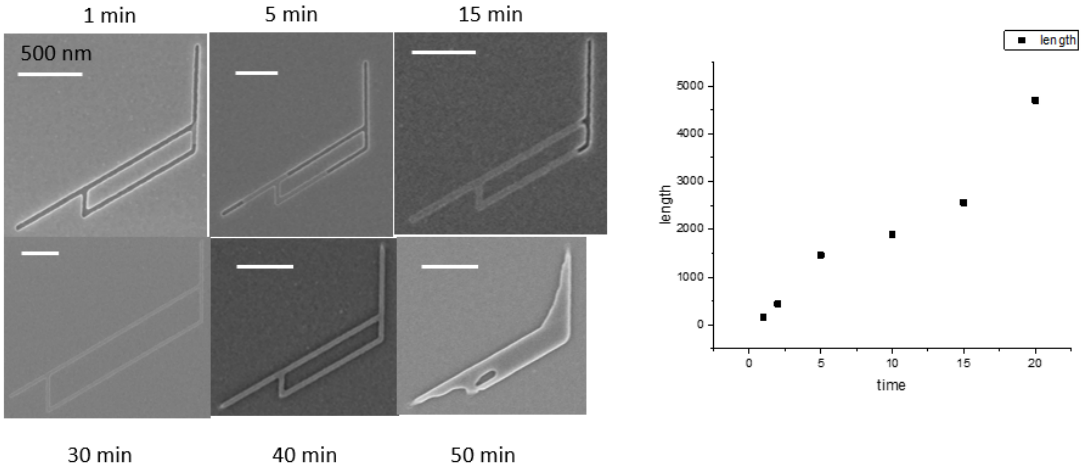


*Figure 53: Left side shows SEM images of structures with the same design grown with varying growth windows. The right image shows the length of the nucleations as a function of the growth window.*

### 4.3.2 TEM defect analysis

The TEM is used to check for the defects in the InSb crystal and at the interface. Different TEM-modes have been used, these are described in chapter 3.6. Here again the two directions (110) and (112) have been compared to check for differences. Furthermore on both an analysis has been done along the wire as well as by looking at the cross-section. To summarize the next section, the TEM results show no significant difference between the (110) and (112) orientation. This analysis is only performed on a few nanowires, if this is the case for every structure is not known.

#### 4.3.2.1 TEM on (112) cross-section

First TEM has been used on three wires in the (112) direction to look at the cross-sections. The wires are shown in figure 66 on the left side, where the red rectangle marks the spot where the thin filament was cut out. These structures were chosen to check for differences in wires with different heights. The left one is the tallest, the middle one the smallest and the right and is in the middle, as shown on the right side.

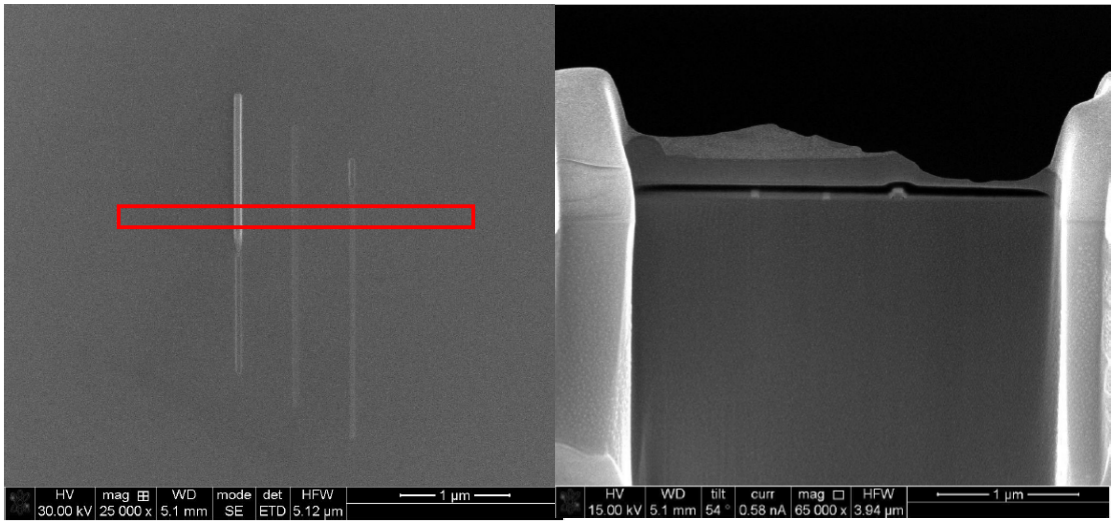


*Figure 54: SEM images, the left image showing the three nanowires of interest with different heights. The red rectangle marks the region where the filament was made off. The right image shows a side view, showing that the left nanowire is the tallest, than the right one and the middle one is the smallest.*

From these three structures an EDX mapping was done to examine the phosphor contamination in the InSb crystal. Figure 67 shows the result. The red is Antimony, the

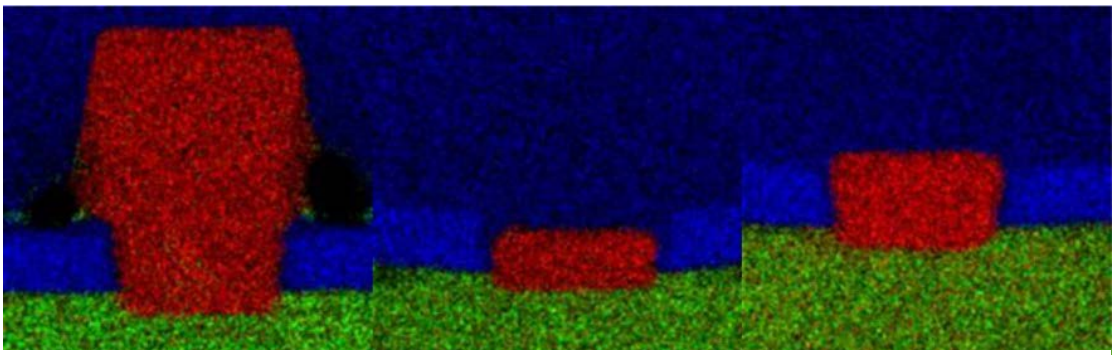

*Figure 55: EDX mapping of the Phosphor(green), Antimony(red) and Silicon(blue). The contamination of InSb by Phosphor seems to be small. The tallest structure is several times larger than the SiN mask.*

green is Phosphor and the blue is Silicon. Therefore the green is the InP, the red is the InSb and the brighter blue is the SiN mask. The red indicating the InSb is higher than the bright blue areas on the side representing the SiN mask for the tallest structure, therefore this structure is thicker than the SiN mask. There seems to be not much Phosphor contamination (green) in all three of the InSb structures.

After EDX mapping BFTEM and HAADF-STEM are used to check for defects. These methods are used with a magnification up to 300 000 times. Figure 68 shows the BFTEM and HAADF-STEM data for the three wires with a magnification of 250 000 times.

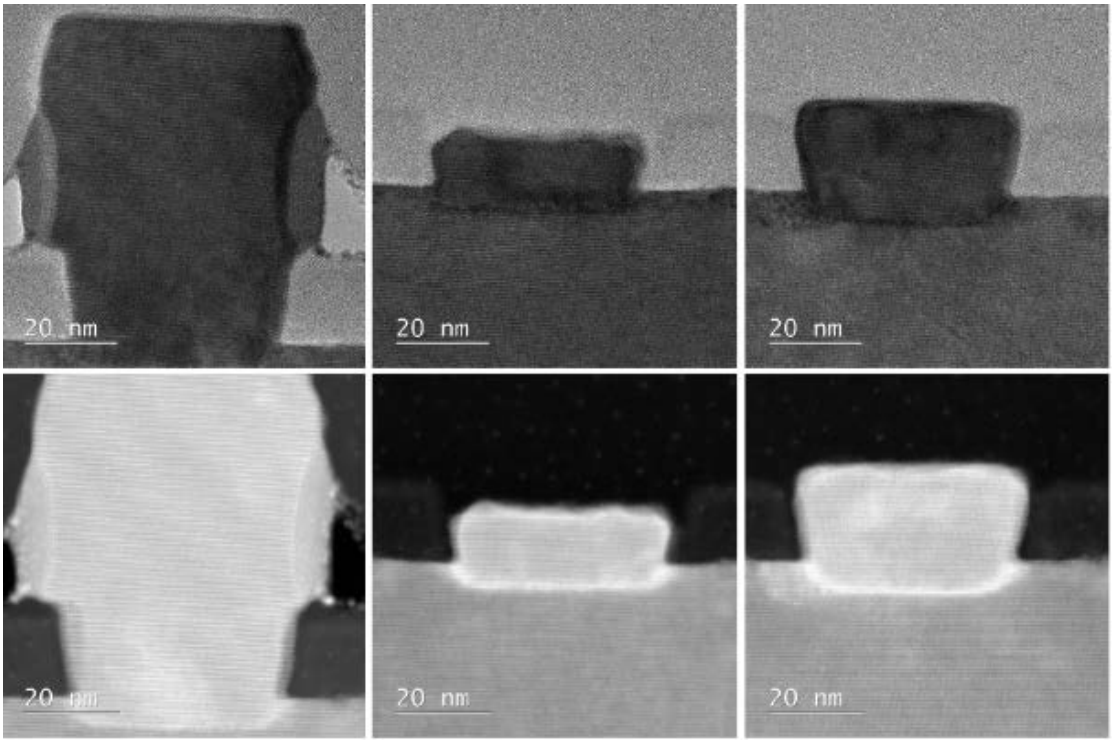


*Figure 56: BFTEM and HAADF-STEM images of the three wires. The images were taken with a magnification of 250 000x.*

The tallest structure on the left shows some less dark grey areas right next to the InSb structure. The EDX mapping suggests that there is still Antimony present here. It could be amorphous InSb. The reason is unknown. A possible explanation could be a high flow across the surface. Giving rise to a continuous pressure against the sidewalls,

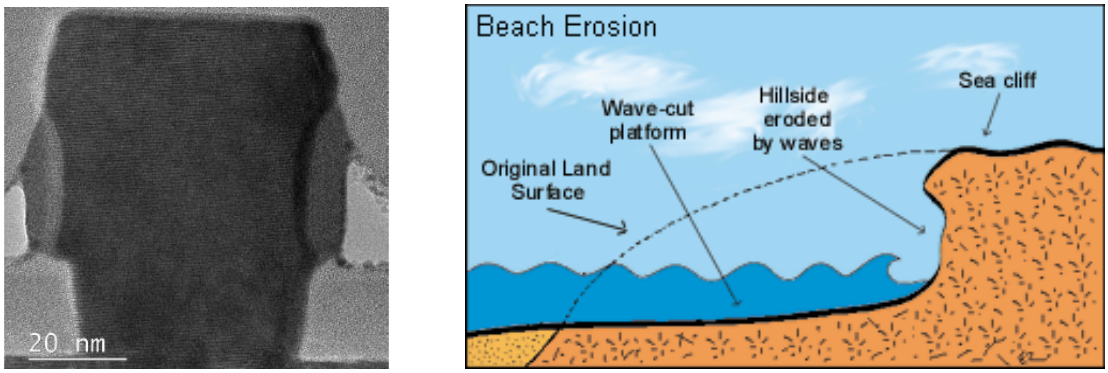


*Figure 57: Left image showing the amorphous InSb ( the less dark grey areas on the sides of the InSb structure). A possible explanation can be found on the right. A continuous pressure due to the flow over the surface could result in the InSb not being able to fully relax crystalline.*

making it impossible for the InSb to relax in a crystalline matter. For better visualisation it could be compared with the erosion of a beach as shown in figure 69 on the right side.[40] It could also be caused during cool down under an Antimony flow, here the lowest energy facets seem not to have formed yet.

The amorphous InSb is also present on the top of the smallest structure, the other two have a flat (111) facet, parallel to the (111) substrate. This could also be caused during cooldown.

Next the Fast Fourier Transformation (FFT) is used to check the epitaxial relation between wire and substrate for the tallest nanowire. The result is shown in figure 70. The first image is the entire structure, where the red square takes the FFT of the full image, the green area is the FFT of the InSb structure, the blue area is the FFT of the interface between InSb and InP and the purple image is the FFT of the InP. The FFT image of the full image shows double spots. This is due to the different lattice constant of InSb and InP. It suggests full relaxation in the lateral and vertical direction as the double spots are visible without lines. The green and purple area show single spot patterns. The blue area of the interface shows double spots again, this time suggesting lateral relaxation at the interface. Vertical lines are still present.

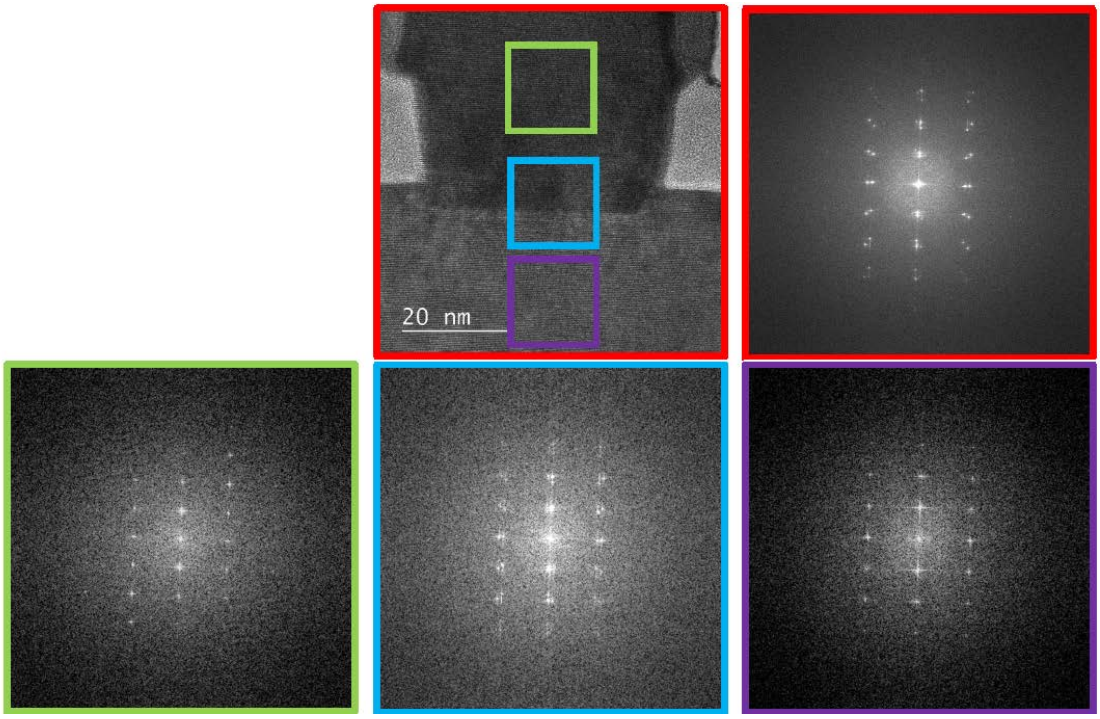


*Figure 58: FFT images of the TEM image at different locations. Red is the full image, double spots suggesting full relaxation in both directions, green and purple show single spot patterns from the InSb and InP. Blue is the region at the interface, suggesting lateral relaxation.*

At last, HAADF-HRTEM has been used to check the misfit dislocation at the interface between InSb and InP. Figure 71 shows the HAADF-HRTEM image with in red the region of interest. When zooming in on this region, the atoms become visible with the crystal structure and planes. At the bottom a special area of interest is marked, where a misfit dislocation is present. This is better visible in the Fourier filtered image on the bottom right image. The lattice planes of InP go over into the lattice planes of the InSb. But since InSb has a larger lattice constant, at a certain position one plane is

missing as is visible. This is called a misfit dislocation. This is how the InSb is able to relax at the interface.

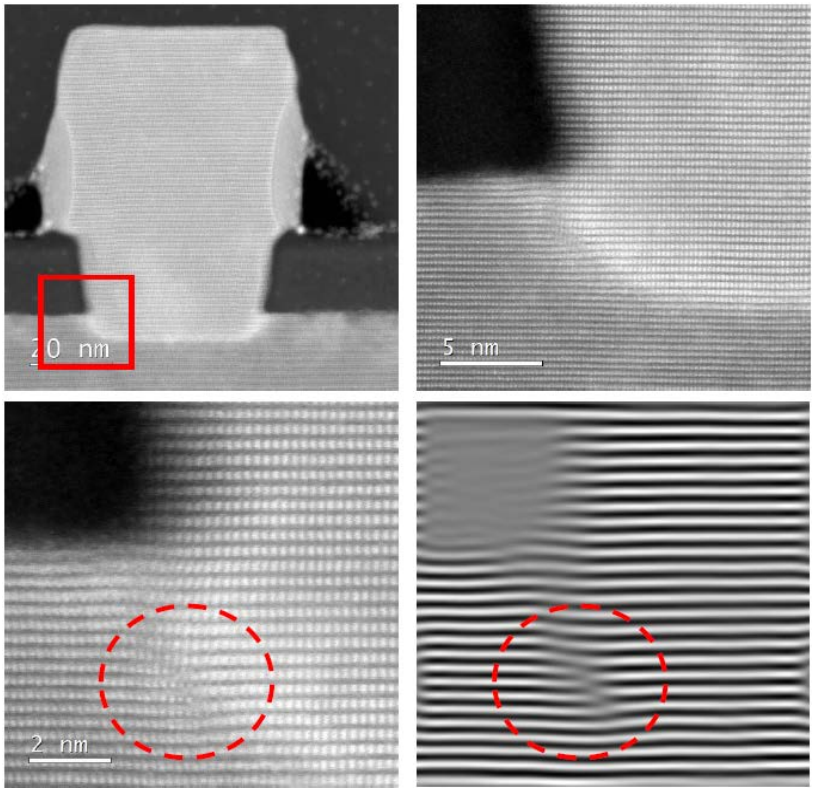


*Figure 71: HAADF-HRTEM image of the tallest structure. Zooming in on the interface, a misfit dislocation is visible. The Fourier filtered image shows the misfit dislocation even better.*

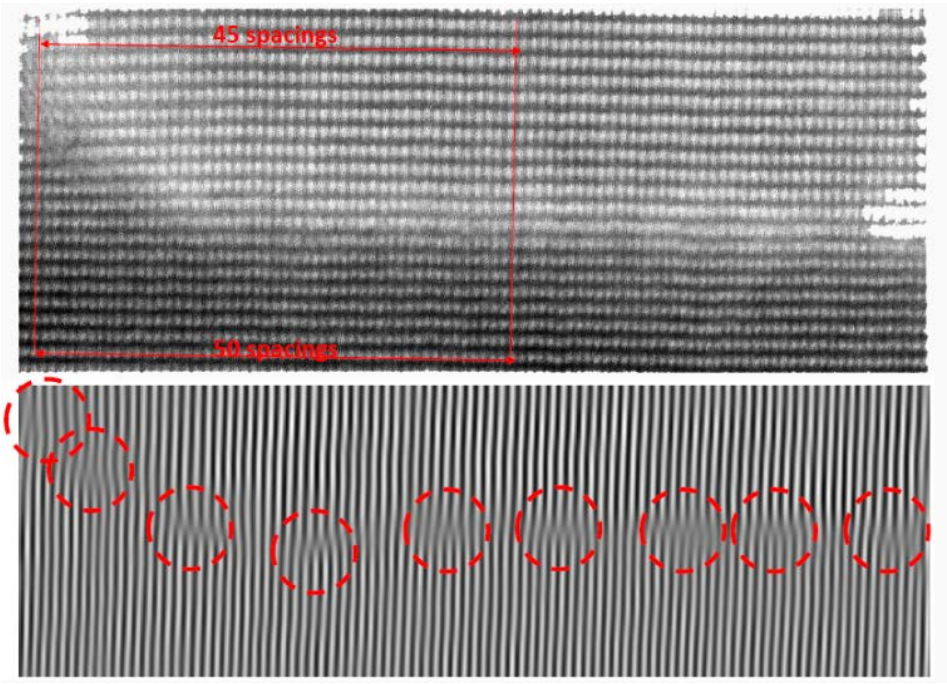


*Figure 72: HAADF-HRTEM image of the interface with more misfit dislocations visible. For every 50 spacings in the InP layer, there are 45 spacings in the InSb layer. This results in one misfit every 10 planes, or 10%. This is the same as the lattice mismatch between the InP and InSb of 10.4%. A Fourier filtered image shows the misfit disloctions more clearly. Again a misfit can be found for every 10 InP planes.*

At last a bigger interface area was used to investigate the number of dislocations at the interface. Again a HAADF-HRTEM image was made. After that a Fourier filtered image was made to see the misfit dislocations more clearly. These images are shown in figure 71 and 72. The HAADF-HRTEM image already shows a different amount of spacings on the same length. For every 50 spacings in the InP substrate, there are around 45 spacings in the InSb layer. So every 50 spacings 5 spacings are missing in the InSb, this is 10%. It is in good agreement with the lattice mismatch between the InP and InSb, which is 10.4%. The same result can be found by looking at the Fourier filtered image. Again 1 plane is missing every ~10 planes, which also gives 10%.

#### 4.3.2.2 TEM on (112) along the wire

Other TEM analysis on wires in the (112) direction, along the wire now, was done on a hashtag like design, with the structure shown in figure 73. Different locations on the hashtag were analysed by looking at the structure at different angles. The four locations are A, B, C and D. A is a thick nanowire, at a certain point this thick nanowire makes a transition towards a thin nanowire, this is location B. Location C is empty and location D manifests a flake. The red rectangle indicates the area from which the filament was made.

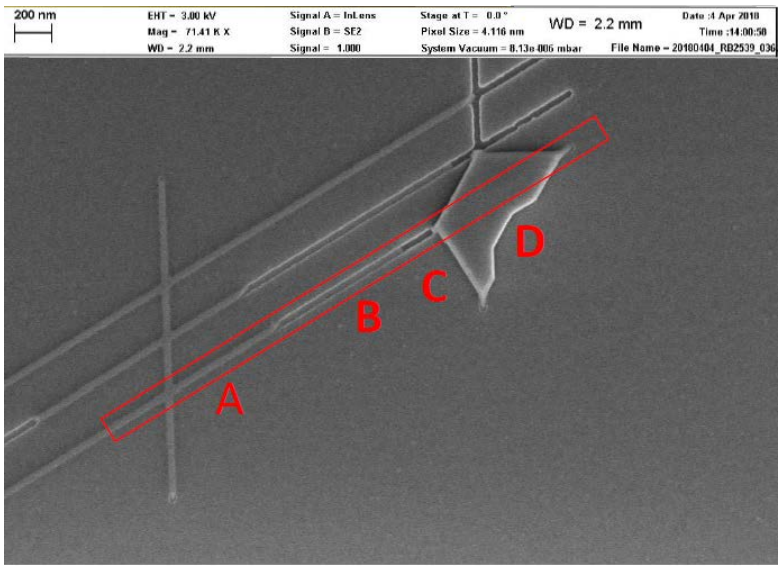


*Figure 73: SEM image of the hashtag structure that was used for the TEM analysis along the (112) orientation. 4 Locations are assigned a different letter. A is a thick nanowire, B is a thin nanowire, C is empty and D is a flake.*

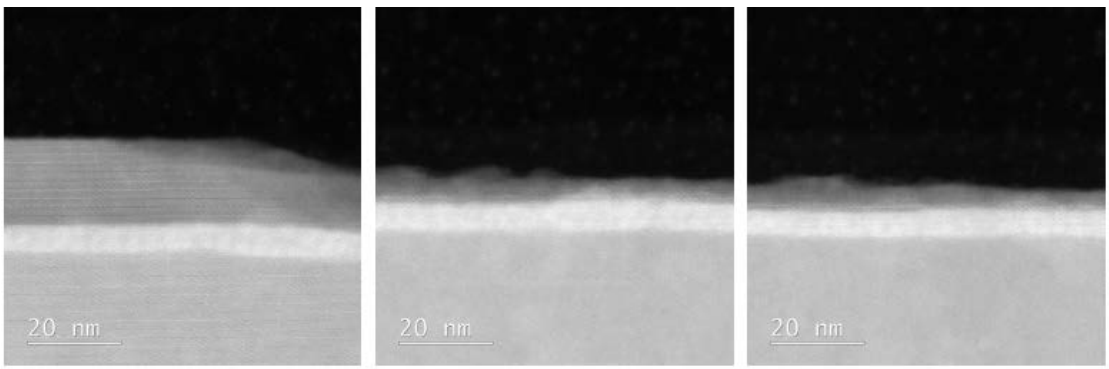


*Figure 74: HAADF-STEM images of the transition between area A and B. The thick nanowire has a smooth top facet while the thin nanowire has an amorphous rough top.*

First the transition between location A and B is analysed. Figure 74 shows three HAADF-STEM images. The first is from the thick nanowire, a clean top facet is visible. The second and third image show the thin nanowire. Observe the rough, amorphous top of this area. Again highlighting that we should focus on the thick nanowires.

Next an image is shown of the transition between area B and C. C is a part of the trench that is empty. On the left the bottom part of the image is InP, the bright part is the interface between InP and InSb with defects, the top part is thin InSb nanowire. At the location where the thin nanowire stops the bare InP substrate is a few nanometre lower. It is not clear if this happened before the growth and that this is the reason why the thin nanowire stopped there, or that this happened during growth because the InP substrate was not covered. If this InP substrate is not covered the Phosphor could evaporate out of the substrate due to the growth temperature. This could damage the surface.

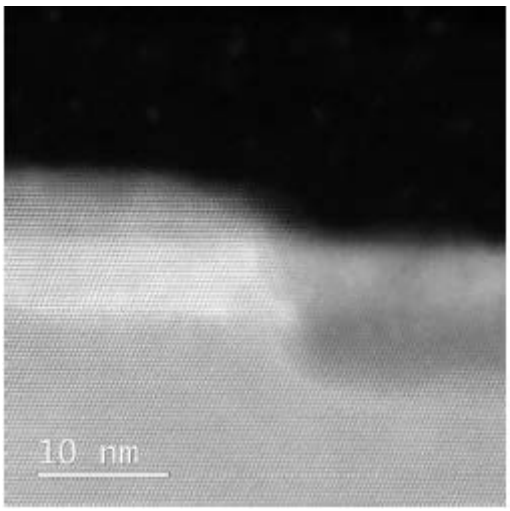


*Figure 59: HAADF-STEM image of the transition between area A and B. The left part is the thin nanowire and the right part is the bare InP substrate. The bare InP substrate seems to been damaged.*

Next an HAADF-HRTEM image is shown of the thin nanowire. A lot of local stacking faults seem to be present by looking at this image. This is again a reason to avoid the thin nanowires.

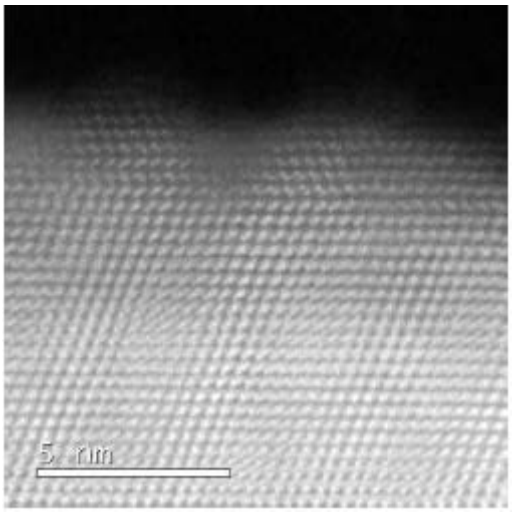


*Figure 60: HAADF-HRTEM image of the thin nanowire. A lot of local stacking faults are visible*

At last a BFTEM image is shown of area D, the flake. This part could be interesting for the flake project. The thin dark stripe in the middle of the image is the interface between the InP substrate and the InSb nanowire/flake. The dark top part of this InSb structure is where the flake is growing over the SiN mask. Three inclined stacking faults are visible here, pointed out by the yellow arrows. These stacking faults already start at the interface. This shows that not all stacking faults seem to be parallel to the surface. These inclined stacking faults are only found in the flake area, if these two phenomena are related is hard to tell.

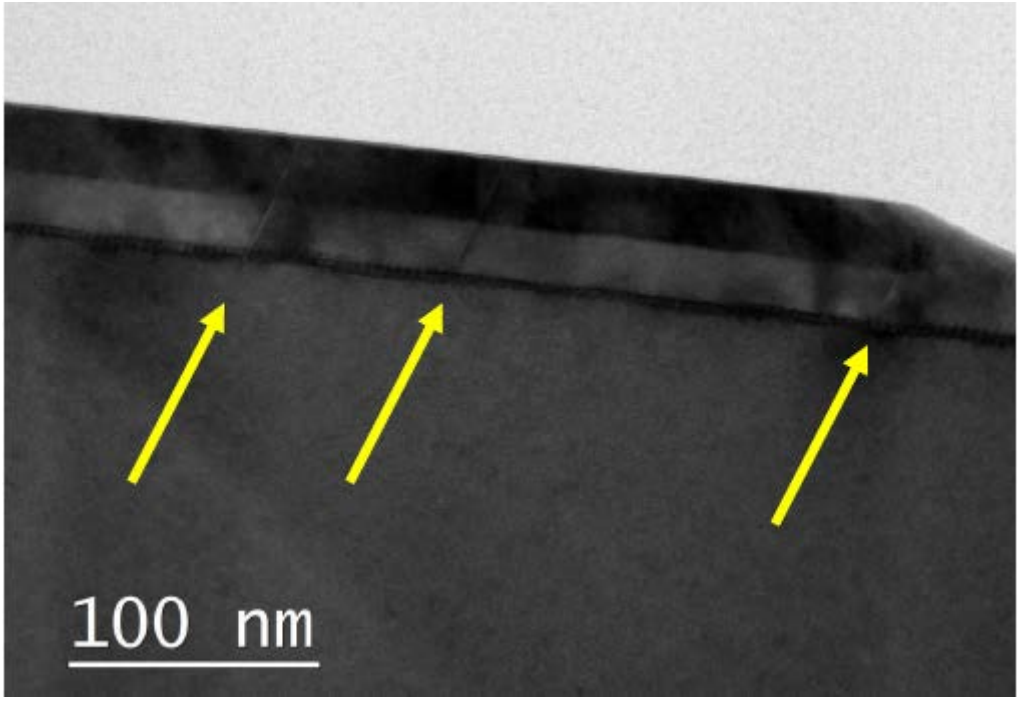


*Figure 61: BFTEM image of area D, the flake. The yellow arrows indicate where the inclined stackings faults are. If these are related to the flake forming is not clear.*

#### 4.3.2.3 TEM on (110) cross-section

The same analysis as with the (112) direction cross-section has been done with the (110) cross-section. Figure 78 shows a SEM image of the structures that have been used, with the red rectangle the place where the filament was cut out.


*Figure 62: SEM image of the three nanowires which were used for cross section analysis in the (110) direction. The red rectangle shows the area from which the filament was made.*

Again BFTEM and HAADF-STEM images were made from the three wires. This time again the thinnest nanowires show an amorphous top (B,C), while the thick nanowire has a clear (111) top facet. The images are shown the figure below and were made with a 250.000 X magnification.

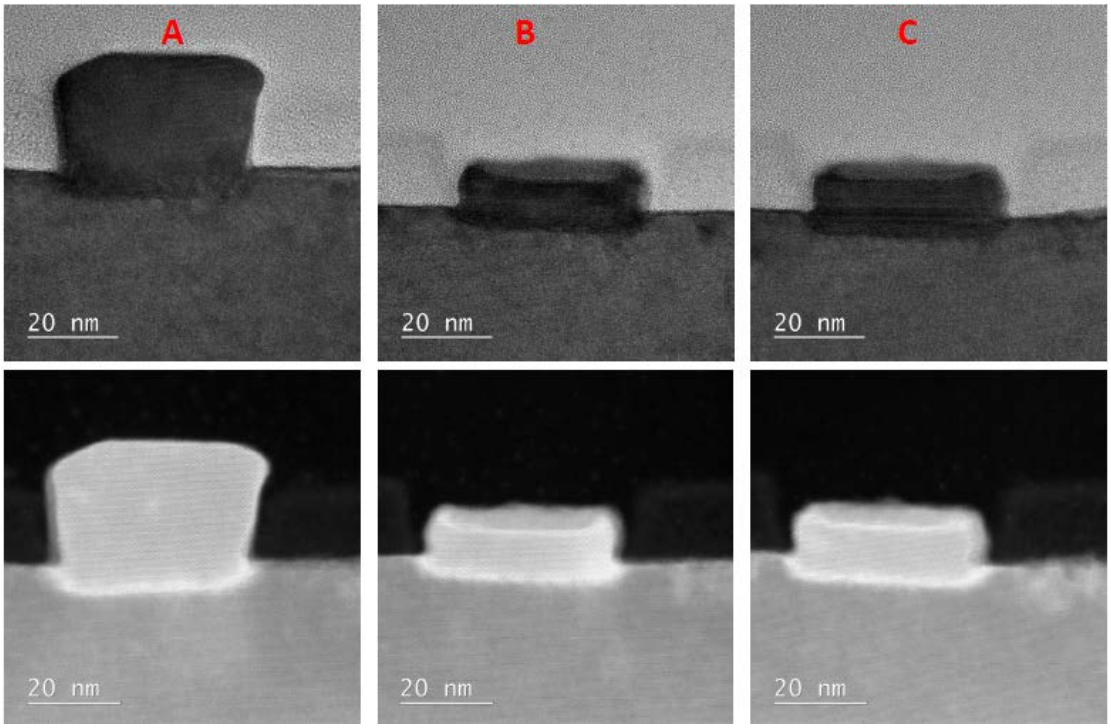


*Figure 63: BFTEM and HAADF-STEM images from the three wires in the (110) direction. Again the thinnest wires show an amorphous top. A magnification of 250.000 X has been used.*

An enlarged HAADF-STEM image, shown in figure 80, from a thin nanowire clearly shows the amorphous top and local stacking faults. The total picture is comprised of two HAADF-STEM images.

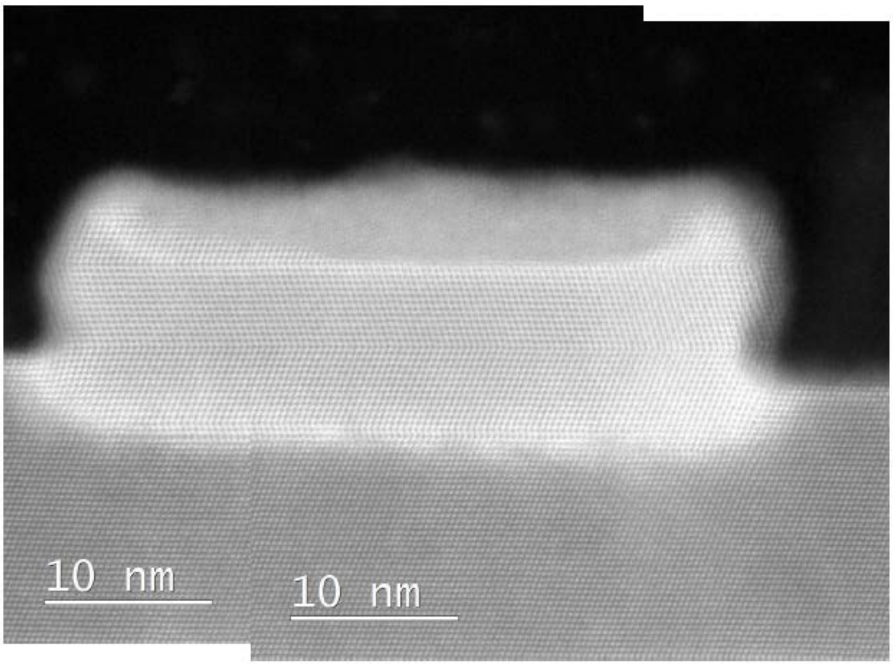


*Figure 64: Picture comprised of two HAADF-STEM images of a thin nanowire in the (110) direction. An amorphous top and local stacking faults are visible*

At last, a HAADF-STEM image is shown of the interface between the InSb and InP for the thickest nanowire. Local stacking faults are highlighted in red and some misfit dislocations are present. Above the interface the InSb seems completely relaxed and crystalline. This is a good sign for the hybrid semiconductor-superconductor devices.

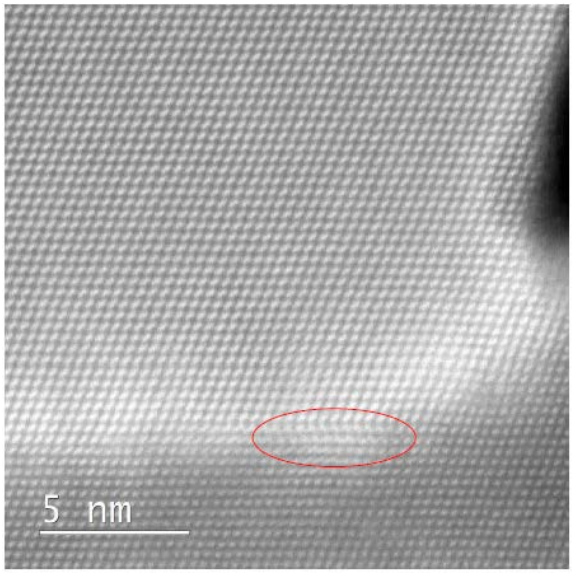


*Figure 65: HAADF-STEM image of the interface between InP and InSb for the thickest nanowire. Some local stacking faults are highlighted in red.*

#### 4.3.2.4 TEM on (110) along the wire

The same analysis along the wire from the (112) direction has been performed on the (110) oriented wires. Figure 82 shows the design used for the TEM, with the red rectangle indicating the area where the filament was made off. Different viewing angles can be used again, this time the (110) direction in yellow is the most convenient.

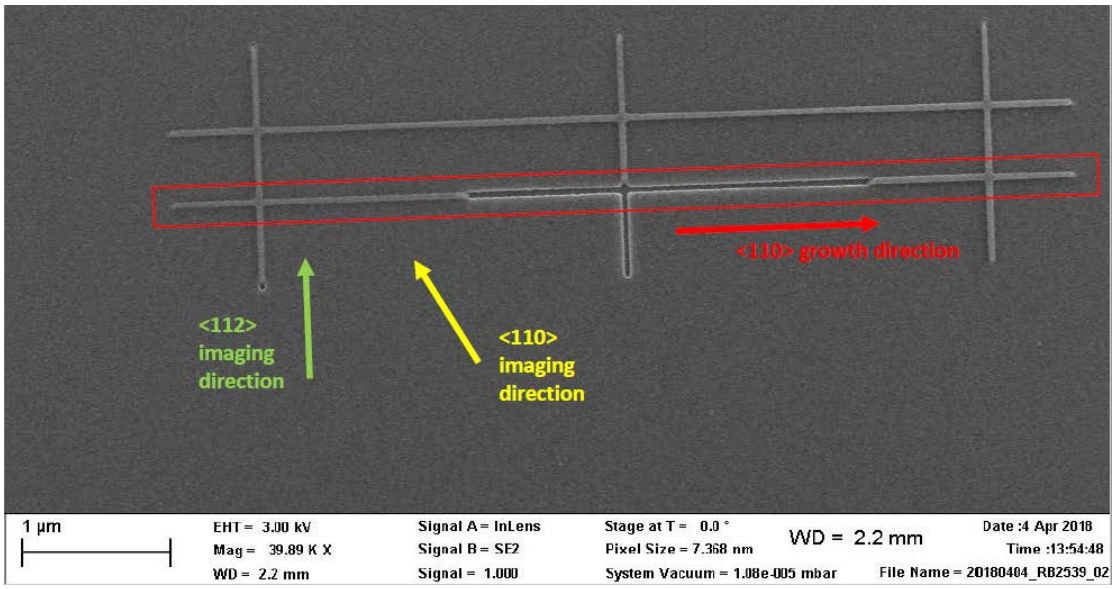


*Figure 66: SEM image of the structure used for TEM analysis on the (110) direction. The red rectangle indicates the investigated area.*

Again the BFTEM and HAADF-STEM mode were used. First the left end was imaged with BFTEM, shown in figure 83. The side facet is not smooth, this could be

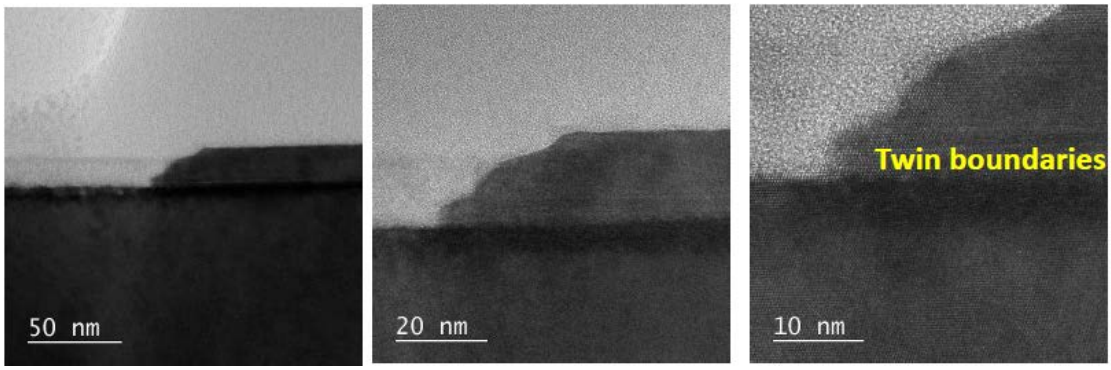


*Figure 67: BFTEM of the left end of the nanowire. The side facet is not smooth, this could be because it is at the end of a trench. Twin boundaries seem to occur a few nanometre above the interface.*

because it's the end of the trench. In this direction twin boundaries happen a few nanometre above the interface, the same thing has been observed in the (112) direction.

Next HAADF-STEM was used to look at the twin boundaries with more details. The twin boundaries are clearly visible in figure 84 on the right side as a kink in the growth direction upwards. Both images were made while looking from the (110) direction (yellow). This twin boundary could be a seperation between the crystalline InSb on top, used for the device, and the interface with misfit dislocations.

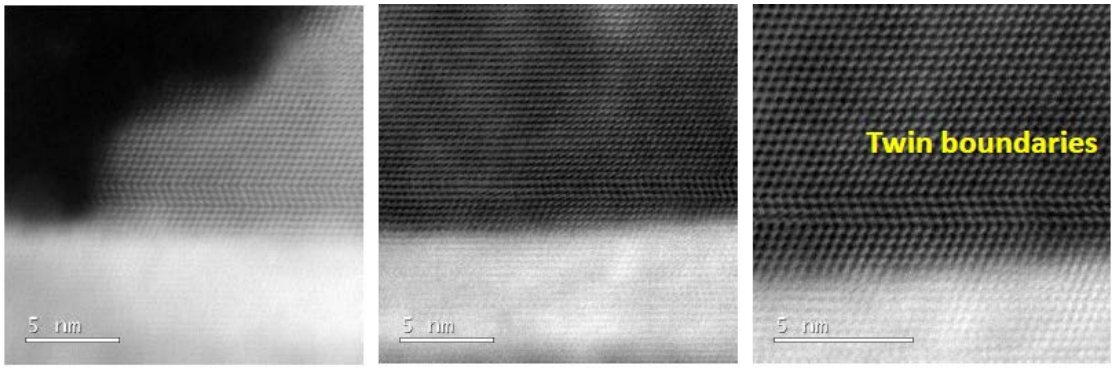


*Figure 69: HAADF-STEM image of the same place. Where the twin boundaries are clearly visible on the right side.*

The same analysis was performed on the left edge of the second nucleation. Here the side facet looks smoother, this side facet is not a the end of a trench. Figure 85 are BFTEM images showing the side facet and the interface with the InP substrate.

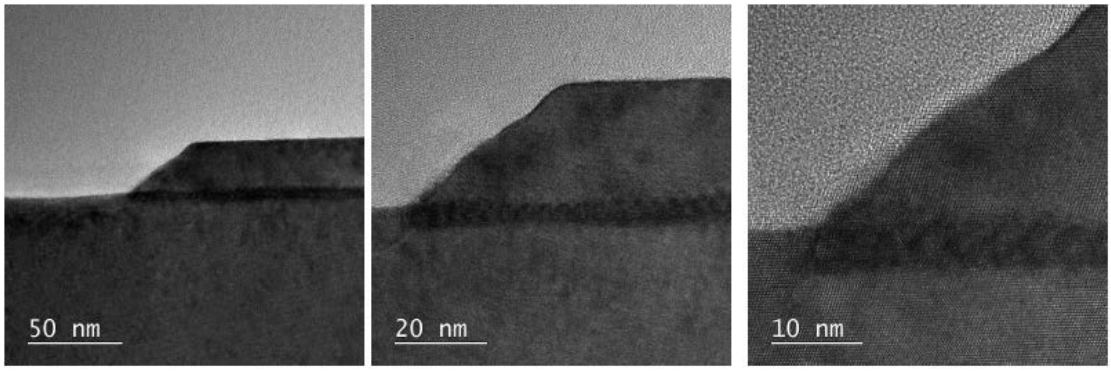


*Figure 68: BFTEM images of the second nucleation. Again the left side facet is shown. This side facet is not at the end of a trench and seems smoother.*

The HAADF-STEM image of the same side facet shown in figure 86 shows that this time there is no twin defect present. If this has influence on the performance of the device is not clear.

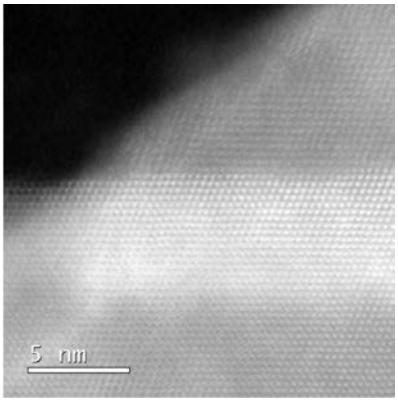


*Figure 70: HAADF-STEM image of the second nucleation in the (110) direction. The left side facet shows no signs of a twin defect this time.*

## 4.4 Coherence length in hashtag grown with optimal conditions

The Aharonov-Bohm effect is used to study the quality of the devices. An interference measurement is performed were out-of-plane magnetic field results in a phase shift due to the Aharonov-Bohm effect. Figure 87 shows a SEM image of the device. Two opposing corners of a loop are contacted with gold. The electrons go from one contact to the other. This could happen by travelling half the length of the structure. But some electrons first make a full loop or multiple loops before reaching the other contact as described in chapter 2.6.

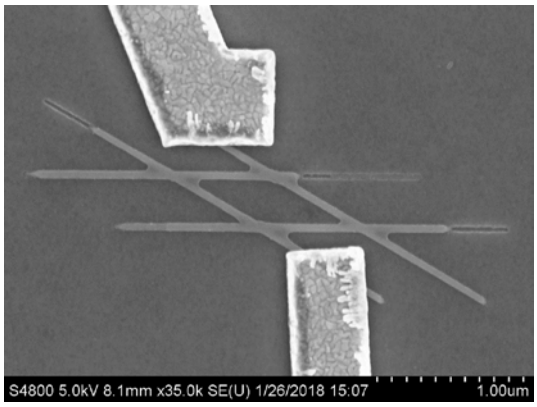


*Figure 71 SEM image of the structures, in this case a hashtag loop, contacted with gold. The electrons travel from one contact to the other.*

The fast Fourier transformation (FFT) of 11 measurements were taken and averaged as shown below. Up to 5 harmonics (peaks) are visible in the signal, relating to 5 full loops before exiting as described in chapter 2.6. In the logarithmic scale even the 6$^{th}$ harmonic is visible with a little bit of imagination. These higher harmonics correspond with a larger phase-coherence length of the electrons in the structure, an indication that the InSb grown while using the found optimal conditions can be used in hybrid semiconductor-superconductor devices.

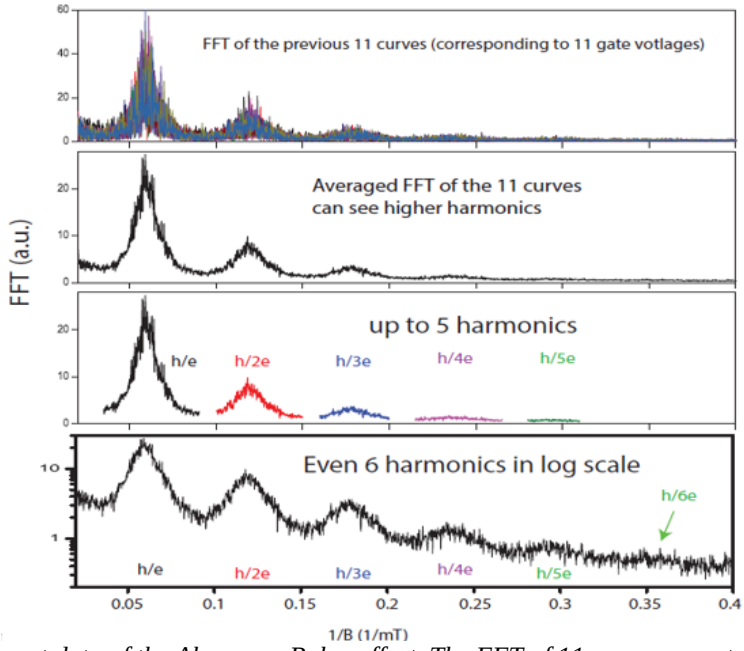


*Figure 72: Transport data of the Aharonov-Bohm effect. The FFT of 11 measurements were averaged. Up to 5 harmonics are visible, in the logarithmic scale even 6. This corresponds with a large coherence length.*

The $5^{th}$ harmonic relates to the electrons travelling 4 ½ loop before exiting. The loop has four sides of 1000 nm. This results in a phase-coherence length of the electrons of up to 18 μm. This is a strong indication that InSb directly grown on InP can be used for the hybrid semiconductor-superconductor devices, despite the large lattice mismatch. A buffer layer to accommodate for this large lattice mismatch is not required.

For this measurement a hashtag design has been used. The specially made Aharonov-Bohm designs without the unused side arms the hashtag has could even improve the data. This could be done in the near future.

## 4.5 Selective area overgrowth in-plane flakes

Selective area overgrowth has been used to create 2D sheets of InSb. The designs from chapter 3.3.3 were used, specially made to increase the total size of the sheets. Choosing directions in between the (112) and (110) directions will result in relaxation by making facets in these directions. This is clearly visible in the left image of figure 89. The growth of the in-plane InSb flake stops after reaching these lowest energy facets. Being able to still see the design underneath would imply a very thin layer of InSb. A thicker InSb flake is shown on the right side. An interesting observation is the 'hovering' of the InSb over the SiN mask as it does not want to bond. Increasing the growth window and changing the V/III ratio influences the growth and thickness of the flakes. The thin flakes as shown on the left side are probably more interesting for applications due to the restrictions to two dimensions.

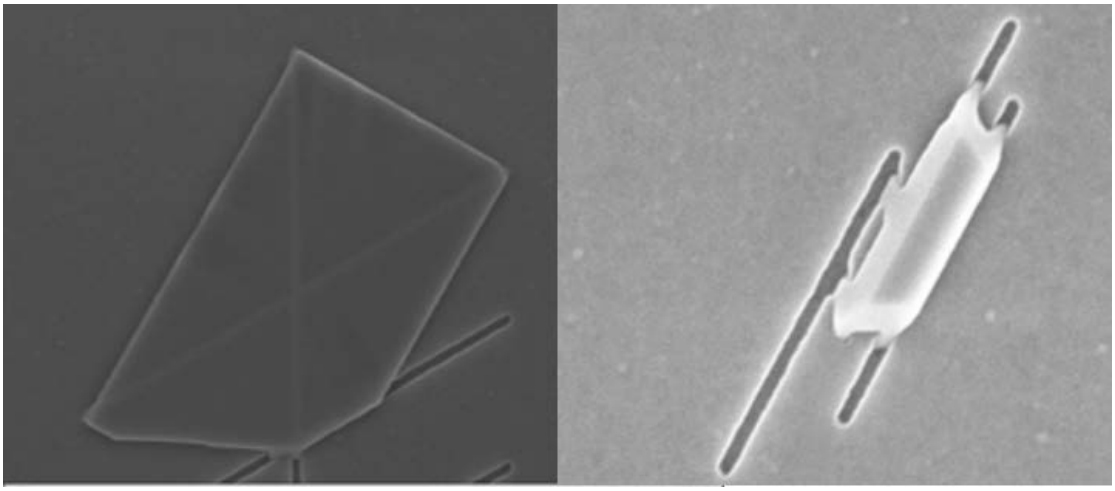

*Figure 73: Left:SEM image of a big flake on a hashtag like design. The clean edges show the facets. Being able to still spot the design underneath would imply a very thin layer of InSb. Right: SEM image of a thicker flake hovering over the SiN mask.*

The size of the flakes and yield is still not as big/high as they possibly could get. Further research could improve the results, this is discussed in chapter 6.6. Thermal annealing before growth could already improve the yield significantly, as could other V/III ratios. The special designs could increase the maximum flake area before the

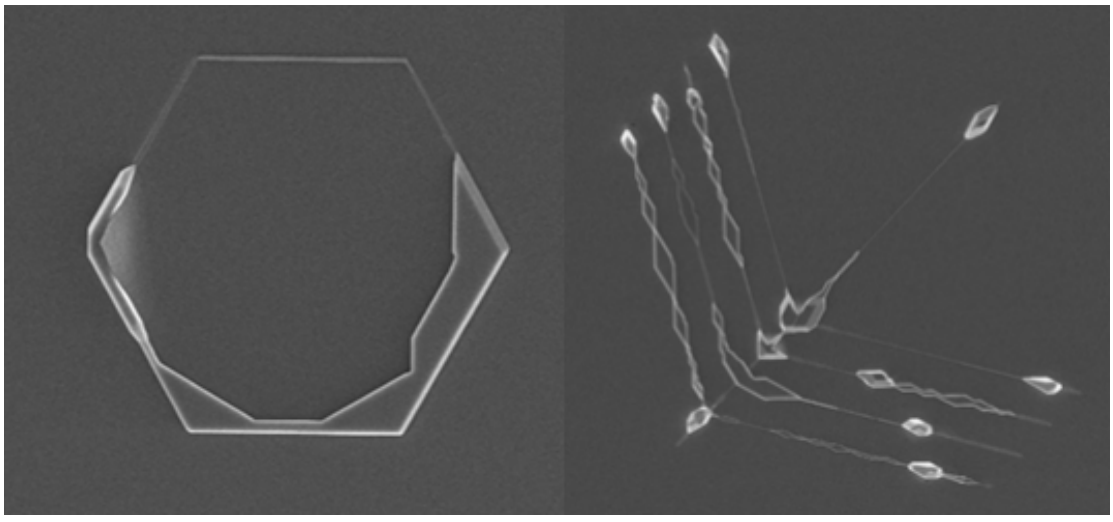

*Figure 74: SEM images of a hexagon and leaf design after selective area overgrowth with InSb. Faceting happens in the preferential growth directions.*

lowest energy facets are formed. The results without thermal annealing are shown in figure 90. The numerous of small flakes and bigger ‘blobs’ are likely a result of the oxidized InP substrate.

The best conditions for the InSANe project were found using a flow of 12.5 sccm for TMI and 37.5 sccm for TMSb. When increasing the TMI flow and decreasing the TMSb flow, there are in general more flakes. By trial and error the best parameters for flakes were found to be 35 sccm of TMI and 8 sccm of TMSb. This results in an effective V/III ratio of 73.4. This is considerably lower than the effective V/III ratio of 962.9 for the InSANe project. If these parameters will again give the best results when performing thermal annealing is not known.

## 4.6 Thermal annealing

Thermal annealing has been performed in situ to get rid of the native oxides on the surface. The native oxides passivate the surface and change the surface adhesive force and layer chemical potential, as described in chapter 2.4.1. The ratio between the adatom cohesive force and the surface adhesive force determines the growth mechanism. As the island formation caused by a higher adatom cohesive force is unwantingly decreasing the yield, a higher surface adhesive force by annealing could solve the problem.

Getting rid of the native oxides with thermal annealing can be achieved in different ways. The problem is the evaporation of Phosphor at this temperature, decomposing the surface. Therefore the thermal annealing has been performed under Phosphine pressure in the chamber, this limits the Phosphor evaporation. With this method it is possible thermal anneal at temperatures higher than 600°C. This will ensure that the surface is depassivated. The downside is that the Phosphor in the room will contaminate the growth of the InSb nanowires afterwards. Instead of InSb we would get $InSb_xP_{1-x}$. The solution is to separately grow and thermal anneal in different reactors. The thermal annealing has been performed by heating up under 306.25 sccm of $PH_3$. After heating till the temperature exceeds 780°C, the chamber is stabilized for 5 minutes at 750°C. In the next 5 minutes the $PH_3$ value is dropped to 80 sccm, after which the system is kept at these conditions for 5 more minutes before cooldown. After cooldown the sample is moved to the other chamber for the growth. Some of the results are shown in figure 91.

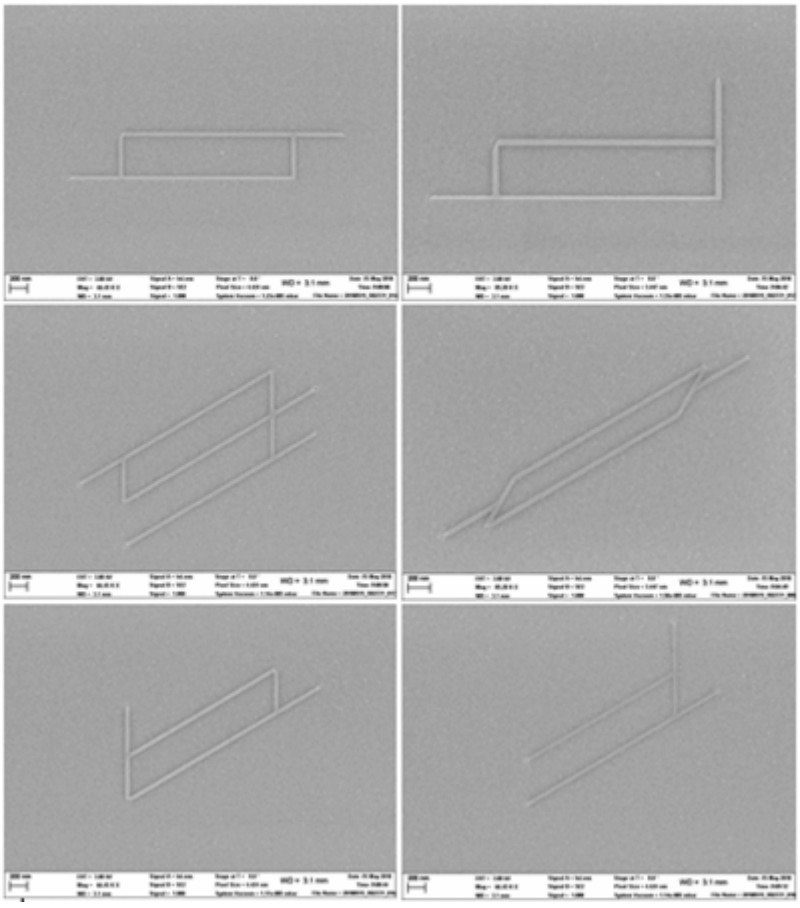

*Figure 75: SEM images of some InSb structures with a thermal annealing step. Al kind of shapes and both the (110) and (112) direction seem to grow very well.*

Every design is now grown well, there is no flake or blob forming. This results in a yield of >95%. Comparing this to the results before thermal anealing, as described in chapter 4.1, shows that the native oxides really were the limiting factor. Before the extra thermal annealing step, the yield was around ~60%, where a lot of structures had multiple nucleations or blob forming. A good recipe for growing InSb on top of InP(111)B with high yield has now been found. With a TMI molar fraction of 3.49E-07, a TMSb molar fraction of 1.49E-03, a surface temperature of ~425°C and a growth time of 40 minutes. The effective V/III ratio is 962.9.

Some high resolution SEM images were made under a 30° angle instead of a typical top view, they are shown in figure 92. The images clearly show the difference in height of the nucleation. The one qubit design is filled with InSb which is thinner than the ~20nm SiN mask. The hashtag like design has an InSb network which is thicker than the SiN mask. This design is not completely filled yet but this could easily be accomplished by increasing the growth window. As told before, the end goal is to make a hybrid semiconductor-superconductor device. This superconducting material should have a clean contact/interface with the InSb, which is easier to accomplish with an InSb which is thicker than the SiN mask. Therefore this research aims at thicknesses of the second kind. Moreover the thicker wire has more crystalline InSb material away from the interface and defects, this could possibly increase the electrical properties.

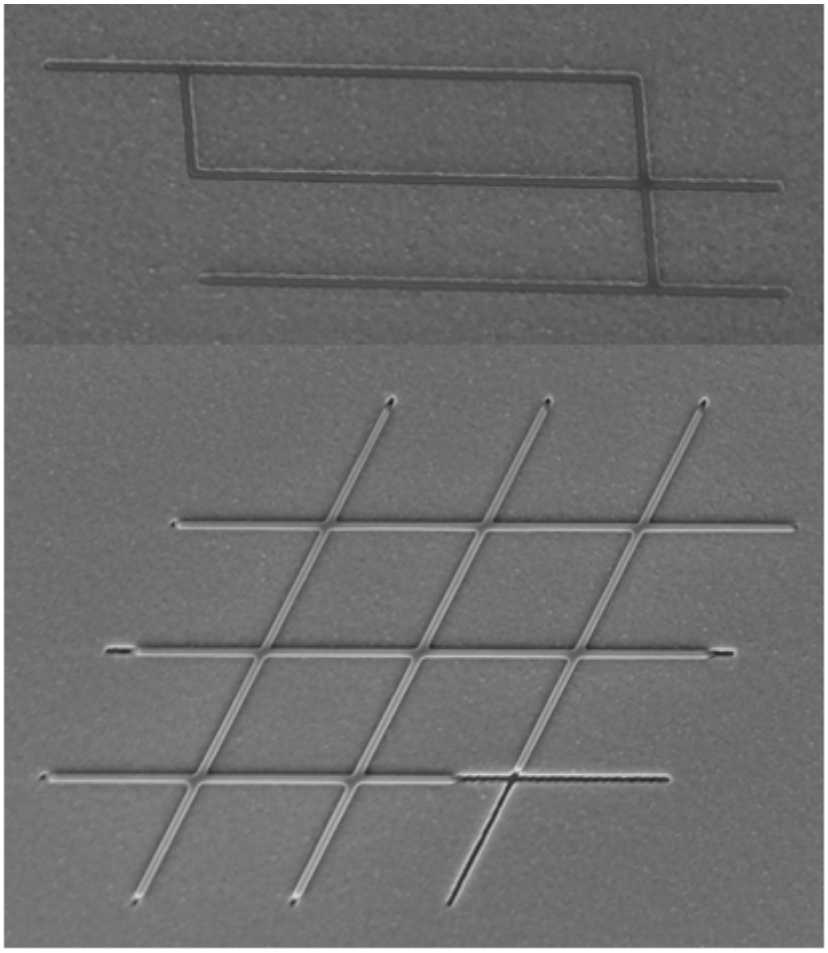

*Figure 76: SEM images of a sample with thermal annealing procedure. The images were taken under a 30 degree angle. Clear difference in thickness of the InSb network can be observed*

Switching from reactors for the thermal annealing step is troublesome and there could be a way to perform it without Phosphine pressure according to literature. This is described in chapter 6.7. Increasing the yield was the last hurdle before adjusting the structures to bigger and more complex designs. A few of these designs have already been made. The first results are shown in the next chapter.

## 4.7 Growth of complex structures realised

After a yield of ~95% was realised, more complex designs were made as described in chapter 3.3.5 to show the feasibility. Due to limited availability of the thermal annealing reactor, these structures were not yet grown while using this thermal annealing step. This results in a lower yield. Figure 93 shows the overview of the new designs.

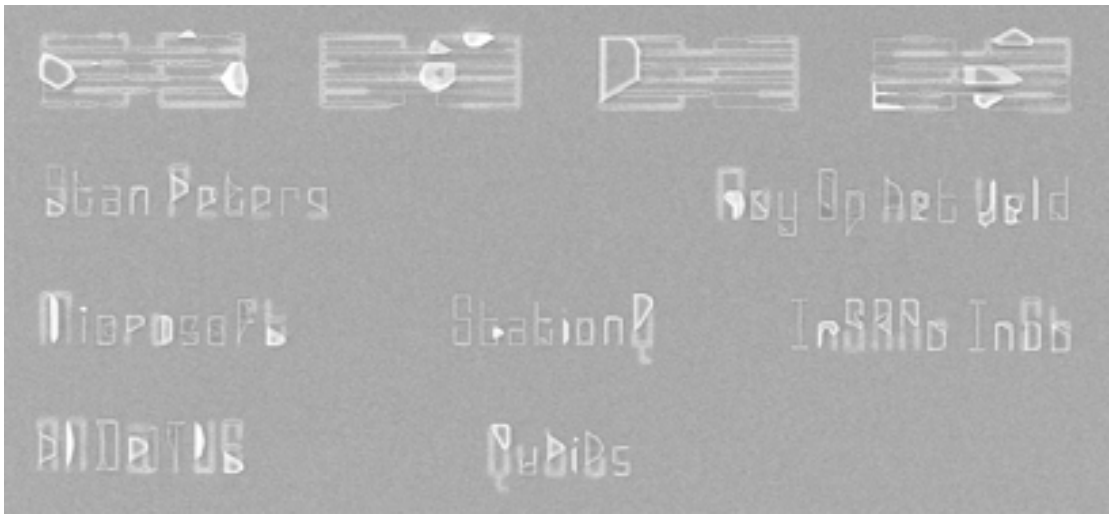

*Figure 77: SEM image of an overview of the complex designs. On top the 4 qubit design is repeated and on the bottom different names and phrases are present.*

On top the design for the 4 qubit devices is repeated 4 times. On the bottom several words and phrases are shown. A lot of flake forming is happening, probably because the thermal annealing step was not performed. Zoomed in SEM images of the words are shown in the next figure 94.

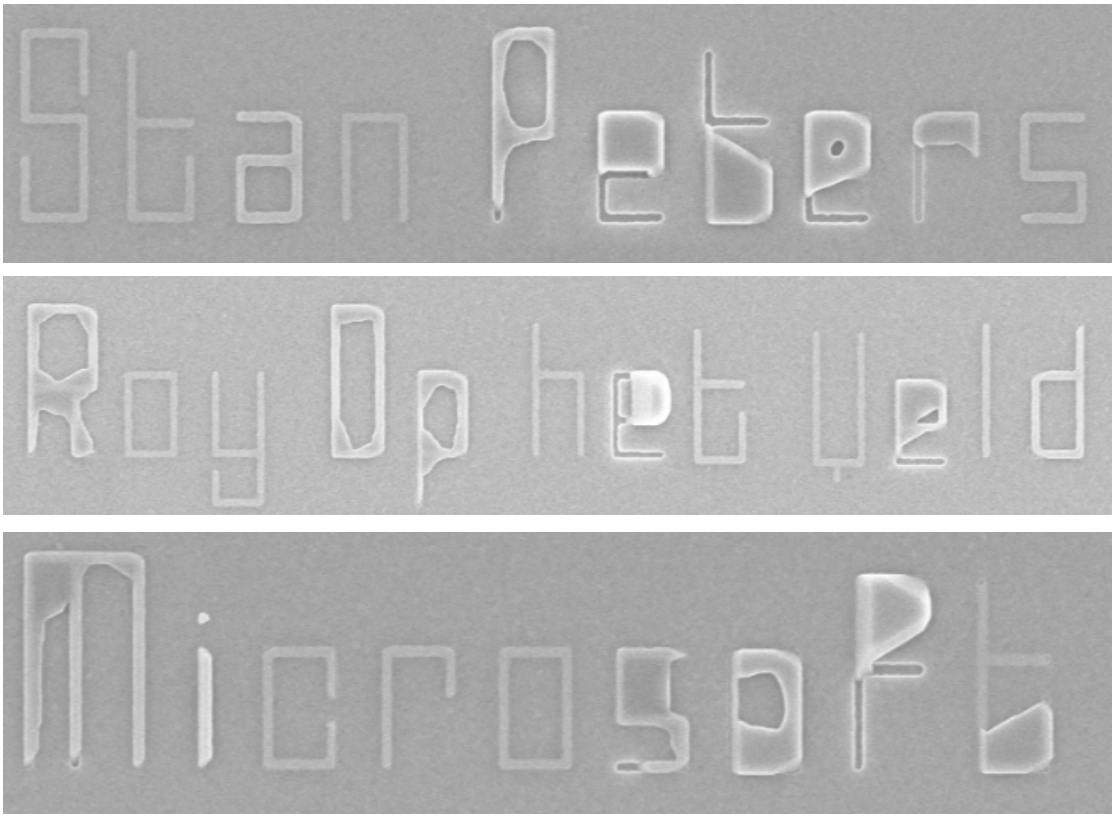

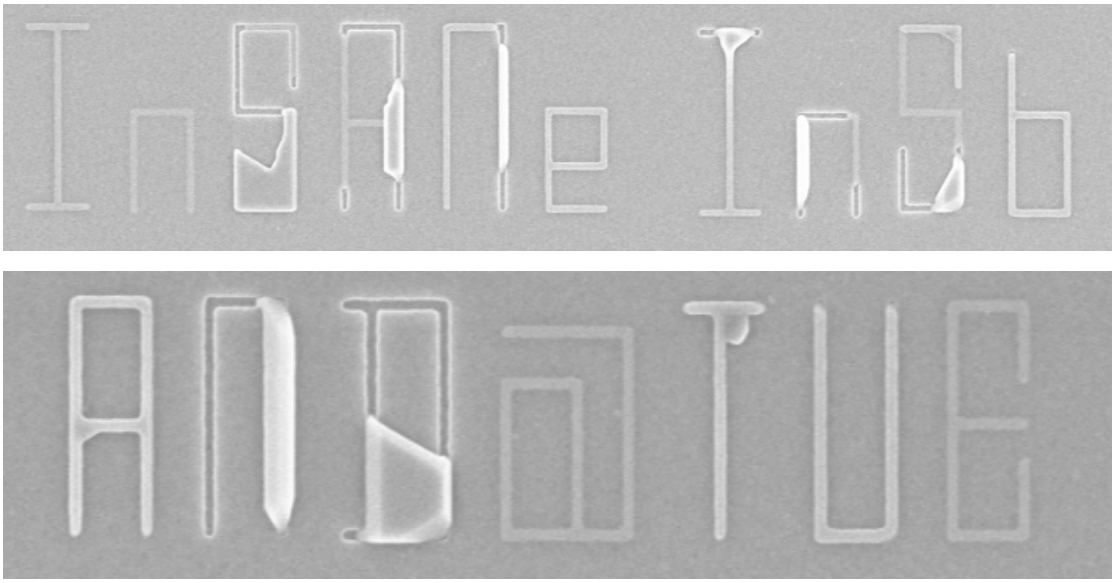

*Figure 78: SEM images of the words and phrases. Special square font makes sure that only (110) and (112) directions are used.*

Some letters/symbols are grown perfectly. The same yield is achieved as with the networks without thermal annealing. An indication that with the thermal annealing step most of them will grow well. This illustrates the possible full control over the growth of in-plane InSb networks directly on an InP substrate. When the thermal annealing reactor is available again better results could be achieved.

# 5 Conclusion

The use of a hybrid semiconductor-superconductor device to host a Majorana fermion for topological qubit applications is much debated. III-V semiconductor InSb could be used as the semiconductor foundation. Here we demonstrate the feasibility to grow InSb nanowire networks on top of an InP(111)B substrate.

First the growth conditions were varied to find the optimal parameters. The InSb seems to grow well on an InP(111)B substrate grown by MOVPE while having a TMSb precursor molar fraction of 1.49E-3, a TMI precursor molar fraction of 3.49E-7, a temperature of 460°C, a total volume flow of 6000 sccm and a growth window of 30-40 minutes. An interesting observation is the nicely grown structures in the (112) and the (110) crystal orientations across the surface, other orientations don't work. A yield of ~60% was achieved.

An Indium and Antimony series has been performed to investigate the influence of these parameters on the growth. The Indium series shows that the growth is Indium limited, increasing the TMI molar fraction has the same effect as increasing the growth window. High values of the TMI molar fraction result in flake forming. The Antimony series does not show the same kind of correlation. Low values of TMSb molar fraction seem to result in a lot of nucleations.

Next the nucleation mechanism has been studied by limiting the growth window to 1 minute. Again an Indium and Antimony series has been performed. This time the average distance between nucleations (L) has been measured for different molar fractions of TMI and TMSb. For the Indium series L seems to exponentially increase for low values of the TMI molar fraction. As the growth is Indium limited, this could be caused by a shortage of Indium. The Antimony series show an increase in L for high values of the TMSb molar fraction. This time it cannot be explained by a shortage of Indium as this parameter stays the same. The excess of Antimony could passivate the surface, decreasing the places where a nucleation can happen. The nucleations already show several facets, orientations with a lower energy. The top of the nucleations seems to grow parallel to the surface so is a (111) facet. The side facets seem to all be from the (110) family, this is in agreement with literature. [18] For both series the (112) orientation nucleations seem to have a larger L than the (110) orientation nucleations, resulting in less nucleations per micrometre for the (112) direction. The cause is not found.

After the nucleation the growth mechanism has been studied by varying the growth window. The growth seems to be linear in time. By fitting the data a growth speed of 0.73244 micrometre of InSb nanowires per minute was found. The defects in fully grown InSb nanowire networks have been studied with a TEM. The TEM images show that the InSb seems to relax immediately at the interface with help of misfit dislocations. The frequency of the misfit dislocations is around 1 in 10, this is in good agreement with the 10.4% lattice mismatch. The top part of the InSb structures is defect-free. This shows the ability to grow crystalline InSb directly on an InP substrate regardless of the large lattice mismatch. Nanowires thicker than the SiN seem to have a flat (111) surface, while thinner nanowires sometimes have an amorphous region on top. Therefore the focus should be on the thicker nanowires.

Next the phase-coherence length of the electrons has been studied with Aharonov-Bohm measurements. The phase-coherence length of the in-plane InSb nanowire networks is up to 18 micrometre long. This is huge and shows great promise for topological qubit devices made with an InSb semiconductor foundation.

The formation of large in-plane InSb flakes growing on top of the SiN mask has been observed. As a side project different designs have been made to increase the total area of the flake. The flake forms by having a nucleation not aligned with the (110) or (112) orientation. The nucleation wants to relax to the low energy facets and forms a flake. Further research could improve the yield.

To improve the yield of ~60% for the best recipe, thermal annealing has been performed before growth. A native oxide layer, already present after the wafer is exposed to air for a few seconds, is removed by increasing the temperature to 780°C. These native oxides could passivate the InP substrate. This has been done under Phospine pressure to prevent the Phosphor from the InP substrate to evaporate, as the Phosphor evaporation would damage the substrate. After thermal annealing the best recipe has been used again. This resulted in a yield of ~95%. A splendid result which shows that the native oxides were limiting the growth.

# 6 Outlook

For future implementations and devices several aspects could be improved. Taller structures could be made to improve the transport in the devices, this could be achieved by using a 50 nanometre SiN layer instead of 20. This is discussed in chapter 6.1. In the next chapter a method is defined to grow structures as large as possible from one nucleation. When scaling, dealing with multiple nucleations is unavoidable. This means that merging may form a problem due to defects. Studying this merging could be very interesting and is described in chapter 6.2. Another aspect that has to be added for future implementations is a global backgate. There are several restrictions for the global backgate, these are defined in chapter 6.3. One option is to use N-doped InGaAs as a global backgate. The downside is that it does not form a nice thin epitaxial layer when grown on an InP(111)B substrate, instead it forms pyramidal hillocks. It does grow fine on an InP(100) substrate. The possibility to grow the InSb structures on an InP(100) substrate is discussed in chapter 6.4. A problem with the InP(100) substrates is that the defects caused by the lattice mismatch induce defects that are inclined to the surface. A buffer layer almost lattice matched to the InSb could incorporate the defects. The use of an AlInSb buffer layer is discussed in chapter 6.5

Another interesting experiment would be to look at the in-plane flakes. These InSb 2D sheets could have varying applications. Increasing the size of these flakes could be achieved by using the thermal annealing beforehand and growing for a longer time or by varying angles, designs and growth parameters.

The results of the nucleation experiment in this research was achieved without thermal annealing. The effect of thermal annealing was only discovered later on in the experiment, but has the potential to change the nucleation process drastically. New series with thermal annealing could give a better understanding of the nucleation process. This is discussed in chapter 6.7.

## 6.1 50 nm SiN mask for thicker wires

A thicker SiN mask could create more defect free crystalline InSb away from the defects at the interface, this could possibly enhance the electron mobility. Growing for a longer time with a 20nm SiN mask would result in overgrowth instead of taller structures. Therefore it could be interesting to deposit a 50 nanometre SiN mask instead of a 20 nanometre mask. This 50 nanometre SiN mask would need longer RIE exposures to open a trench to the InP substrate underneath. The pure CHF3 exposure now used for the 20 nanometre SiN layer is used for 1 minute and 15 seconds. If the process is linear this would result in a time of 3 minutes and 8 seconds for 50 nanometre. A RIE time of 3 minutes, 3 minutes and 10 seconds and 3 minutes and 20 seconds have been used and demonstrate the non-linear behaviour, shown in figure 95.

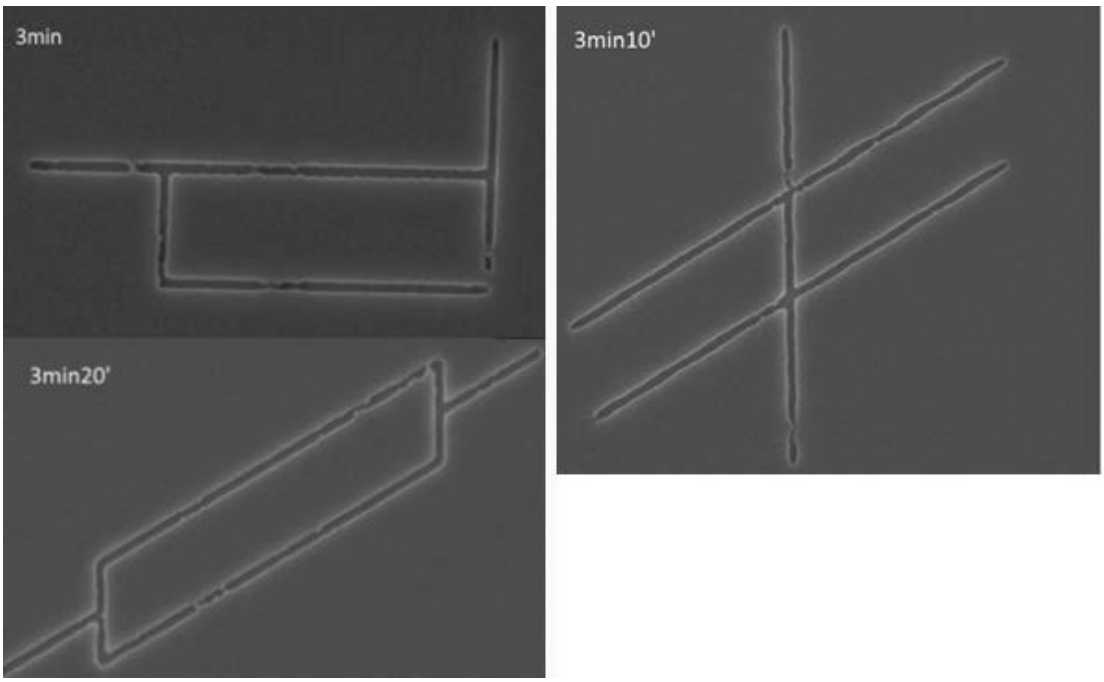


*Figure 79: SEM images showing designs with varying RIE time. The 3 minutes and 8 seconds which would be enough if the process is linear does not seem to be enough.*

All designs are still partly opened. Even the 3 minutes and 20 seconds was not enough. When using a 50 nanometre SiN layer with a pure CHF3 RIE exposure, my suggestion would be a time of 3 minutes and 45 seconds. Due to limited time this was never done.

## 6.2 Study of the merging of multiple nucleations

The growth of bigger designs from a single nucleation will only go so far. At a point multiple nucleations are bound to happen when scaling. These nucleations will have to merge to form one big design. If this merging does not happen correctly it can cause defects and twin boundaries. These twin boundaries could influence the properties of the InSb crystal. A study into this process could be very helpful and informative.

A paper from Gazibegovic et al.[11] shows positive signs. Their InSb hashtags are grown by merging multiple out-of-plane nanowires as shown in figure 96. This can cause twin boundaries at the merging points. Transport data from their research suggests that these defects do not influence the transport in the devices. If it's the same for the in-plane InSb networks is not clear.

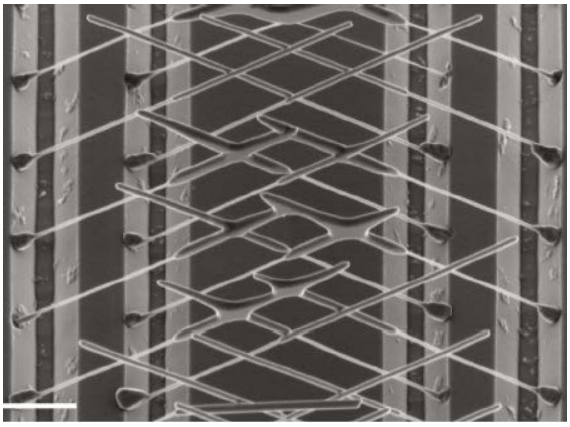

*Figure 80: Out-of-plane InSb nanowires merging mid-air from literature. The merging causes twin defects, which does not seem to affect the electrical properties*

The same thing happens when multiple nucleations merge with in-plane InSb structures. These defects can run inclined to the surface. Figure 97 shows a SEM image with a top view of such a twin boundary on the left side, on the right side a TEM image is shown where the inclined defects are visible from the side, if these are the result of multiple nucleations merging is not proven.

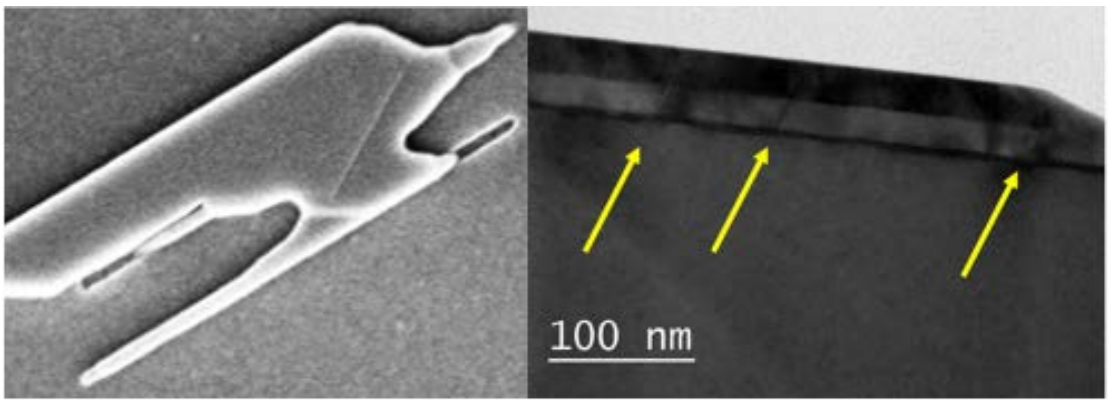


*Figure 81: Left side is a SEM image showing a twin boundary with top view. Right shows multiple twin boundaries from the side. Both could have been caused by nucleations merging.*

## 6.3 Global backgate

For the use as topological superconducting qubits a global backgate should be present for the transport measurements. This is the next step towards a fully functioning Majorana fermion qubit. For the global backgate N-doped InGaAs could be used. A sandwich of InP/N-doped InGaAs/InP could be used as a global backgate while still being able to use the same recipe for the growth. (Because the top layer is again an InP layer). The global backgate layer should have the same lattice parameter as the InP to prevent defects, it should have a low band gap and when doped it should be conducting like metals. So first a thin epitaxial layer of lattice matched $InGa_{0.53}As_{0.47}$ should be grown on top of an InP wafer, after which an InP layer should be grown. This way the recipe for the growth of these structures wouldn't have to change.

Problems arise however when looking at the current used wafer. Literature shows that InGaAs does not grow a smooth thin layer on top of InP(111), instead in grows pyramidal hillocks.[41] Figure 98 shows an example of those pyramidal hillocks, where a typical height of the structures is 0.8 micrometre. The side facets are different (110) directions.

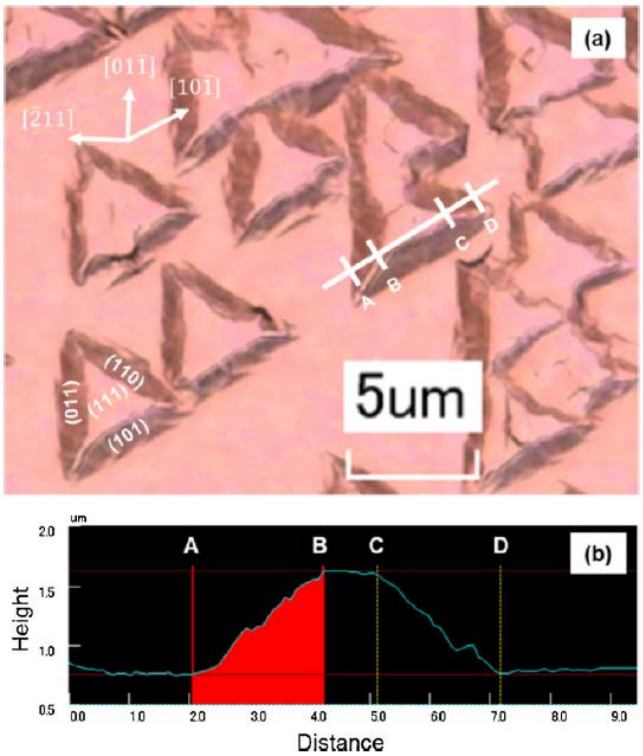


*Figure 82: CLMS image of InGaAs surface on on-axis(InP(111)A substrate. The lower image is a linescan profile of a triangular pyramidal hillock.*

A solution could be to grow the structures on an InP(100) substrate, as the growth of an epitaxial layer of InGaAs on InP(100) is well established. This has been tried but the right parameters, if they exists, were not found. Thermal annealing could maybe improve the odds. The use of InP(100) as substrate is discussed in chapter 6.4. Another solution would be to find another lattice matched material.

## 6.4 InP(100) substrate with thermal annealing

Instead of growing on an InP(111)B substrate, InP(100) could be used as well. The benefits of this orientation are the 90° angles with the same crystal directions, where for the InP(111)B different crystal facets have to be used to create 90° angles (this is described in chapter 4.1) and the possibility to grow a N-doped InGaAs global backgate, as described in chapter 6.3. The downside of this substrate is that the growth of InSb on top is much harder to control, and the defects that form are not parallel to the interface but inclined. Decreasing the number of defects could be done by growing an AlInSb buffer layer first, described in the next chapter.

Several attempts have already been made to find the right growth conditions. Results are shown in figure 99. The SEM images show that the InSb does not fill the trenches nicely. For these attempts the thermal annealing procedure was never performed. Combining this could make it possible to grow on an InP(100) substrate.

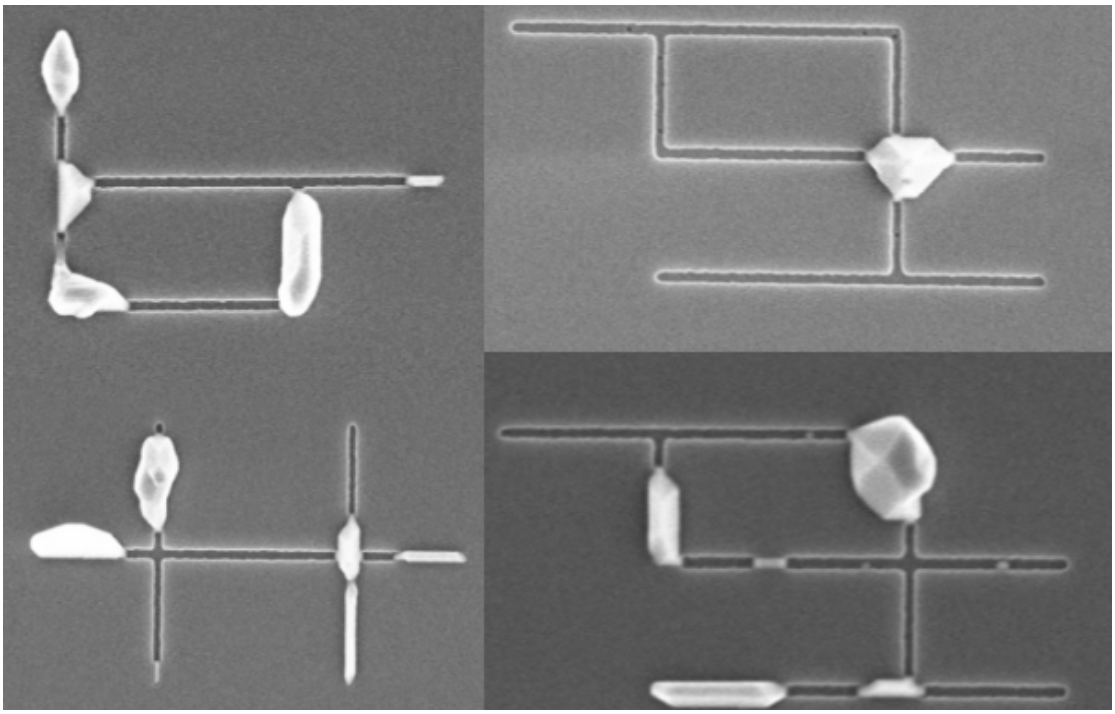

*Figure 83: SEM images of InSb growth on an InP(100) substrate. The nucleations start to form blobs rather than filling the trenches. Thermal annealing to remove the native oxides could maybe improve the growth.*

## 6.5 AlInSb buffer layer

Currently the InSb in-plane networks are grown directly on top of the lattice mismatched InP. This results in defects at the interface which could decrease the electrical properties of the InSb network. It seems that these defects don't affect the top layer of InSb, but if they would, a buffer layer could solve the problem. The layers are shown in figure 100 with corresponding lattice constants. A buffer layer of the ternary alloy AlInSb almost lattice matched with InSb would ensure a safe transition between these two layers.

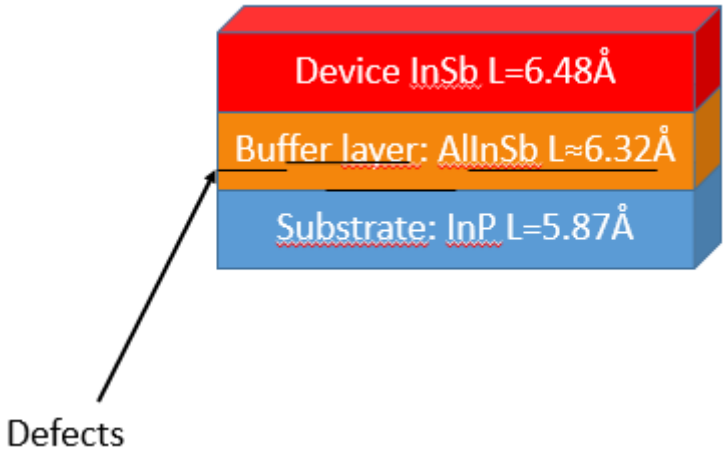


*Figure 84: Illustration of the buffer layer with corresponding lattice constants. The buffer layer relaxes when grown directly on the InP with help of defects. The small lattice mismatch between InSb and AlInSb would not cause defects.*

The buffer layer would have a lattice mismatch with InP. With help of defects like misfit dislocations the buffer layer relaxes. Due to the small lattice mismatch between InP and InSb the InSb would be able to accommodate for the lattice mismatch without forming defects.

As the defects resulting from growing InSb directly on InP seem to stay at the interface, there is no need for a buffer layer at this point. Would future research indicate that the defects still decrease the electrical properties, an AlInSb buffer layer could save the day. For now it would only make the design more complicated than need be. This AlInSb buffer layer could also be used when the InP(100) substrate is utilized.

## 6.6 Flake study

The flake project has up until now not shown tremendous results as shown in chapter 4.5. Changing the growth parameters could already improve the yield. The effect of thermal annealing on the flake forming has not been studied, it could be that these native oxides are the cause of the bad yield. Designs to maximize the total area have already been made. TEM results from the flake project up until now show that there are inclined twin boundaries present in the flakes. If these are required for flake growth is not known. These inclined twin boundaries are shown in image 101.

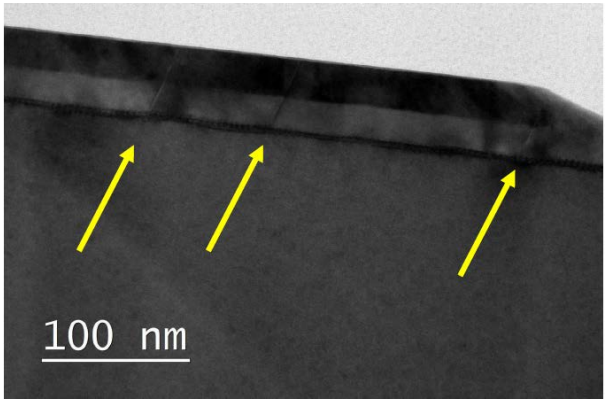


*Figure 85: TEM image of a flake showing inclined twin boundaries starting from the InP/InSb interface. The three twin boundaries are indicated by the yellow arrows.*

SEM-images made from a thermal annealed sample with networks shows large InSb flakes in the numbers. These numbers are very large and just meant to make finding the designs easier. This growth seems not to be limited to special directions as shown in image 102 on the left side. The right side shows a zoomed in image of a corner, where it looks like the InSb crawls over the InP substrate like a glacier. The small white structures could be small InSb nucleations or leftovers from the SiN mask, as the dose was not calibrated for the numbers. The height of this InSb flake is not known but could be around 20-50 nanometre.

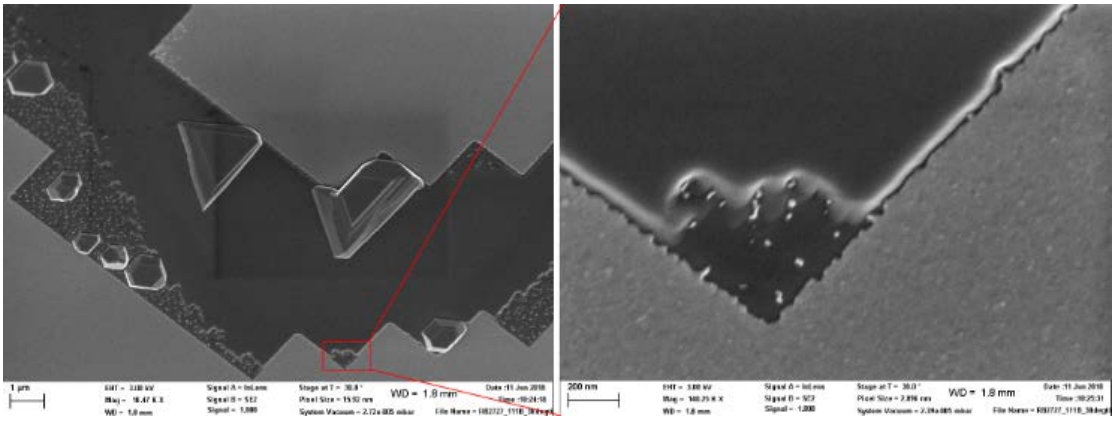

*Figure 86: SEM images showing large InSb flakes on a thermal annealed sample.*

## 6.7 Series with (different) thermal annealing

The Indium, Antimony and time series discussed in the result section of this report are done without thermal annealing. Simply because the effect of thermal annealing was discovered later on. However, the thermal annealing and thereby removing native oxides and changing the surface energy could change the nucleation and growth process drastically. Therefore new series with thermal annealing could be interesting.

Due to Phosphor evaporation thermal annealing is difficult without a Phosphine($PH_3$) pressure in the chamber. The recipe now is to heat up under 306.25 sccm of $PH_3$. After heating till the temperature exceeds 780°C, the chamber is stabilized for 5 minutes at 750°C. In the next 5 minutes the $PH_3$ value is dropped to 80 sccm, after which the system is kept at these conditions for 5 more minutes before cooldown. This Phosphine stays in the chamber and could contaminate the InSb crystalline nanowire. Therefore the thermal annealing is now done in reactor A, while the growth is done in reactor B. These reactors are connected to the same glovebox so the wafer stays oxide free. It would be easier to do the thermal annealing in the same reactor. There is a chance that it would work at a specific temperature and time without a Phosphine pressure. Literature[42] suggests a temperature of 458°C. As the surface temperature is around 30-40°C less than the temperature setting, the temperature setting should be around 490-500°C for 2-5 minutes.

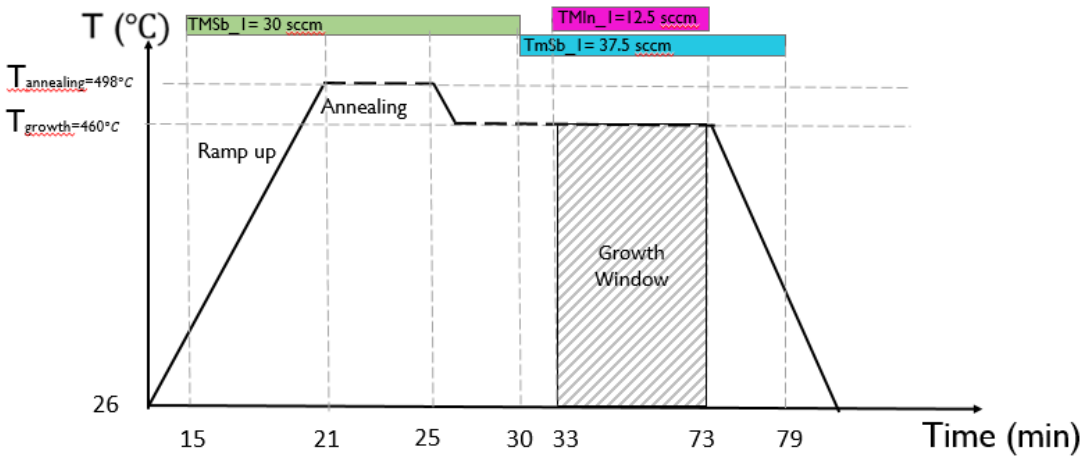


*Figure 87: Growth scheme with temperature and time. First a high temperature is reached for annealing, after which the system goes back to the growt temperature and opens the TMI line.*

# 7 References and Acknowledgements

## References


1. Popkin, G. Quest for qubits. *Science (80-. ).* **354,** 1090–1093 (2016).
2. Kitaev, A. Unpaired Majorana fermions in quantum wires. (2000). doi:10.1070/1063-7869/44/10S/S29
3. Kitaev, A. Y. Fault-tolerant quantum computation by anyons. *Ann. Phys. (N. Y).* **303,** 2–30 (2003).
4. Alicea, J., Oreg, Y., Refael, G., Von Oppen, F. & Fisher, M. P. A. Non-Abelian statistics and topological quantum information processing in 1D wire networks. *Nat. Phys.* **7,** 412–417 (2011).
5. Friedl, M. *et al.* Template-assisted nanowire networks for scalable topological quantum computing schemes. 1–20 (2018).
6. Microchip transistor size, 2000-2020. Available at: www.futuretimeline.net.
7. Hal, G. van. *De quantum computer: Een digitale revolutie op het punt van uitbreken*. (Veen Media, 2017).
8. David Mermin, N. *Quantum computer science- An introduction*. (Cambridge university Press, 2007).
9. Van Weperen, I. *et al.* Spin-orbit interaction in InSb nanowires. *Phys. Rev. B - Condens. Matter Mater. Phys.* **91,** 1–21 (2015).
10. Vaitiekėnas, S. *et al.* Selective area grown semiconductor-superconductor hybrids: a basis for topological networks. 1–6 (2018). doi:arXiv:1802.04210v1
11. Gazibegovic, S. *et al.* Epitaxy of advanced nanowire quantum devices. *Nature* **548,** 434–438 (2017).
12. Krizek, F. *et al.* Scalable quantum nanowire networks grown by molecular beam epitaxy. (2018).
13. Desplanque, L., Bucamp, A., Troadec, D., Patriarche, G. & Wallart, X. In-plane InSb nanowires grown by selective area molecular beam epitaxy on semi-insulating substrate.
14. Del Alamo, J. A. Nanometre-scale electronics with III-V compound semiconductors. *Nature* **479,** 317–323 (2011).
15. Leijnse, M. & Flensberg, K. Introduction to topological superconductivity and Majorana fermions. *Semicond. Sci. Technol.* **27,** (2012).
16. Christian-Albert Universitat zu Kiel. 5.1.4 Wavelength Engineering. **4,** 4–7 (2011).
17. Vesta, J. M. http://jp-minerals.org/vesta/en/. Available at: http://jp-minerals.org/vesta/en/.
18. Chi, C. Y. *et al.* Twin-free GaAs nanosheets by selective area growth: Implications for defect-free nanostructures. *Nano Lett.* **13,** 2506–2515 (2013).
19. Donnay, J. D. H. mineralogy. *Encycl. Earth Sci.* 149–150
20. Venables, J. A. Introduction to surface and thin film processes. 256 (2003). doi:10.1016/S0042-207X(00)00430-9
21. Bauer, E. *Zeitschrift für Kristallographie - Crystalline Materials*.
22. Ucer, K. B. NAN242 - Thin Film Fabrication (Epitaxy). *Wake For. Univ.* (2010).
23. Hoflund, G. B. & Corallo, C. F. A characterization study of the native Oxide layer formed on chemically Etched InP (111). *Surf. Interface Anal.* **9,** 319–323 (1986).
24. Stringfellow, G. B. *Organometallic Vapor-Phase Epitaxy (Theory and practice)*. (Academic Press, 1989).

25. Price, S. J. W. & J.P.Richard. Determination of Conditions for the Suppression of ... *Can. J. Chem.* **50,** 996 (1971).
26. Price, S. J. W. The Decomposition of Metal Alkyls, Aryls, Carbonyls and Nitrosyls. *Compr. Chem. Kinet.* **4,** 197–257 (1972).
27. Larsen, C. A., Gedridge, R. W., Li, S. H. & Stringfellow, G. B. Decomposition mechanisms of Antimony Source Compounds for Organometallic Vapor-Phase Epitaxy. *Mater. Res. Soc. Symp. Proc.* **54,** 255–263 (1990).
28. Buchan, N. I., Larsen, C. A. & Stringfellow, G. B. Mass spectrometric studies of trimethylindium pyrolysis. *J. Cryst. Growth* **92,** 591–604 (1988).
29. Riesz, F., Dobos, L., Vignali, C. & Pelosi, C. Thermal decomposition of InP surfaces: Volatile component loss, morphological changes, and pattern formation. *Mater. Sci. Eng. B Solid-State Mater. Adv. Technol.* **80,** 54–59 (2001).
30. Chu, S. N. G. Morphological Study of Thermal Decomposition of InP Surfaces. *J. Electrochem. Soc.* **130,** 2398 (1983).
31. Mojzes, I., Veresegyh, R., Kov, B. & Malina, V. metal fim barrier against the evaporation of volatile components during the heat treatment of metail-compound semiconductor contacts. **164,** 4–7 (1988).
32. Bayliss, C. R. & Kirk, D. L. The compositional and structural changes that accompany the thermal annealing of (100) surfaces of GaAs, InP and GaP in vacuum. *J. Phys. D. Appl. Phys.* **9,** 233–244 (1976).
33. *Cleanroom Specifications*.
34. o.h. Veld & Roy. Scalable InSb nanowire networks for Majorana braiding Go no-go proposal. (2017).
35. Ju, W., Gulino, D. A. & Higgins, R. Epitaxial lateral overgrowth of gallium nitride on silicon substrate. *J. Cryst. Growth* **263,** 30–34 (2004).
36. Plugge, S., Rasmussen, A., Egger, R. & Flensberg, K. Majorana box qubits. *New J. Phys.* **19,** (2017).
37. Klavs F. Jensen. Microelectronics Processing. **221,** 199–263 (1989).
38. Abudayyeh, H. Synthesis and Analysis of ZnO Nanowires. (2012). doi:10.1016/j.jcrysgro.2008.07.049
39. Nania, S. L. & Shaw, S. K. Analysis of fluid film behaviour using dynamic wetting at a smooth and roughened surface. *Anal. Methods* 7242–7248 (2015). doi:10.1039/C5AY00574D
40. Beach erosion. Available at: https://www.etutorunplugged.com/sample/lesson/earth-art-erosion/learn-and-resources. (Accessed: 28th May 2018)
41. Yamada, H., Ichikawa, O., Fukuhara, N. & Hata, M. Formation and Reduction of Pyramidal Hillocks on InGaAs / InP ( 111 ) A. **121101,** 135–136 (2015).
42. Lau, W. M., Sodhi, R. N. S. & Ingrey, S. Thermal desorption of oxides on InP. *Appl. Phys. Lett.* **52,** 386–388 (1988).
43. De Gennes, P.-G. Comptes rendus hebdomadaires des séances de l â€™ Académie des sciences . Série B. *Comptes rendus Hebd. des séances l â€™ Académie des Sci. Série B* **275,** 319–321 (1972).
44. Thomson, G. W. The antoine equation for vapor-pressure data. *Chem. Rev.* **38,** 1–39 (1946).
45. Shenai-Khatkhate, D. V., DiCarlo, R. L. & Ware, R. A. Accurate vapor pressure equation for trimethylindium in OMVPE. *J. Cryst. Growth* **310,** 2395–2398 (2008).
46. Fulem, M. *et al.* Vapor Pressure of Trimethylantimony and. 362–365 (2010).
47. Bour, D., Yang, Z. & Chua, C. Simple technique for measuring the filled volume

of liquid or solid CVD precursor chemicals in bubblers. *J. Cryst. Growth* **310,** 2673–2677 (2008).
48. Hurt, R. Mechanisms of emission of secondary electrons, backscattered electrons, and characteristic X-rays from atoms. Available at: https://commons.wikimedia.org/wiki/File:Electron_emission_mechanisms.svg.
49. ZEISS. ZEISS GeminiSEM - Field Emission Scanning ELectron Microscope. Available at: https://www.zeiss.com/microscopy/int/products/scanning-electron-microscopes/geminisem.html.
50. Australian Microscopy & Microanalysis Research Facility. Scanning Electron Microscope. 1–98 (2014).
51. Myron L Company. Application Bulletin Deionized Water.
52. Madou, M. J. *Fundamentals of Microfabrication and Nanotechnology*. (CRC Press, Taylor and Francis group).
53. Jiao, Y. *et al.* Fullerene-assisted electron-beam lithography for pattern improvement and loss reduction in InP membrane waveguide devices. *Opt. Lett.* **39,** 1645 (2014).
54. Zeon Corporation. Technical Report. (1999).
55. Oxford. Schematic RIE. Available at: https://www.oxford-instruments.com/products/etching-deposition-and-growth/plasma-etch-deposition/rie. (Accessed: 22nd May 2018)
56. BAKER PRS-3000.pdf.
57. Kriegor27. Principe FIB. *wikiipedia* Available at: https://commons.wikimedia.org/wiki/File:Principe_FIB.jpg. (Accessed: 22nd May 2018)
58. Kittel, C. *Elementary solid state physics - a short course*. (Willey, 1962).
59. Oxford Instruments. Plasma enhanced chemical vapour deposition (PECVD). Available at: https://www.oxford-instruments.com/products/etching-deposition-and-growth/plasma-etch-deposition/pecvd. (Accessed: 27th February 2018)

**Acknowledgments**

I would like to thank a few persons for their guidance and help with this research. First of all MSc. Roy op het Veld, my daily supervisor. Thanks for the patience and willingness to help. Special thanks for prof. dr. Erik Bakkers for the overall supervision. Furthermore I would like to show my gratitude for prof. Marcel Verheijen for the TEM-analysis and keen insides in the crystal structures and dr. Sebastian Kölling for the FIB-procedure. I also want to acknowledge the help of all the technicians in the cleanroom for explaining how to operate the machinery and making the growth possible. Lastly thanks to Microsoft for their funding and interest in this research.

# 8 Appendix

In appendix 8.1: A the difference between quantum bits and classical bits is shown briefly. Appendix 8.2: B the guideline for calculating the normal and effective V/III ratio is shown. The effective V/III ratio can be important if one is interested in comparing with literature. The next appendix, 8.3: C, gives a more detailed explanation of the working of a SEM.

Appendix 8.4: D has several chapters, each explaining a part of the sample preparation process and used machines in more detail. Lastly, a few high resolution SEM images are shown in appendix 8.5: E, they were made with a viewing angle of 30°.

## 8.1 A: How qubits differ from classical bits

As told before, the quantum bit is a complete new building block. The new concept of operation results in quantum computing. Quantum computing involves a computation device using quantum mechanical phenomena, mainly entanglement and superposition to perform calculations. All physical interactions will have to be under complete control of the system. Any destructive interaction results in decoherence, which is fatal for the quantum computation. Complete isolation can generally only be achieved in almost atomic size structures, where internal features which can have destructive interaction simply don't exist or require way higher energies to play a part, i.e. a hard gap. [8]

The difference between classical bits (cbits) and quantum bits (qubits) can be demonstrated by describing the values 0 and 1 a cbit can have as vectors, |0> and |1>. Where the cbit is one or the other. By measuring the system and looking at the result, one can for sure say what the status of the cbit was. On the other hand, qubits can have an associated state |ψ> with any unit vector in the two-dimensional vector space from |0> and |1>. In formula this would look like:

$$|\Psi >= \alpha_0|0 > +\alpha_1|1 > \qquad (6)$$

Here $\alpha_0$ and $\alpha_1$ are complex numbers and can have any value with the only requirement that the state |ψ> should be a unit vector as well, so

$$|\alpha_0|\text{^}2 \ + |\alpha_1|\text{^}2 = 1 \qquad (7)$$

When measuring a qubit, the outcome could be 0 or 1 again with a certain probability. But after a physical measurement of the state, the information hidden in the amplitudes is lost, this is sometimes referred to as the collapse of the system. Born rule provides a link between the amplitudes and the measurement result, but will not be discussed here. Figure 104 illustrates the difference between the cbits and the qubits.

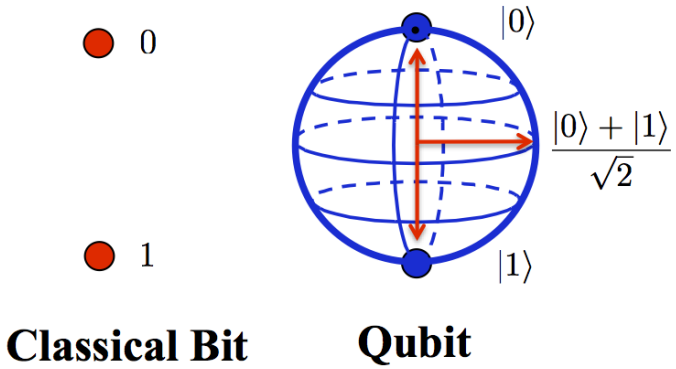


*Figure 88: Image comparing a classical bit with a qubit. The only restriction of the state of a qubit is that it is still an unit vector. Meaning that the probabilities at up to one.*

Where the general state of a n-cbit system is simply the product of the two 1-cbit states, this is not necessary true for qubits. In general the state of a n-qubit system is not the product of the n 1-qubit states. This is commonly referred to as entanglement.

## 8.2 B: Guideline for calculating the (effective) V/III ratio

First the vapour pressure $P_{vapour}$ can be calculated using the Antoine equation[43], shown in equation 8 and 9. Literature suggests this as the easier way to go compared to the Henglein equation.[44] Where the bubbler temperature $T_B$ for $TMI$ is -10°C (263.15K) and the $T_B$ for the $TMSb$ is 17°C (290.15K). The bubbler cylinder is a segment of the MOVPE where a liquid precursor is conveyed into an useful mixed vapour. By means of a hydrogen flow bubbling through the precursor liquid like a hottub. Control over the temperature ensures a constant steam pressure. The bubbler pressure $P_B$ is for both cases 500 mbar.

$$\log\left(P_{vapour}(Torr)\right) = a - \frac{b}{T_B(K) + c} \tag{8}$$

$$P_{vapour}(Torr) = 10^{a - \frac{b}{T_B(K)+c}} \tag{9}$$

Where $a$,b and $c$ are variables which depend on the material. The following table 2 gives the values for different precursors, determined in literature. In literature different variables were found. The most trusted results are in bold, these have been used.

*Table 2: Overview of the constants a, b and c of Antoine's equation for different precursors. All values are from literature.*

| | **TMI**[45] (Torr) | TMI[24] (Torr) | TMSb[46] (Pascal) | **TMSb**[24] (Torr) |
|---|---|---|---|---|
| a | 10.98 | 10.52 | 21.0431 | 7.7078 |
| b(K) | 3204 | 3014 | 3000.32 | 1697 |
| c | 0 | 0 | -37.366 | 0 |

The vapour pressure in Torr as a function of the temperature in kelvin is shown in figure 105. With the TMSb in orange and the TMI in blue.

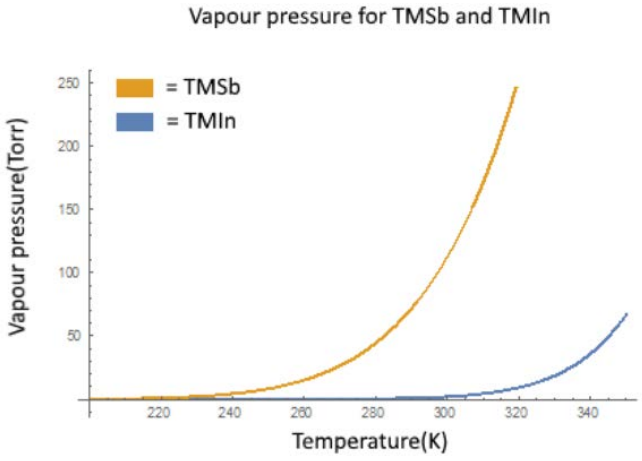


*Figure 89: Vapour pressure in Torr as a function of temperature in Kelvin. The TMSb vapour pressure is shown in orange and the TMI in blue*

Now it is easy to calculate the vapour pressure. The vapour pressure is now defined in units of Torr, for convenience it can be rewritten in units of mbar using the relation in equation 10.

$$P(mbar) = \frac{P(Torr)}{0.7500616827042} \tag{10}$$

From the calculated vapour pressure, given bubbler pressure and source flow, the molar flow can be calculated using equation 11. [47] The molar flow represents the amount of precursor material that is present in the mixture.

$$f_{molar}(sccm) = \frac{P(mbar)}{P_B(mbar) - P(mbar)} f_s(sccm) \tag{11}$$

The molar flow can again be converted in other units for convenience. The molar flow in mol per minute is found by using equation 12.

$$f_{molar}\left(\frac{mol}{min}\right) = f_{molar}(sccm) * 0{,}00000074 * 60 \tag{12}$$

Finally, the molar fraction of each compound and ratio can be calculated by using the molar flow and the total volume flow.

$$F_{molar} = \frac{f_{molar}(sccm)}{V_{totalflow}(sccm)} \tag{13}$$

$$V/III = \frac{F_{molar,Sb}}{F_{molar,In}} \tag{14}$$

During all measurements the total flow volume $V_{totalflow}$ has been kept at a constant 6000 sccm. To lower the amount of growing material and keep the total flow constant, more non-reactive gas $h_2$ must be used to compensate. Dividing the molar fraction of the Antimony with the Indium molar fraction will give the V/III ratio in the chamber as shown in equation 14. For more accurate results, the V/III ratio can be calculated while having the cracking efficiency in mind. The amount of precursors which will be cracked, thus be available for growth, depends on the temperature. Different equations are used to estimate the cracking efficiency for each precursor.

For the cracking efficiency (CE) of TMI, the pyrolysis reaction speeds and dependence on temperature are important. A graph from literature showing the cracking efficiency is already shown in chapter 2.5. The CE of TMI while having a surface temperature ~425°C is around 100%. Richards' equation can be used, with the following solution:

$$CE_{In} = a * \left(1 + (d-1) * \exp\left(-k * (x - x_c)\right)\right)^{\frac{1}{1-d}} \tag{15}$$

Where $a = 98{,}85129$, $x_c = 329{,}1$, $d = 5{,}23518$ and $k = 0{,}20787$.

At last, the CE of TMSb can be calculated by using the equation of Gompertz.

$$CE_{Sb} = a \exp\left(-exp\left(-k * (x - x_c)\right)\right) \tag{16}$$

Where $a = 2180{,}913$, $x_c = 607{,}39869$ and $k = 0{,}00835$

The cracking efficiencies are shown in figure 106 as a function of the temperature.

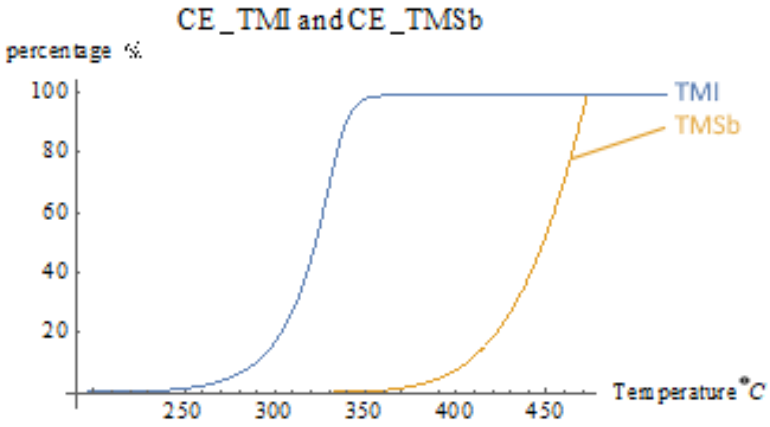


*Figure 90: Cracking efficiencies (CE's) of TMI and TMSb as a function of temperature. TMSb cracks at a higher temperature than TMI as expected.*

The effective V/III ratio is now given by:

$$V/III_{effective} = \frac{F_{molar,Sb} * CE_{sb}}{F_{molar,In} * CE_{In}} \tag{17}$$

## 8.3 C: Know-how of the SEM

Here the know-how of the SEM is explained. When the primary electron (PE) from the electron beam hits an atom, it can ionize the atom by darting away an electron. This electron is called the secondary electron(SE). Another possibility is that the electron moves through the material and gets reflected. The primary electron turns around and can reach an Inlens Energy selected Backscatter detector (EsB) as the back scattered electron (BSE). The produced images in this research are a result of signals coming from secondary electrons (SE), the back scattered electrons (BSE) are not used. These processes are shown in figure 107.[48] The back scattered electrons typically penetrate deeper into the surface, consequently the secondary electrons tell more about the top layer of the surface.

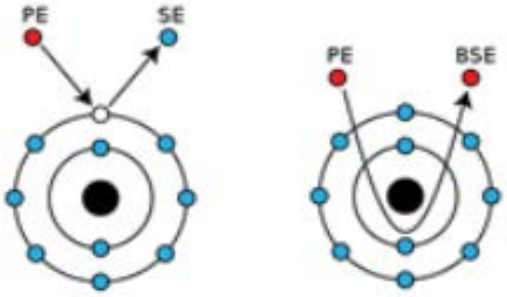


*Figure 91: Schematic view of the process creating secondary electrons on the left and backscattering electrons on the right side. Image is reworked from the original*

This SEM has a Gemini InLens detection, which ensures efficient signal detection of SE's minimizing time-to-image. Figure 108 shows a schematic of the SEM.[49] A field emission(FE)-gun creates the electron beam after which a column/ beam booster, scan coils and electrostatic lens changes the beam before it hits the sample. The beam booster consists of a condenser and magnetic lens. The condenser is used to spread the beam as efficient and evenly possible across the sample. The SE's travel back up, where the SE's are captured by the InLens SE detector.

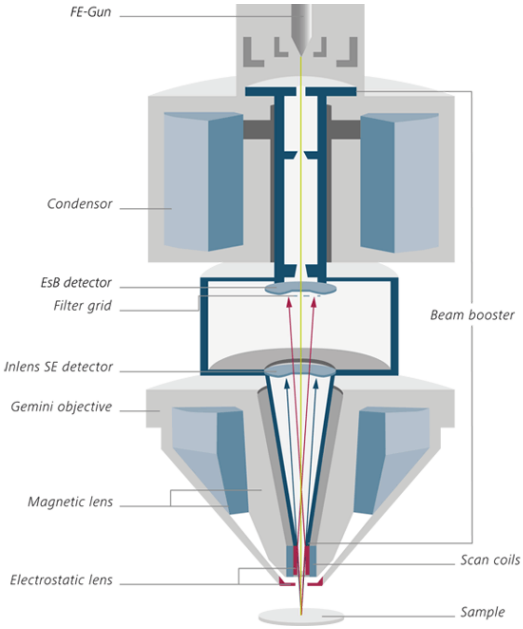


*Figure 92 : Schematic of the SEM. A FE gun creates the electron beam after which it moves through a column before reaching the sample where it reflects back to the detectors.*

Figure 109[50] shows most of the processes happening when an electron beam hits a surface. Secondary electrons are created at the surface where the primary electrons collide with them. Back scattered electrons move deeper into the top layer before they are reflected back up. An excited electron can relax to a lower state without emitting

radiation. When the released energy is given to another electron, this second electron can escape the orbit around the nucleus, these electrons are called Auger electrons.

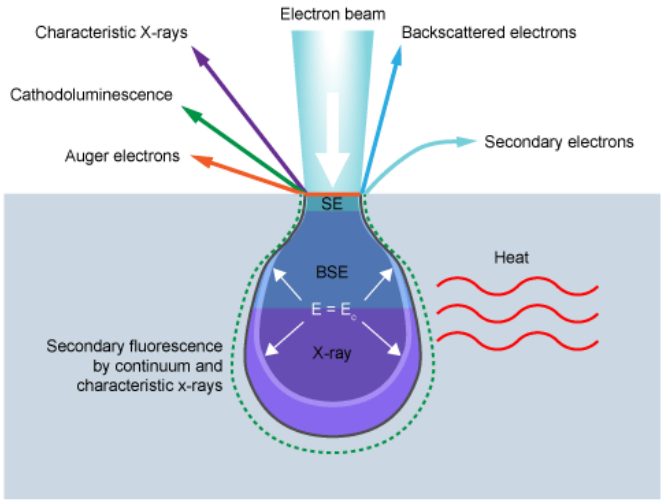


*Figure 93: Schematic view of the processes that can happen when an electron beam hits a surface. Observe the different penetration depths.*

## 8.4 D: Details of sample preparation

Several preparation steps are necessary before growth. Almost every step is very sensitive and a small change could influence the end result. Therefore every procedure and machine is explained in more detail in this appendix. The last chapter explains the FIB procedure to make an ultrathin filament of the sample for TEM-analysis.

### 8.4.1 Phosphoric acid dip

An InP wafer right from the manufacturer undergoes a cleaning step before the fabrication starts. The standard pre-treatment for InP is the deoxidation of the surface because surface oxides can cause passivation of the surface. This is done by a phosphoric acid dip for 3 minutes. The phosphoric acid is a 10 ml $H_3PO_4$ – 100 ml $H_2O$ solution. Due to its polarity phosphoric acid dissolves easily in water. The dip makes the surface more hydrophobic, this is a good check to see if the deoxidation has been done correctly. After the deoxidation the wafer is rinsed with a DeIonized (D.I.) water bath. The resistance of a continuous flow of D.I. water is measured and the wafer is dried with $n_2$ after the resistance of the water reaches 8MΩ or higher.

The Phosphoric acid ionizes upon dissolving in water. The following equations describe the 3 steps in this process. It is important to note that in a water environment only the first reaction is of real influence. The other two reactions almost never happen. This phosphoric acid solution has around 0.49 mol/L. Resulting in 83% $H_3PO_4$ and 17% $H_2PO_4^-$)

$$H_3PO_4 + H_2O \rightarrow H_3O^+ + H_2PO_4^- \quad (18)$$

$$H_2PO_4^- + H_2O \rightarrow H_3O^+ + HPO_4^{2-} \quad (19)$$

$$HPO_4^{2-} + H_2O \rightarrow H_3O^+ + PO_4^{3-} \quad (20)$$

Resistivity/conductivity gives a good estimation of how clean the water is. As shown below the water gets more resistive if the pureness increases. A resistivity of 8 MΩ, frequently used in this research, is at the border between pure water and ultra-pure water, as shown in figure 110. [51]

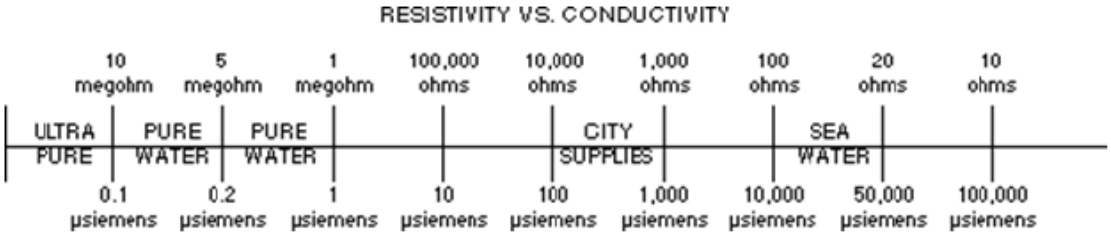


*Figure 94: Resistivity and conductivity of water with the associated level of cleanliness. A difference between city supplies and ultra-pure water is easily detectable with this method.*

This same procedure has been used for every wafer. Moreover the same method is again used to deoxidize the surface right before growth.

### 8.4.2 PECVD

Plasma enhanced chemical vapour deposition (PECVD) is used to deposit a thin layer of SiN on the surface. PECVD, compared to normal chemical vapour deposition (CVD), uses a gas plasma to lower the temperature required to grow a thin film. [52] With help of a radiofrequency (RF) plasma it produces energetic electrons which in turn collide with the neutral precursors. This way the deposition precursors can be produced at a lower temperature. The ion bombardment of the surface also enhances the number of dangling bonds, increasing the efficiency. In this research SiN is used as a passivation layer and increaser of the diffusion length. Equation 21 shows the chemical process happening in the chamber.

$$3SiF_4 + 4NH_3 \rightarrow Si_3N_4 + 12HF \quad (21)$$

The PECVD from Oxford Instruments(see figure 111) is used to deposit the protection layer of SiN on a clean InP(111)B wafer. The standard waveguide SiN (50nm) program is used for 1 minute and 24 seconds, resulting in a SiN layer of ~20nm. This is verified with a refractometer. The refractometer measures the index of refraction by using Snell's law. The index of refraction is different for each material, making it possible to determine the type of material. If the wafer parameters are known as well as the material of the thin epitaxial layer, the bending can be used to calculate the thickness of the thin epitaxial layer via the transmission angle. The PECVD from Oxford operates while using the standard waveguide program at an input flow of the precursors of 17sccm $SiH_4$ ,13 sccm $NH_3$ and 980 sccm $N_2$. So a total flow of 1010 sccm runs through the chamber. The temperature during the process is an almost normal room temperature of 300 Kelvin. The RF source operates at 13.56MHz as shown in figure 111 with 20 Watt and the pressure inside the chamber is 650mTorr.

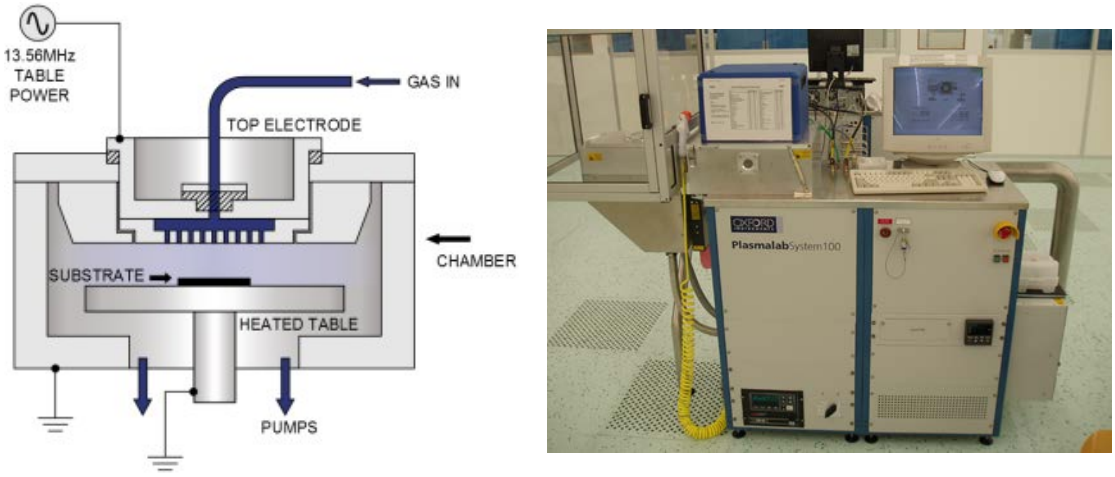


*Figure 111: Left image[59] shows a schematic view of the PECVD by Oxford Instruments. The RF source works at 13.56MHz producing a plasma. A showerhead is used for the gas input right above the sample. The figure on the left shows the actual PECVD from Oxford.*

The figure on the right side shows the actual device. On the left side a loadlock ensures a low pressure of 650mTorr. The thickness depends more or less linearly on the growth time with a deposition speed of ~13.87 nm/min.

### 8.4.3 Spin coating

Before the Ebeam can be used to create the desired pattern in the SiN mask, a positive resist must be applied on the SiN layer. First the wafer is cleaned with $N_2$ to minimize the contaminations on the surface. The wafer is put in the spin coater and is covered with the positive resist, in this case ZEP520A+C60 (described in chapter 8.4.3.1). It spins with 2000RPM for 60 seconds, resulting in a positive resist layer. The resist needs to bake to form polymers and harden. This is done for 10 minutes with a linearly increasing temperature from 125° Celsius to 200° Celsius. After which it is baked for 5 more minutes at 200° Celsius.

The positive photoresist is dispensed by use of a syringe onto the wafer. The wafer is hold in place in the resist spinner by a vacuum chuck. The wafer is spinned for 60 seconds at a speed of 2000 rotations per minute. The end thickness T of the photoresist layer depends on the speed $\omega$, the polymer concentration C, the intrinsic viscosity $\eta$ and the overall calibration constant K as described in equation 22.[52]

$$T = K * \frac{C^{\beta}\eta^{\gamma}}{\omega^{\alpha}} \tag{22}$$

The photo resist leaves unwanted purple residues in the spin coater. This has been removed immediately with Acetone to prevent stains and contamination. Figure 113 shows the resist spinner with vacuum chuck. In this case a syringe with a special filter has been used as the photoresist dispenser. The filter prevents larger polymers to reach the wafer. Acrodisc® CR 13 mm syringe filters have been used with a 0.2 µm PTFE membrane. If contaminants like large polymers or dust still reach the liquid resist layer before resist spinning, stripes like figure 113 on the right side can be caused. The image seems yellow due to the special lights in that section of the cleanroom. As photo resists are meant to be sensitive to light, special light is needed to prevent unwanted exposure of the photoresist to light of shorter wavelengths.

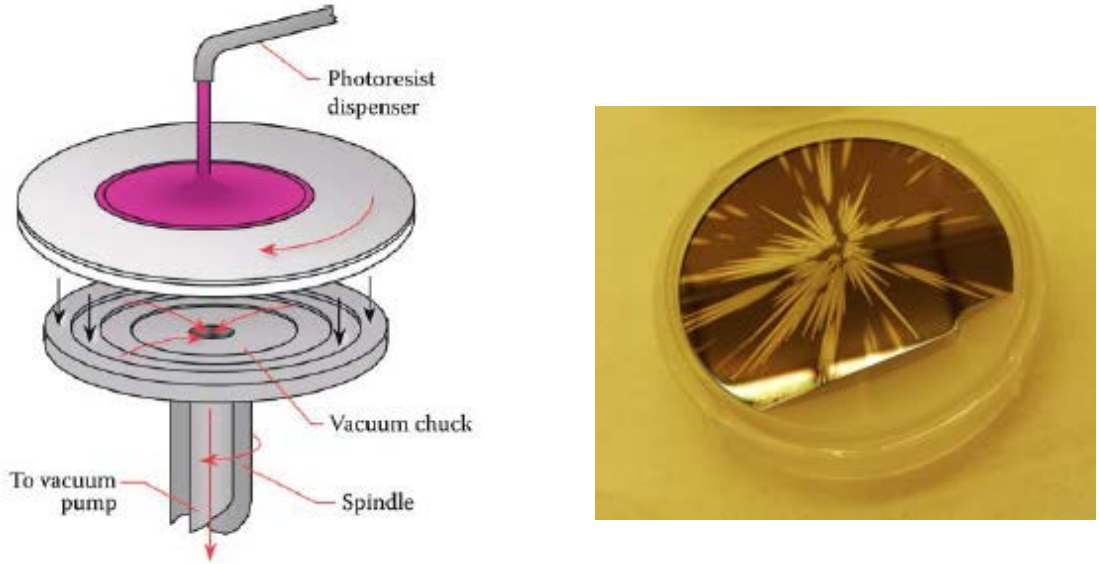


*Figure 112: Left: Schematic view of a resist spinner with vacuum chuck. The photoresist is dispensed on the wafer with a syringe and special filter. If larger polymers are not filtered out of the resist or dust attaches to the liquid resist, stripes may occur as shown on the left.*

### 8.4.3.1 Resist: ZEP520A+C60

A typical resist consists of a polymer(base resin), a sensitizer and a casting solvent. The base resin reacts to the baking by forming extra bonds (polymers). The solvent allows spin applications and the sensitizer controls the polymer formation. ZEP520A+C60, used in this experiment, is a two component resist, which means it uses a sensitizer. Our resist is positive, meaning that the Ebeam exposure weakens the polymers by scission of the polymer chains.

The positive resist used in this research is ZEP520A+C60. This a combination of ZEP520A and fullerene (also called buckyballs). This combination results in better thermal resistance which improves the exposure of nanometre designs. [53] Figure 113 shows the difference between normal ZEP520A resist and the mixed ZEP520A+C60 resist. Where the gap in figure 3.b is 90 nanometre. Figure 4 shows the chemical structure if ZEP520A, the polymers formed during baking consist of these monomer building blocks.

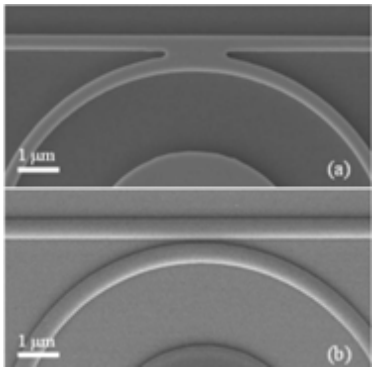


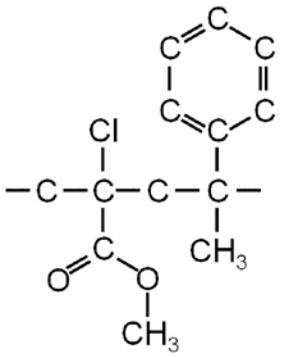


*Figure 95: Figure a on the left side shows a design after exposure with a normal ZEP520A resist. Figure b shows the same design with the mixture resist of ZEP520A and fullerene. The gap between the 2 regions is 90nm. Observe the difference in resolution. The figure on the right side shows the chemical formula for ZEP520A in monomer formation*

The C60 added to the ZEP520A is a ball made from Carbon atoms. Buckyballs are composed of carbon atoms linked to three other carbon atoms by covalent bonds. The carbon atoms are connected in the same pattern of hexagons and pentagons you find on a soccer ball, giving a buckyball the spherical structure as shown in the following figure 114 on the left side. The right image shows the thickness of the resist layer corresponding to each spin speed in rpm for ZEP520A and another version.[54] In our case the 2000 RPM corresponds to a thickness of around 5000Å. (0.5μm)

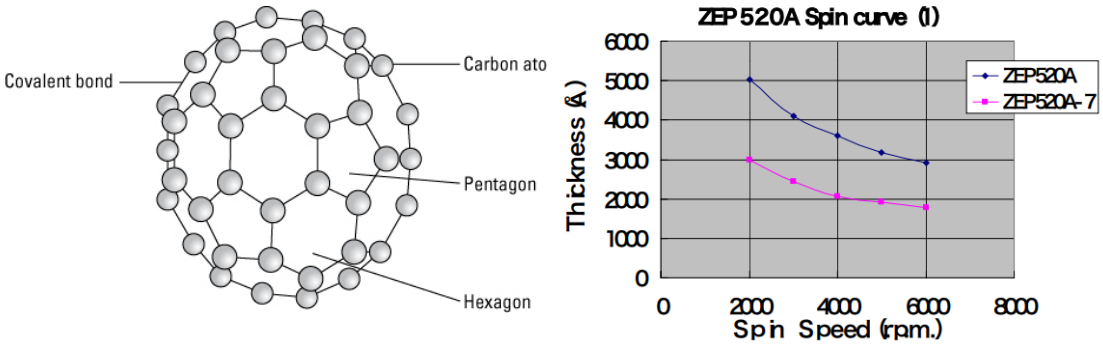


*Figure 964: Schematic view of a buckyball on the left, alternating pentagons and hexagons, often compared with a football. The right image shows a calibration of the thickness of the resist as a function of the spin coat speed (rpm).*

### 8.4.4 Electron beam lithography

Electron beam lithography (EBL) in combination with a positive resist is used in this research to write the design. After spin coating the SiN layer the design can be converted into the positive resist (ZEP520A with C60) layer. The electron beam (Ebeam) uses a bundle of electrons and exposes the surface according to the design. The polymers in the positive resist get scissored by the electrons and can be removed later on. This means that the electrons break the extra bonds in the polymers formed during the baking procedure of the resist. The nA and dose of the electron beam needs to be accurately chosen to not overdose the wafer. 0.3nA has been used for the designs in this research with a dose of 850 μC/cm$^2$.

Electron beam lithography generally offers higher patterning resolution compared to light lithography due to the shorter wavelengths associated with 10-100 keV electrons. The desired structures have a width between 20nm and 35nm, making EBL the better option. As there is no need for a physical mask, designs can be changed easily and without the expensive price tag that comes with a light lithography mask. Another benefit is the possibility to exactly determine different doses for different shapes and sizes in the design. A vacuum is needed to ensure that the electrons don't scatter before reaching the surface. The mean free path of the electrons needs to be bigger than the length from the source to the wafer. The mean free path $L$ can be calculated using:

$$\mathrm{L} = \frac{1}{\pi * \mathrm{d}^2 * n_v} \tag{23}$$

Where d is the diameter of the molecules the electrons can hit with and $n_v$ is the numbers of molecules per unit volume. The ideal gas law is used to calculate $n_v$.

$$\frac{\mathrm{n}}{\mathrm{V}} = \frac{\mathrm{p}}{\mathrm{RT}} = 5 * \frac{10^{-5}}{8{,}314462175 * 290} = 2{,}07366 * 10^{-8} \tag{24}$$

$$\mathrm{L} = \frac{1}{\pi * \mathrm{d}^2 * n_v} = 1{,}066 * 10^{27} m \tag{25}$$

The mean free path is clearly long enough.

The electrons targeted at the surface expose the positive resist. There are three processes responsible for the end result of the exposure. The first process is the forward scattering, the electrons directly hit the surface and expose a small area. The electrons can also cause another electron to leave its orbit around an atom, resulting in a secondary electron. These secondary electrons expose the positive resist as well, increasing the exposed area. For the third process the electrons penetrate deeper into the top layer and are reflected (back scattered) due to the negative potentials. On their way back to the top they expose a larger area. These three processes result in the final size of the exposure area.[52] The processes are shown in figure 115 on the left side. The right image shows the width of the area affected by the forward scattered electrons and the back scattered electrons. Observe the large difference in exposed area between the two.

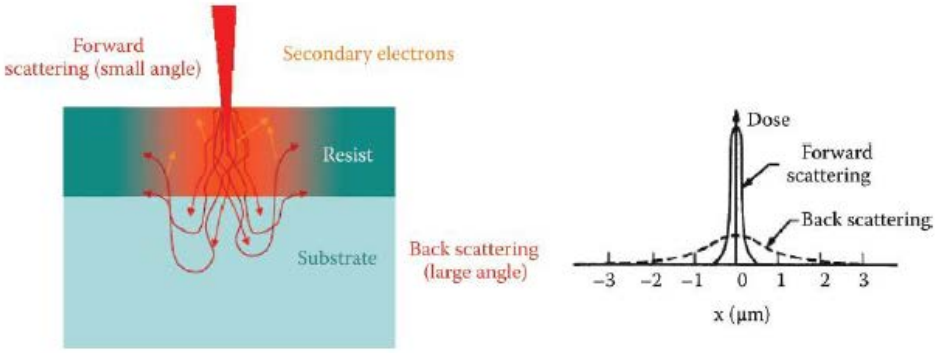


*Figure 115: Left figure shows the three processes responsible for the total exposed area. Where the forward scattered electrons expose the smallest area, the secondary electrons increase the width further and the back scattering electrons are responsible for the end width of the design. Right figure shows the affected respective width for the forward and back scattered electrons.*

With the designs used in this research it is possible that the exposure of one segment causes exposure of other segments by back scattered electrons. (See figure 116)[52]. Therefore a dose test is performed to find the correct dose. Smaller designs have less exposed area around it on average, decreasing the effect of the back scattering thus increasing the required dose. The easiest way to determine the right dose is to perform a dose test. If the dose is not high enough the designs are not completely opened, while overexposure may result in round instead of sharp edges an can damage the substrate.

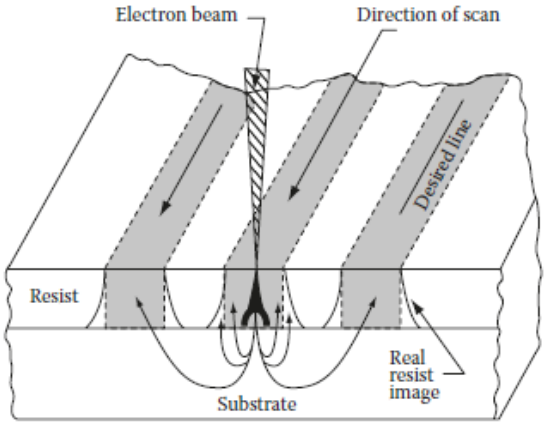


*Figure 116: Designs close to each other may affect the required dose needed to expose the area. The back scattered electrons from the substrate can affect the designs next to it.*

### 8.4.4.1 Autocad and the designs

The luxury of ebeam compared to light lithography is the digital design. Making it possible to have a different design for every exposure. This way there can be experimented with various designs. The designs have been made in Autocad using VBA. Figure 118 shows an example of a design used in our experiments.

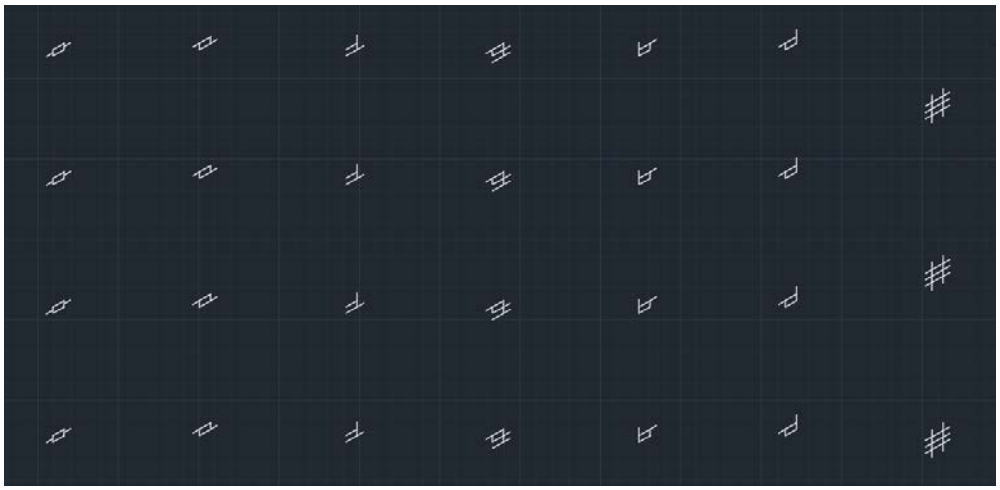

*Figure 97: Autocad file of different designs used in this experiment. The designs are repeated 4 to 10 times above each other. The distance between designs is ten micrometer. Width, height, thickness and angle have been changed to examine the growth.*

The distance between two designs is at least $10\mu m$ to decrease the fluctuations that could occur due to a large diffusion length of the Indium and Antimony on the SiN layer. As the design should have nicely defined corners to prevent strange shapes when using angles, the four points of each corner of each design are connected in a X-fashion, shown in figure 119 on the left side. The lengths, widths, thicknesses of the wires and orientations (angles) on the surface have been varied to study the effects. Numbers to indicate the variables have been modified using the 'explode text' function in Autocad, otherwise the Ebeam software doesn't understand the design. This is shown in figure 119 on the right side. The number is divided in separate blocks with polylines.

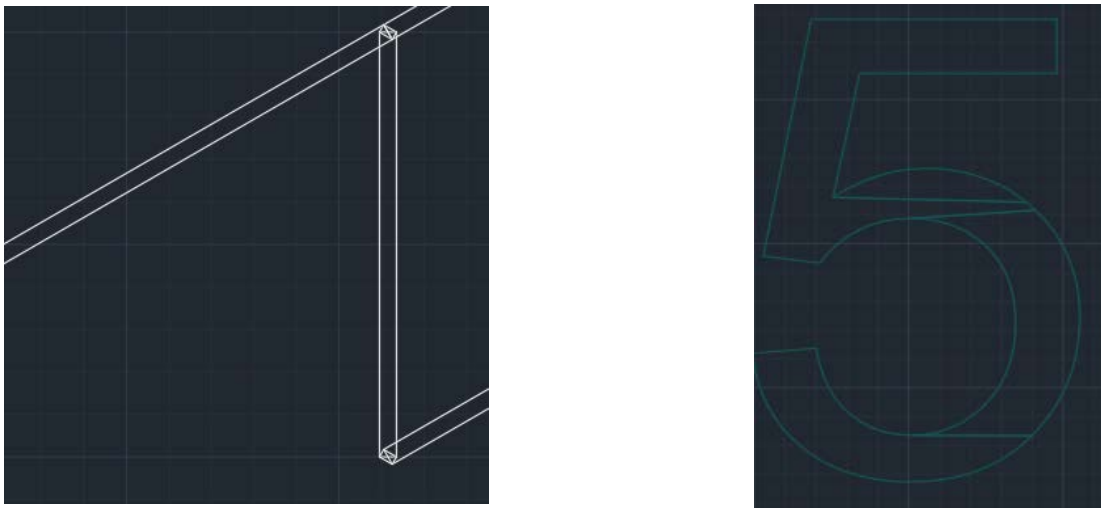

*Figure 98: Left: Each corner is nicely defined in a X fashion, ensuring smooth corners. Right: Exploded text function transforms text and numbers into designs the Ebeam software can understand.*

The beamer software translates the Autocad design into an Ebeam-compatible format. Allocating different doses to different patterns and fix the beam step size and resolution. After the beamer software Cjob is used to make the actual design and repeat it across the whole wafer as figure 120 shows. One colour in figure 120 represents one beamer file and could have its own exposure dose etc. Four different designs can be observed in green, blue yellow and red. These four designs together form one block which is repeated to fill the wafer. In this case all of them have the same exposure dose of 850C/m. The squares are markers surrounding the structures, making it easier to find them. They can also be used to align the Ebeam if multiple exposures are necessary.

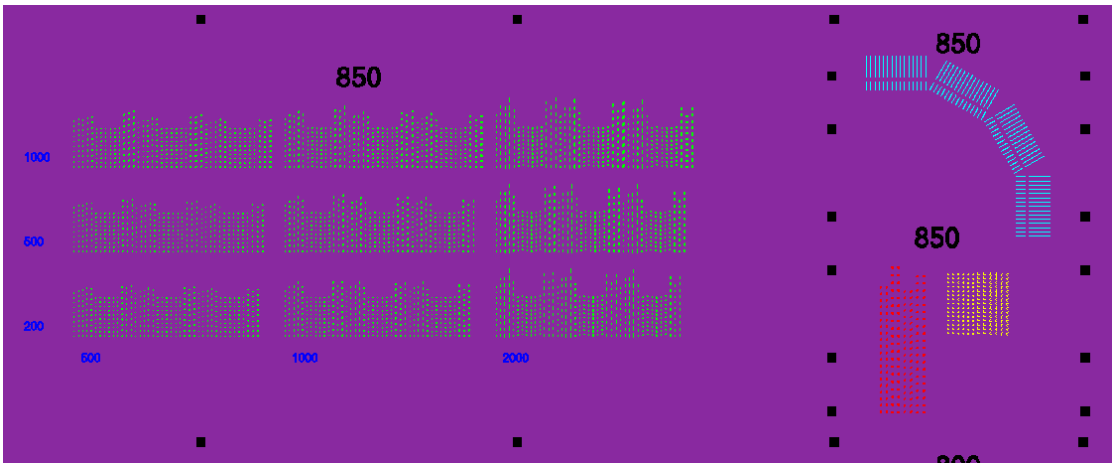


*Figure 99: Illustration of a final design, this block (unit cell) is repeated to fill the wafer. Four different designs can be observed in green, blue, yellow and red. The square markers are used as a guide to find the designs.*

Afterwards the block (unit cell) illustrated in figure 120 is repeated to get to the final design shown in figure 121. The 2 inch wafer is now completely filled with the design. Blocks on the edge which would be partially on the wafer are removed to reduce the exposure time. A typical exposure time for a complex design like this for a 2 inch wafer is around seven hours. The 110 flat can be found on the left side.

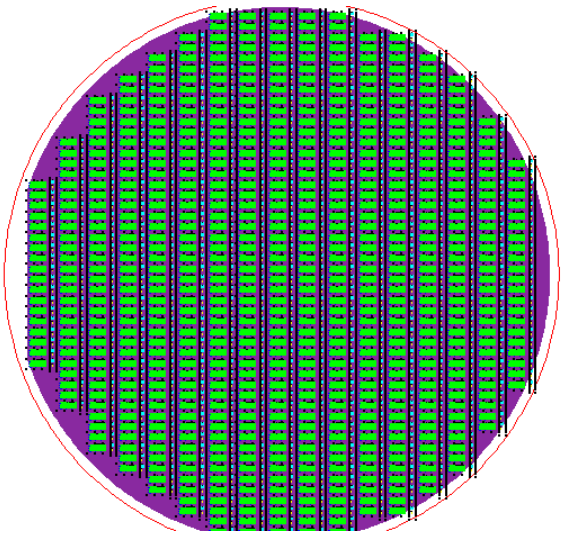

*Figure 100: A 2 inch wafer with repeated design. The flat 110 side of the wafer is on the left side. Blocks which would fit only partially on the wafer have been removed to reduce the exposure time.*

To examine if the growth is direction dependent, a rainbow design has been made as shown in figure 122. Different angles are used. For each angle the width and length of the nanostripes has been varied. Each angle is another crystal direction along the 111 surface of the wafer. The Zinc blende InP and InSb has a special crystal structure with specific crystal directions. This could influence the directions in which the nanowires grow nicely.

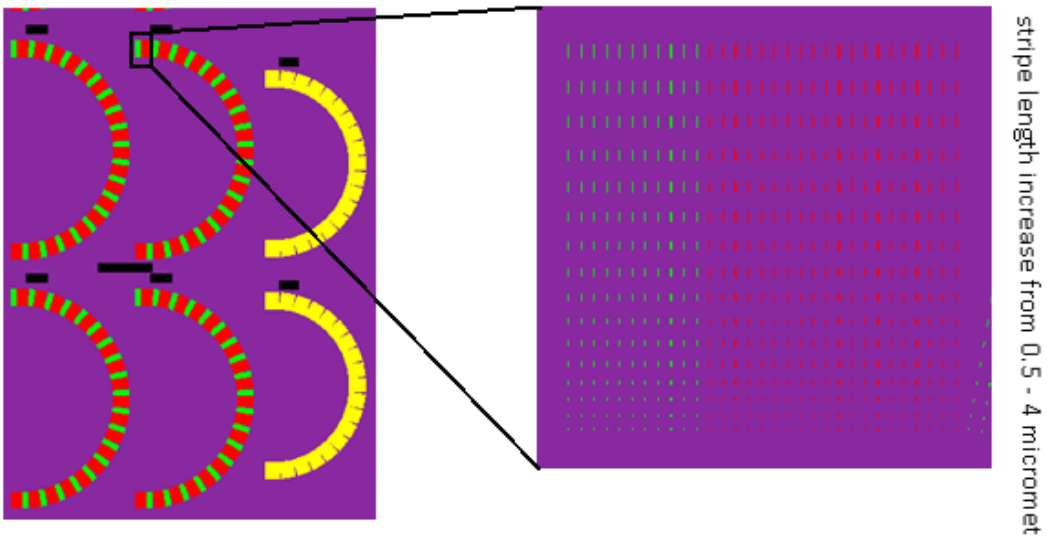


*Figure 101: The rainbow design has been used to investigate if the nanowires grow better along certain directions across the surface. Each angle has a bunch of stripes with varying length and width as shown on the right side.*

### 8.4.5 Development

After Ebeam exposure the scissored pieces of positive resist need to be removed to expose the SiN layer. This procedure is called the 'development'. Each resist has its own developing process, where time plays a key role. The wafer is put in N-amyl-acetate, developer for ZEP-C60, for 60 seconds, followed by 45 seconds of MIBK-IPA (890:110)[54] rinse/developer, and afterwards it gets a 60 seconds IPA bath to clean the surface of chemicals. The IPA acts like a stopper, as the process is time-dependent, a quick stop of development ensures that each wafer gets the same treatment. Longer development can result in larger features while shorter development may result in semi-opened features. The use of N-amyl-acetate as developer and MIBK-IPA as rinse is recommended by the manufacturer and Zeon. [54] Every process in the development has been performed under room temperature conditions.

N-amyl acetate, or pentyl-acetate, has the following chemical structure: $c_7H_{14}O_2$. It is easily detected due to its banana-like odor. This single-solvent compound is recommended by the manufacturer as a ZEP-520A developer. Figure 124 shows the development process. The InP wafer with SiN mask and positive resist is placed in a N-amyl-acetate bath. The light pink area represents the resist exposed during Ebeam. After some time the light pink area disappears while the normal resist stays intact. Over-development may occur when the development is not stopped on time. Widening the structures by damaging the normal resist.

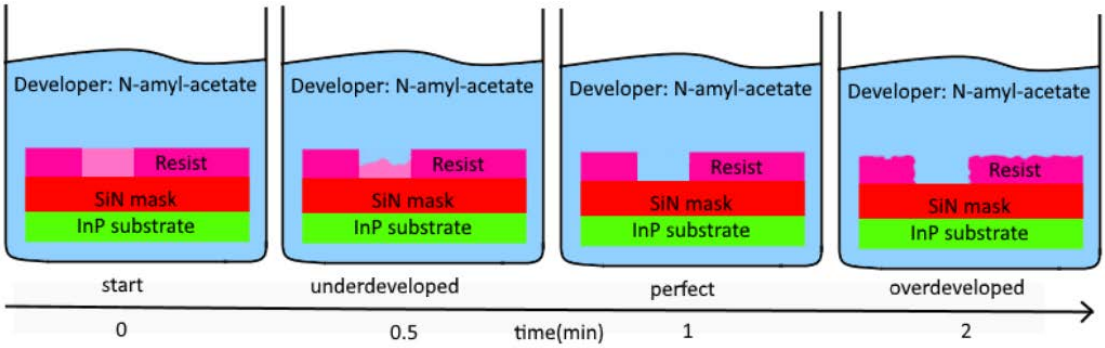


*Figure 103: Develop-procedure of the positive resist after Ebeam exposure. N-amyl-acetate is used as the developer of ZEP520A+C60 resist. The process is time dependent. On the left side the light pink spot is still intact after 0 seconds. Light pink represents the exposed area. After some time the light pink area disappears. If the development is not stopped on the right time overdevelopment may occur, damaging the none exposed resist.*

### 8.4.6 RIE

Reactive-ion etching is used to transfer the design from the positive resist into the SiN layer. Thus exposing the InP wafer underneath, enabling the InSb to grow on the exposed InP. An AC voltage is used to prevent charging of the surface. Where in one half of the cycle the wafer becomes positive due to the ions and in the other half of the cycle the wafer neutralizes due to the electrons. The RF plasma consists of cations, negative anions, radicals and photons. The glow of the plasma is caused by UV photons. A parallel plate reactor generates an artificial plasma using a radiofrequency(RF) power source at 13,56MHz using Ar gas, turning it into $Ar^+$ and electrons. The parallel plates are the top electrode and the bottom electrode. The etching gas ($CHF_3$) flows into the chamber via the gas inlet (see figure 125). The gas will be ionized (stripped from electrons). Electrons follow the RF power source, while ions cannot (too heavy). In the first RF cycles a high electron current manifests and as a result a (-) charged electrode (few 100 Volts) known as DC-Bias or plasma potential is formed. The charged electrode will attract the cloud of ions (ion sheath) and the ions will bombard the surface (sputter). Vertical delivery of reactive species will produce anisotropic etch profiles. [55]

The recipe that was used "Pure $CHF_3$ Etch" operates at 50W, 15mT and 60sccm

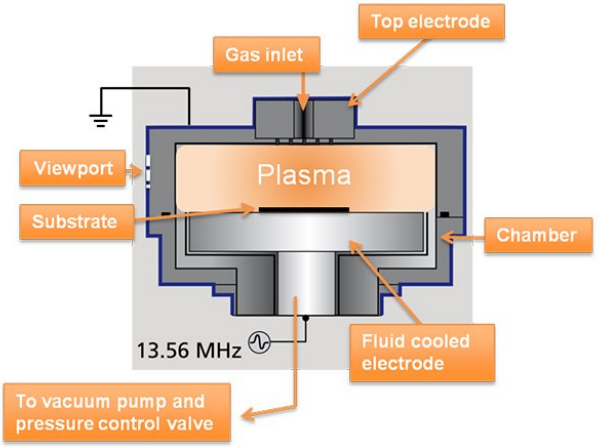


*Figure 104: An illustration of the RIE device. Where the plasma oscillates a t a frequency of 13.56 MHz. The gas inlet is again a showerhead from the top. The ions accelerate vertically and bombard the surface with an impact angle of 90 degrees. This ensures the straight delivery of the design from the resist layer into the SiN layer.*

of $CHF_3$. The etchrate depends on which resist is used, for ZEP520A with buckyballs it has an etchrate between 16 to 26 nm/min. The etchrate can be influenced by adding $H_2$ or $O_2$. $H_2$ decreases the etchrate which results in more control over the amount of material etched but enhances polymerization. The following equation 26 shows the reaction that happens in the chamber.

$$e^- + CHF_3 \rightarrow CHF_2 + F + e^- \tag{26}$$

The electrons react with the $CHF_3$ in the room and form $CHF_2, F$ and an electron. This electron can again react with a $CHF_3$ molecule, creating an avalanche. The byproduct, $CHF_2$, has an unwanted effect. Multiple molecules can polymerize and form long polymer chains, shown in equation 27. These polymers are hard to remove and block the patterns of the design.

$$(CHF_2)^n \rightarrow C_nF_{2n+2} \tag{27}$$

### 8.4.7 Lift-off

After RIE is used to expose the InP substrate, the positive resist has done its job and can be removed from the surface. The SiN layer is preferred to be the top layer during growth as this layer increases the diffusion length of the adatoms on the surface and passivates the surface. The InSb doesn't grow on top of SiN. Baker-PRS-3000™ bulk photoresist stripper is used to remove the ZEP-C60 photoresist. Figure 126 shows the effect of the PRS-3000. The wafer is put in a bath of PRS-3000 for at least 10 hours. After which the PRS-3000 with wafer is put in an ultrasound bath for 2 minutes. The vibrations help remove the photoresist from the surface. To clean the wafer of PRS-3000, an ultrasound bath with Acetone follows for 2 more minutes. As the Acetone leaves residues on the surface the wafer is cleaned with IPA. To clean the surface of organic material the wafer is put in an $O_2$ plasma for 10 minutes at 300 Watt. Finally to deoxidize the surface a 3 minute phosphoric acid dip is used as the last step before the growth.

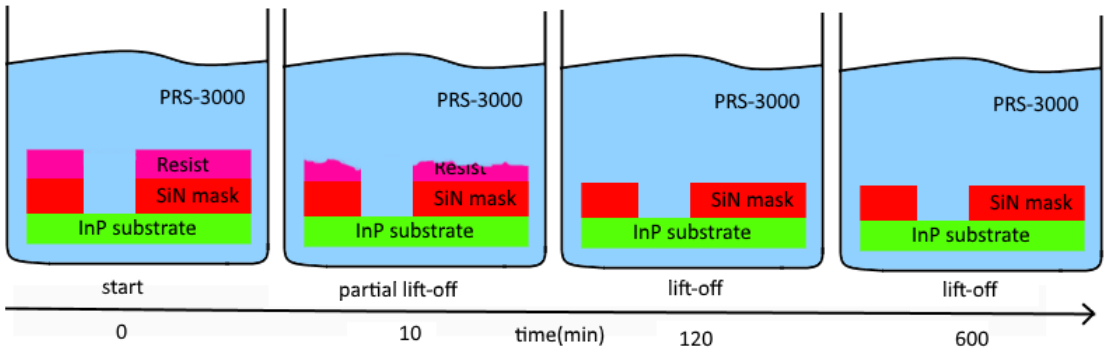


*Figure 105: Illustration of the lift-off process. After RIE the resist layer is no longer needed and is removed using PRS-3000. The PRS-3000 only dissolves the resist layer, keeping the InP and SiN intact. Even after several hours the mask and substrate are still not damaged.*

Baker's PRS-3000 is perfect for lift-off but highly dangerous for humans. Keeping track of the chemicals is important. Table 3 shows the compounds of Baker-PRS3000.[56]

*Table 3: The three main ingredients of Baker's PRS-3000. With corresponding CAS numbers and percentage. All three components are hazardous.*

| Compound | CAS No. | Percent | Hazardous |
|---|---|---|---|
| 1-Methyl-2-pyrrolidinone | 872-50-4 | 40-60% | Yes |
| Thiophene, Tetrahydro-,1,1-dioxide | 126-33-0 | 30-50% | Yes |
| 2-Propanol, 1-amino- | 78-96-6 | 5-15% | Yes |

### 8.4.8 Sample preparation for TEM

The ultrathin filament is prepared with a focused ion beam (FIB). The FIB cuts out a part of the wire by digging holes on three sides. It works basically the same as the SEM but instead of electrons, ions are used. The focused beam of ions with a high energy are used for site specific sputtering and milling. Gallium ions are used in our FIB. Image 127[57] shows the Gallium ions ($Ga^+$) hitting the sample. The atoms from the surface are removed and fly off as secondary ions ($i^+$) or neutral atoms ($n^0$). Secondary electrons can also be formed.

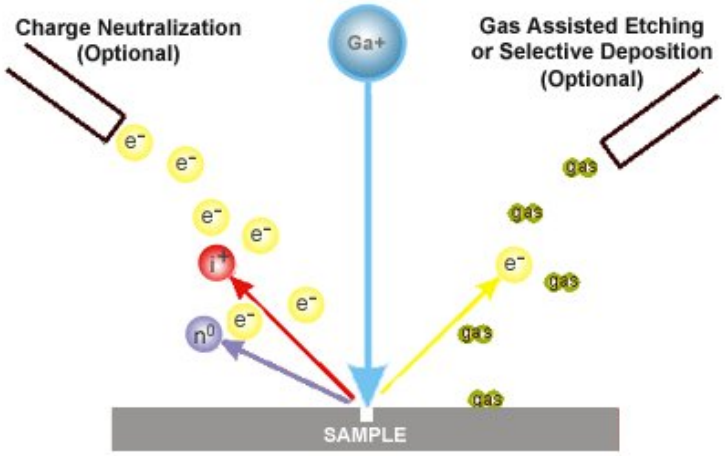


*Figure 127: Illustration showing a Gallium ion beam etching away part of the sample. This is a necessary procedure for in-plane networks to get the grown network without surroundings.*

These high energy Gallium ions damage the surface easily, therefore a few protective layers are first deposited on top of the in-plane nanowire, namely a $SiO_2$ layer and a layer of platinum (Pt). Image 128 shows a nanowire covered for protection. The result of the FIB is clearly visible.

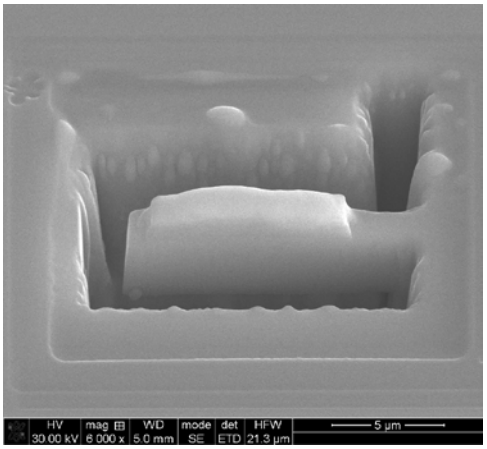


*Figure 128: Image of the in-plane network after the FIB procedure. On three sides trenches are made to be able to move the InSb network to another work station.*

The nanowire is then moved to a different stage. Where a beam of Gallium ions is again used, but now to make the sample as thin as possible, usually around 65-75 nanometre. This helps increasing the resolution of the images the TEM produces.

## 8.5 E: High resolution SEM images

A few high resolution SEM images have been made with a 30° angle view. The results are shown below.

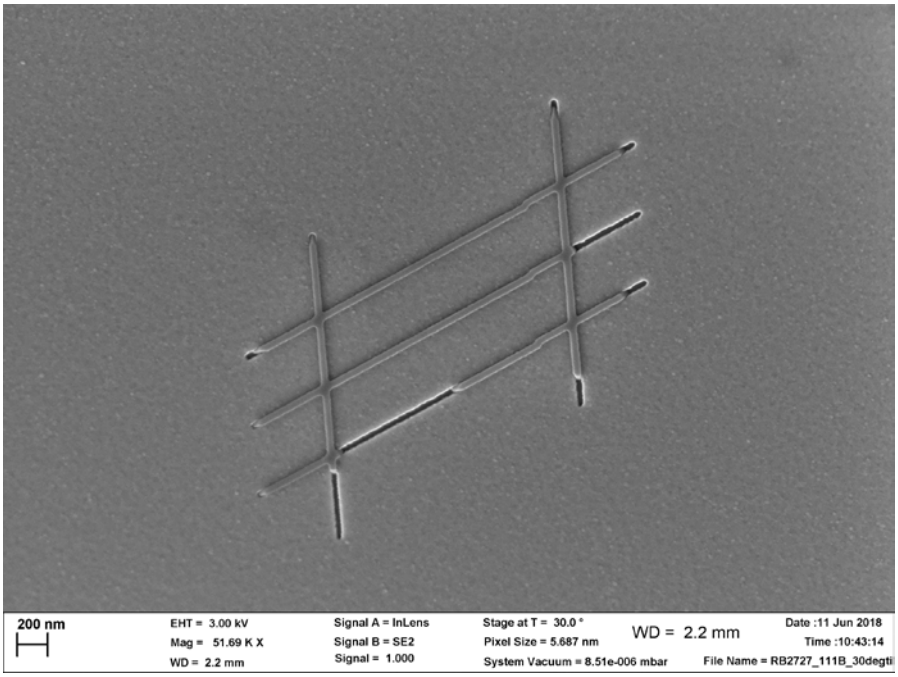


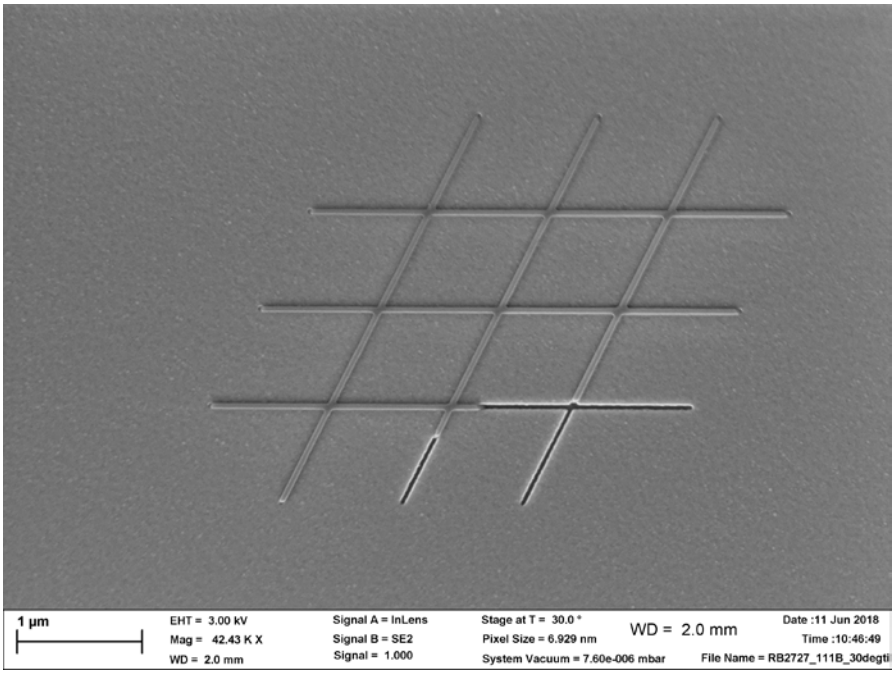

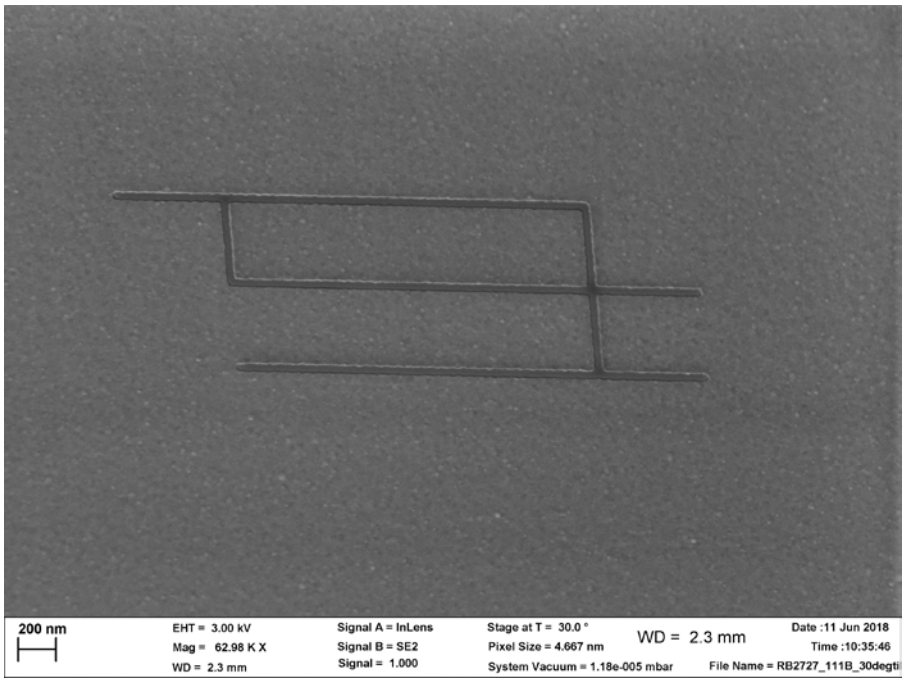
200 nm
EHT = 3.00 kV
Mag = 62.98 K X
WD = 2.3 mm
Signal A = InLens
Signal B = SE2
Signal = 1.000
Stage at T = 30.0 °
Pixel Size = 4.667 nm
System Vacuum = 1.18e-005 mbar
WD = 2.3 mm
Date :11 Jun 2018
Time :10:35:46
File Name = RB2727_111B_30degti

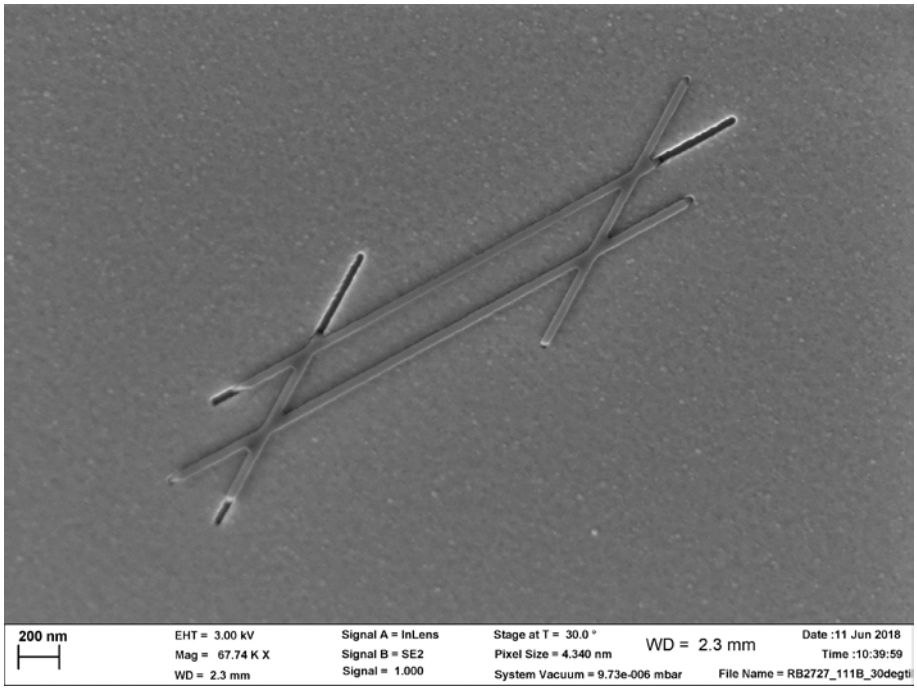
200 nm
EHT = 3.00 kV
Mag = 67.74 K X
WD = 2.3 mm
Signal A = InLens
Signal B = SE2
Signal = 1.000
Stage at T = 30.0 °
Pixel Size = 4.340 nm
System Vacuum = 9.73e-006 mbar
WD = 2.3 mm
Date :11 Jun 2018
Time :10:39:59
File Name = RB2727_111B_30degti

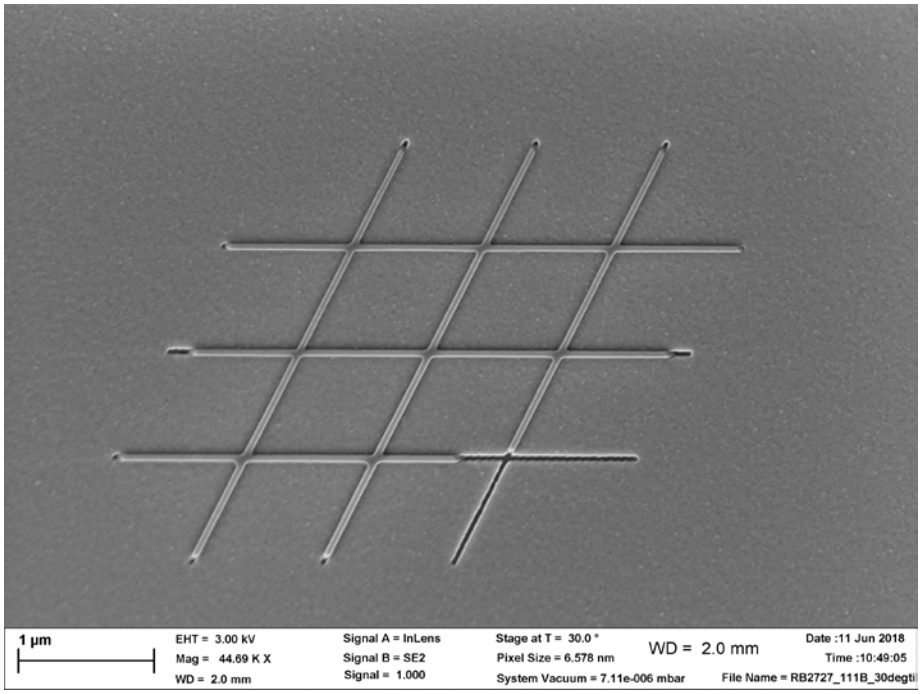
1 µm
EHT = 3.00 kV
Mag = 44.69 K X
WD = 2.0 mm
Signal A = InLens
Signal B = SE2
Signal = 1.000
Stage at T = 30.0 °
Pixel Size = 6.578 nm
System Vacuum = 7.11e-006 mbar
WD = 2.0 mm
Date :11 Jun 2018
Time :10:49:05
File Name = RB2727_111B_30degti

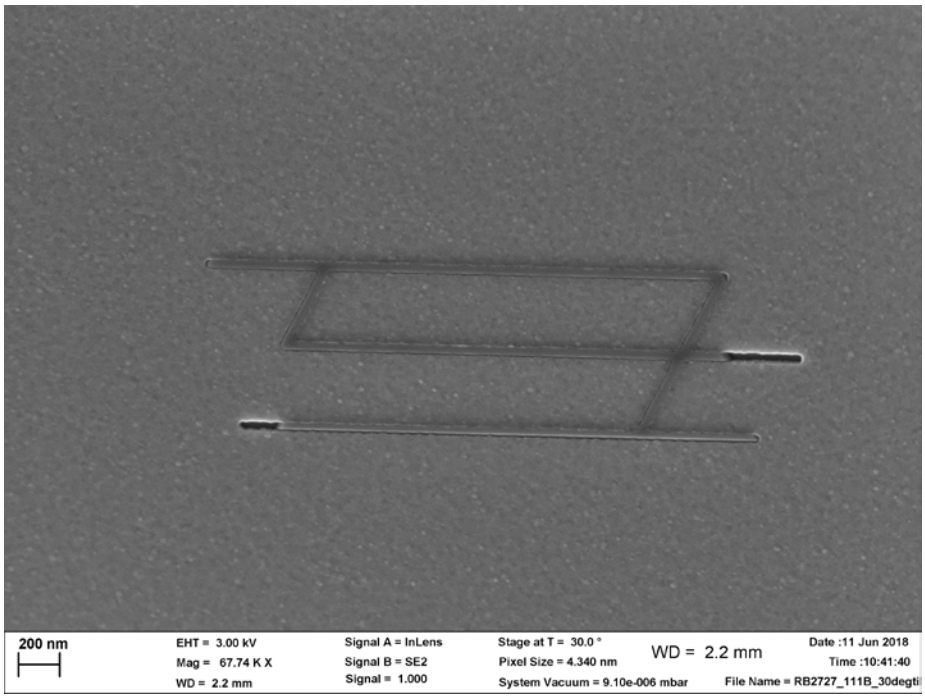
200 nm
EHT = 3.00 kV
Mag = 67.74 K X
WD = 2.2 mm
Signal A = InLens
Signal B = SE2
Signal = 1.000
Stage at T = 30.0 °
Pixel Size = 4.340 nm
System Vacuum = 9.10e-006 mbar
WD = 2.2 mm
Date :11 Jun 2018
Time :10:41:40
File Name = RB2727_111B_30degti

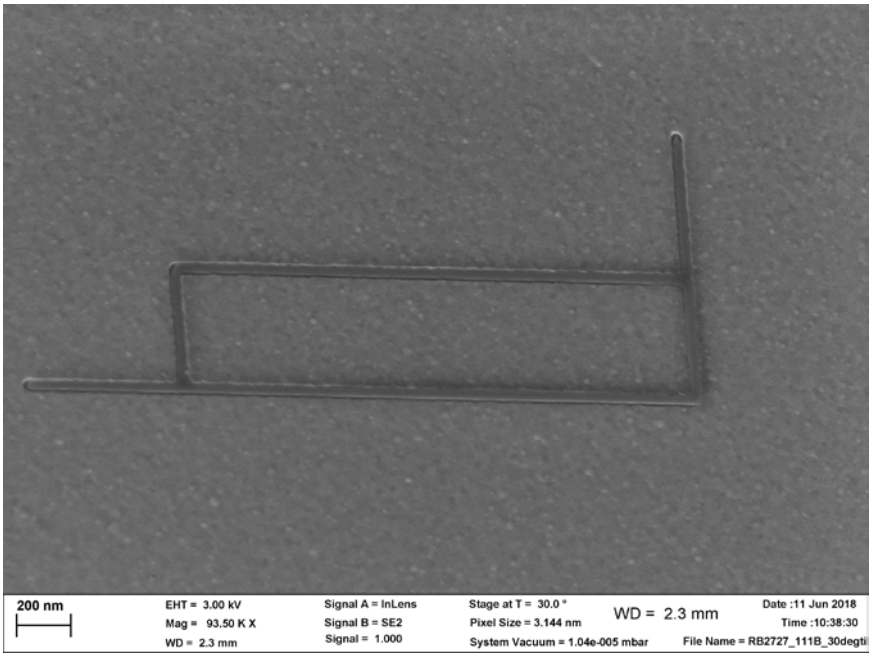
200 nm
EHT = 3.00 kV
Mag = 93.50 K X
WD = 2.3 mm
Signal A = InLens
Signal B = SE2
Signal = 1.000
Stage at T = 30.0 °
Pixel Size = 3.144 nm
System Vacuum = 1.04e-005 mbar
WD = 2.3 mm
Date :11 Jun 2018
Time :10:38:30
File Name = RB2727_111B_30degti

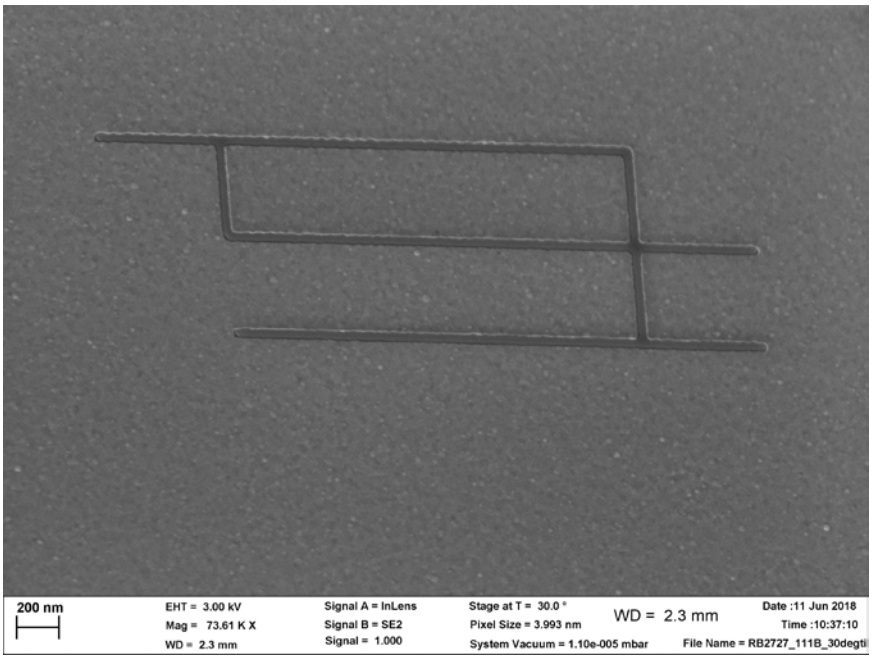
200 nm
EHT = 3.00 kV
Mag = 73.61 K X
WD = 2.3 mm
Signal A = InLens
Signal B = SE2
Signal = 1.000
Stage at T = 30.0 °
Pixel Size = 3.993 nm
System Vacuum = 1.10e-005 mbar
WD = 2.3 mm
Date :11 Jun 2018
Time :10:37:10
File Name = RB2727_111B_30degti